1.0

1.1

1.25   1.4   1.6

2.8   2.5
3.2   2.2
3.6
4.0   2.0

1.8

MICROCOPY RESOLUTION TEST CHART
NATIONAL BUREAU OF STANDARDS 1963 A

FOR FURTHER TRAN
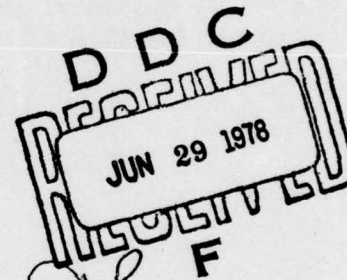
USARTL-TR-78-1A

A055767

ROTOR WAKE EFFECTS ON HUB/PYLON FLOW
Volume I, Theoretical Formulation

Paul Soohoo
Richard B. Noll
Luigi Morino
Norman D. Hamm

Aerospace Systems, Inc.
Burlington, Mass. 01803

May 1978

Final Report for Period June 1975 - September 1977

DDC
JUN 29 1978
F

78 06 27 063

APPLIED TECHNOLOGY LABORATORY POSITION STATEMENT

This report presents a method for determining aerodynamic character-
istics of helicopter shapes under the influence of the main rotor wake.
The method is considered to be worthy of publication for dissemination
of information and the stimulation of further related research. The
reader is cautioned that this method does not predict flow separation
as the title would imply, nor does the rotor wake fully impinge upon
the body of the helicopter. The method is useful, however, as a design
tool in determining rotor-fuselage aerodynamic interference.

Mr. F. A. Raitch of the Aeromechanics Technical Area served as project
engineer for this effort.

REPORT DOCUMENTATION PAGE	READ INSTRUCTIONS BEFORE COMPLETING FORM

1. REPORT NUMBER	2. GOVT ACCESSION NO.	3. RECIPIENT'S CATALOG NUMBER
USARTL-TR-78-1A		

4. TITLE (and Subtitle)	5. TYPE OF REPORT & PERIOD COVERED
ROTOR WAKE EFFECTS ON HUB/PYLON FLOW Volume I. Theoretical Formulation	Final Report - June 1975 - September 1977
	6. PERFORMING ORG. REPORT NUMBER
	ASI-TR-76-38 VOL-1

7. AUTHOR(s)	8. CONTRACT OR GRANT NUMBER(s)
Paul Soohoo Luigi Morino Richard B. Noll Norman D. Ham	DAAJ02-75-C-0041

9. PERFORMING ORGANIZATION NAME AND ADDRESS	10. PROGRAM ELEMENT, PROJECT, TASK AREA & WORK UNIT NUMBERS
Aerospace Systems, Inc. Burlington, Massachusetts 01803	62209A 1F262209AH76 00 087 EK

11. CONTROLLING OFFICE NAME AND ADDRESS	12. REPORT DATE
Applied Technology Laboratory U.S. Army Research & Technology Labs (AVRADCOM) Fort Eustis, Virginia 23604	May 1978
	13. NUMBER OF PAGES
	119

14. MONITORING AGENCY NAME & ADDRESS(if different from Controlling Office)	15. SECURITY CLASS. (of this report)
IF62209AH76	Unclassified
00	15a. DECLASSIFICATION/DOWNGRADING SCHEDULE

16. DISTRIBUTION STATEMENT (of this Report)

Approved for public release; distribution unlimited.

DDC JUN 29 1978 RECEIVED F

17. DISTRIBUTION STATEMENT (of the abstract entered in Block 20, if different from Report)

18. SUPPLEMENTARY NOTES

Volume I of a two-volume report.

19. KEY WORDS (Continue on reverse side if necessary and identify by block number)

Helicopter	Rotors
Hub/Pylon Flow	Separation
Induced Drag	Finite Element Aerodynamics
Potential Aerodynamics	Aerodynamic Computer Program
Rotor Wake	

20. ABSTRACT (Continue on reverse side if necessary and identify by block number)

An investigation has been conducted to demonstrate the use of the Green's function method to study rotor wake effects on helicopter hub/pylon flow. This report consists of two volumes which document the theoretical formulation and the use of the digital computer program SHAPES (Subsonic Helicopter Aerodynamics Program with Effects of Separation).

Volume I presents the theoretical formulation and corresponding numerical procedure for the study of incompressible potential aerodynamics with separated flow. While the

DD FORM 1 JAN 73 1473	EDITION OF 1 NOV 65 IS OBSOLETE	

389 704

20. Abstract (Continued)

formulation is valid for fully unsteady aerodynamics, this report is mainly concerned with rotor aerodynamics. A potential flow aerodynamic program, SHAPES, with suitable rotor wake representation was developed to predict the separation characteristics of arbitrary three-dimensional helicopter configurations. In particular, the effect of the rotor blade wake, blade shank wake, and hub wake in the separation of the flow over a lifting helicopter in forward flight is analyzed.

The present method has potential application in the design of helicopters because it provides an analytical capability which can be used to develop low-drag profile as well as to explore problem areas. Extensive numerical results obtained from Program SHAPES demonstrated the flexibility and accuracy of the method. These results are in excellent agreement with existing data.

PREFACE

This report, prepared by Aerospace Systems, Inc. (ASI), Burlington, Massachusetts, for the U.S. Army under Contract DAAJ02-75-C-0041, documents the results of research performed during the period June 1975 to September 1977. The study was sponsored by the Eustis Directorate, U.S. Army Air Mobility Research and Development Laboratory,* Fort Eustis, Virginia, with Mr. Frederick A. Raitch serving as Technical Monitor.

The effort was directed by Mr. John Zvara, President and Technical Director of ASI. Mr. Paul Soohoo served as Principal Technical Staff Member under the supervision of Mr. Richard B. Noll, Vice President of ASI. Dr. Luigi Morino, Director of Computational Continuum-Mechanics Program at Boston University, and Dr. Norman D. Ham, Director of the V/STOL Technology Laboratory at MIT, contributed to the study as Principal Consultants.

---

*Redesignated Applied Technology Laboratory, U.S. Army Research and Technology Laboratories (AVRADCOM), effective September 1, 1977.

TABLE OF CONTENTS

TABLE OF CONTENTS (Concluded)

LIST OF ILLUSTRATIONS

LIST OF ILLUSTRATIONS (Concluded)

SECTION 1
INTRODUCTION

Early in the design phase, helicopter studies require a great deal of aerodynamic information, such as surface air loads and flow directions, and various component interference velocities. This information is most advantageous before any one configuration is identified as a baseline model for wind tunnel testing. In addition, aerodynamic data required for the most efficient design, such as various rotor/fuselage-induced interference velocities, are often costly and extremely difficult to obtain in a wind tunnel test. Theoretical and experimental works in helicopter aerodynamics are presented in References 1 to 10.

The induced interference effects are of particular importance since the separated flow in areas of high interference velocities is the major source of aerodynamic drag. The interference velocities result in steep adverse pressure gradients that may lead to further separation. Furthermore, the separated wake from rotor/fuselage components creates additional interference due to wake blockage. These effects are seen in Figure 1. The interacting flow fields of the pylon ramp, pylon, shaft, hub, and blade shanks produce a strong diffuser effect that leads to gross separation. To minimize the separation and, therefore, the induced drag, it is necessary to eliminate the peak interference velocities by gross redistribution of cross-sectional area and to contour the localized interference regions around the pylon to avoid the sudden deceleration of flow in the boundary layer.

In the design phase, it is desired to be able to investigate analytically the local interference regions and the effects of geometry variations on the separation characteristics of the design. The advent of high-speed computers has allowed the application of finite element aerodynamic methods to complex aerodynamic configura-

PRESSURE DISTRIBUTION

C_p

POSSIBLE SEPARATION REGIONS

QUASI—ONE DIMENSIONAL FLOW "DIFFUSOR EFFECT"

HIGH LOCAL STREAMLINE ACCELERATION

SEPARATION CREATES
ADDITIONAL INTERFERENCE
DUE TO WAKE BLOCKAGE

HUB

PYLON

FUSELAGE

(From Reference 8.)
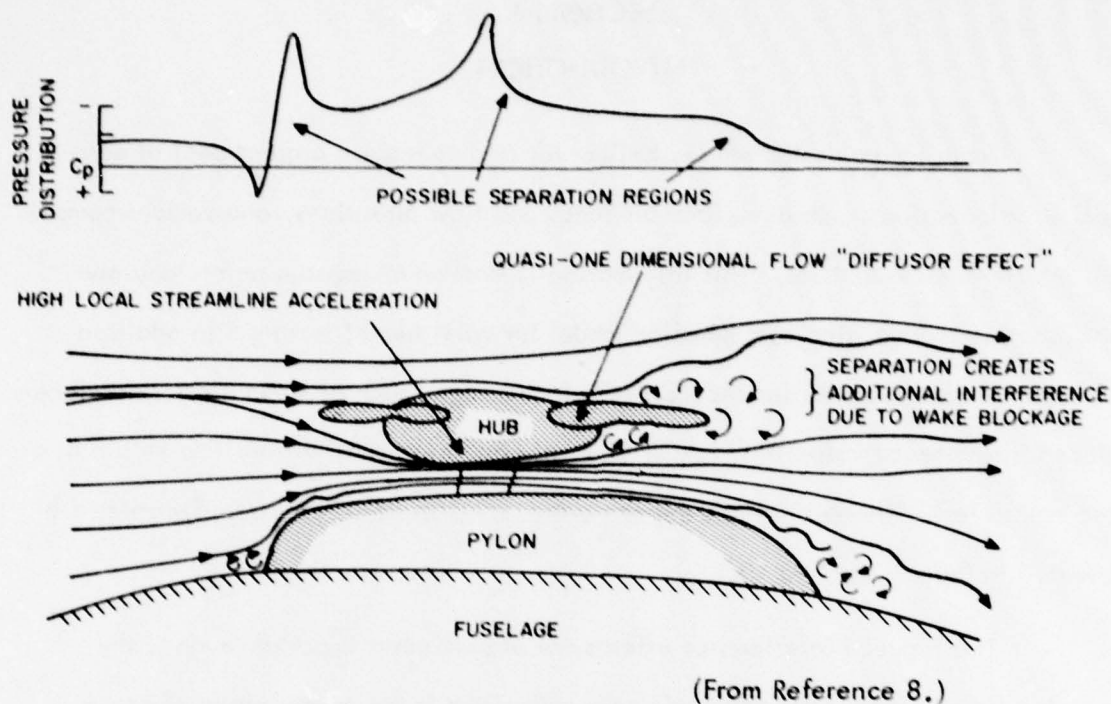
Figure 1. The Hub-Pylon Interference Problem.

tions. As a result, surface airloads may be obtained quickly and efficiently. Flow direction and magnitude can be obtained, aiding in the identification of potential separated flow regions to minimize the effect on aircraft drag.

This report presents the results of a study to examine the total effect of the presence of the rotor in its various operating conditions on the pressure distribution and drag (induced) of the helicopter components beneath the rotor. A potential flow aerodynamic program with suitable rotor wake representation is developed to predict the separation characteristics of arbitrary three-dimensional bodies with lifting surfaces in yawed flow. In particular, the effect of the main rotor blade wake, blade shank wake, and hub wake on the separation of the flow over the hub, shaft, pylon, and fuselage of a lifting helicopter in forward flight is analyzed.

10

The report is presented in two volumes. This volume, Volume I, Theoretical Formulation, gives the theoretical background for the computer program. Volume II, Program SHAPES User's Manual, presents a detailed description of the computer program.

This volume begins with the background description of the helicopter rotor-fuselage aerodynamic interference. The analytical approach to the problem for separated flow and the helicopter rotor wake representation are also discussed. A theoretical formulation for incompressible aerodynamics with separation is given in Section 3. Fundamental aspects of wake dynamics are discussed in Section 4. The numerical formulation of the aerodynamic method for use in the computer program is given in Section 5. Section 6 presents the computed results. Concluding remarks on the present study and recommendations for future research are also provided. A list of references supporting the various discussions is also included.

SECTION 2

HELICOPTER AERODYNAMICS

The helicopter configuration with its numerous rotating parts is a complex aerodynamic shape with intersecting wakes and separated flows. Analysis of these configurations requires the use of computer programs designed for use on high-speed computers. Programs of this type that can be applied to configurations with aerodynamic interference are reviewed in Subsection 2.1. One of these, Program SOUSSA, is discussed in more detail in Subsection 2.2, and its application to helicopter aerodynamics is introduced. The last subsection presents a brief discussion of the representation of the helicopter rotor wake.

2.1   AERODYNAMIC INTERFERENCE

The classical approach for evaluating the aerodynamic pressure on interfering lifting surfaces (wings or rotors) is the lifting surface method (Reference 11). Calculations have been normally limited to wings or other lifting surfaces separately, except for a limited number of cases in which the vehicle could be considered as a slender body. However, interaction of the flow fields of lifting surfaces and the fuselage results in interference effects (Reference 12) that cannot be adequately accounted for when examining the lifting surface and the body separately. The advent of modern high-speed computers has prompted the recent development of a series of new methods, generally called finite element methods. These methods offer both flexibility and efficiency and can be applied to complex configurations. All the methods are based on potential aerodynamics and consider various distributions of sources, doublets, vortices, pressure panels, etc., on and/or inside the surface of the aircraft.

12

An early work on the flow field around three-dimensional bodies by Hess and Smith (Reference 13) uses constant strength source-elements to solve the problem of steady subsonic flow around nonlifting bodies. This method has been extended to lifting bodies (References 14-16) by including doublet and vortex panels. Woodward's method for steady subsonic and supersonic flow (References 17 and 18) is a different approach that uses lifting surface elements for the representation of the body. Little work has been done in unsteady flow. For oscillatory subsonic aerodynamics, extensions of the doublet-lattice method (Reference 19) are obtained by either placing unsteady lifting surface elements on the surface of the body or by using the method of images combined with slender body theory (Reference 20). In the supersonic range, complex configurations are analyzed in References 17, 21, and 22. The program noted in Reference 7 is a modification of the program by Rubbert and Saaris (see Reference 14), which in turn is based on the original program by Hess and Smith (Reference 13).

Of all the methods mentioned above, none is sufficiently general to analyze unsteady rotor-fuselage interference in compressible flow since there exists no frame of reference with respect to which all the surfaces (body and rotor) are fixed. However, a general method for unsteady compressible aerodynamics around complex configurations (where the surface is allowed to move with respect to the frame of reference as necessary for the present analysis) has recently been developed (References 23 and 24). This method provides a unified theory for analyzing steady and unsteady, subsonic and supersonic aerodynamics for complex aircraft configurations and is the only method that allows for the complex unsteady rotor-fuselage interaction in compressible flow. Various developments are given in References 23 to 33.

This method is readily applied to compressible (subsonic and supersonic) flow and is the only known method for analyzing, for instance, unsteady supersonic

13

flow around non-zero-thickness configurations (References 27 and 29). The technique

is implemented in the computer program called SOUSSA (Steady Oscillatory Unsteady

Subsonic and Supersonic Aerodynamics). In this program, the motion of the surface

with respect to the frame of reference is assumed to consist of small oscillations with

arbitrary variation in time. The surface of the aircraft and its wake are divided into

small quadrilateral elements that are approximated by a hyperboloidal surface defined

by four corner points. In this process, the continuity of the surface is maintained,

although discontinuities in the slopes are introduced. The unknown is assumed to be

constant within each element and, therefore, the integral equation reduces to a system

of linear algebraic equations. It should be noted that the general formulation includes

fully unsteady flow. Therefore, the problem of interference of the fuselage with the

rotor is a particular case of the general theory of Reference 23.

2.2   PROGRAM SOUSSA

Program SOUSSA is based on radically new integral equations proposed first

by Dr. Luigi Morino (Reference 23) for lifting non-rigid bodies having arbitrary shapes

and motions (including, for instance, the combined motion of blades-fuselage for a

helicopter in forward flight or maneuvering, with elastic deformation included). The

method is based upon the classical Green's theorem approach, which was never before

used in computational aerodynamics. While the representation of the velocity poten-

tial is still in terms of source and doublets distribution, the specific nature of the

representation (which is not assumed, but obtained from the Green's function theory*)

has many advantages that make the method superior to any other existing one. Only

the subsonic case is described here. First, the integral equation does not imply the

---

*For example, for steady incompressible flows, one obtains a distribution of source with
known intensity equal to the downwash (prescribed from the boundary conditions) and a
distribution of doublets equal to the unknown potential itself. This is obtained by
solving the integral equation (see Section 3).

14

normal derivative of the integral representation (as the others do) and, therefore, there are no singularities in the integral equation (see, for example, Reference 23). This yields programming simplicity with the scheme-convergence being very fast. Therefore, fewer elements are required and thus the computer times are very low. Second, the vorticity distributions over the boundary layer and the wakes are included (as equivalent doublet distributions) in the limit as the viscosity goes to zero (zero-thickness boundary layer and wakes). Third, Program SOUSSA is very simple to use since the type of distribution (source doublet, or vortex elements) is prescribed by the formulation itself and not left to the experience of the engineer using the program. Finally, the methodology is applicable to the general compressible unsteady flow. In particular, the effect of the compressibility and unsteadiness for the rotor-blade motion can be included in an exact way. No other existing theory can accomplish this.

The classical approach is weak in the modeling of separated flows since, in the separated wake (i.e., the region between the dividing line and the body), the flow field is not potential. The presence of vorticity is apparent for the point Q_v (Figure 2). Therefore, formulations of potential flow with boundary layer (where the vorticity is limited to a thin layer near the body) are not adequate to describe the complete flow field since vorticity is not included in the neighborhood of the point Q_v.

The correct formulation for the description of flow fields in the presence of vorticity (rotational, i.e., nonpotential flows) is given in Reference 30. A simplified version of this general, exact formulation is used. This consists in assuming that the vorticity distributed in the separated wake can be replaced with the vorticity of a zero-thickness separation wake* with the addition of a single isolated vortex located

---

*The separation wake is defined here as a zero-thickness vortex sheet (i.e., doublet layer, Reference 23) emanating from the separation line and composed of the dividing streamlines.

FLUID ORIGINATING
FROM FREESTREAM

DIVIDING
STREAMLINE

Qs

SEPARATION LINE

Qv

SEPARATED WAKE
WITH VORTICITY
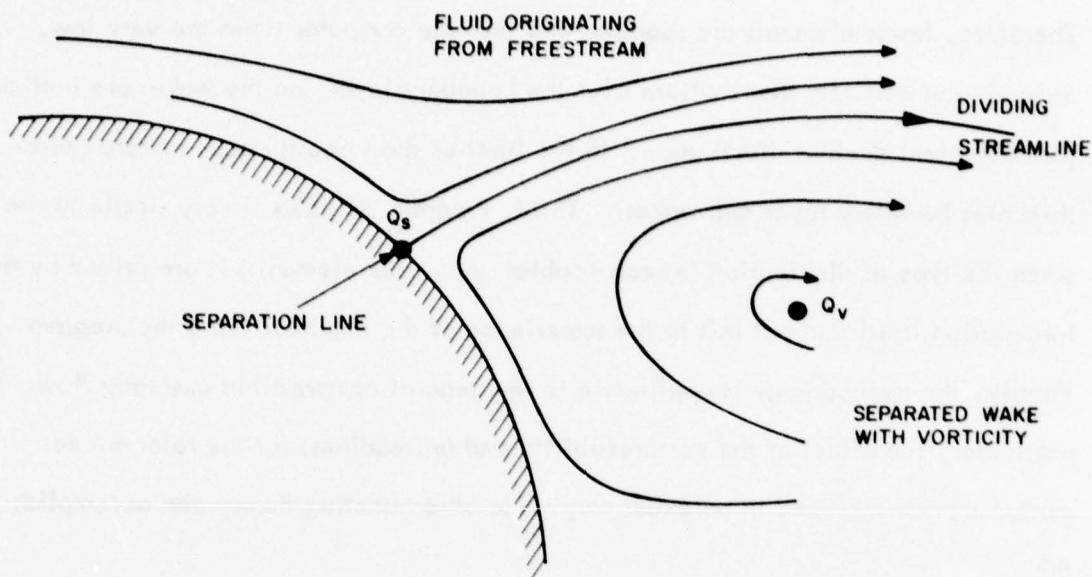
Figure 2. Separated Flow.

at Q_v. The location of the separation line and the geometry of the zero-thickness wake along with the geometry of the vortex line is assumed, based upon experimental results, physical intuition and engineering experience.

Program SOUSSA can be used to solve the problem If the value of the strength of the vortex is known. This value may be obtained by iteration by imposing, at a prescribed point, that the separation line is a stagnation line. In addition, various geometries for the wake and various locations for the separation line will be analyzed by iteration and imposing the condition that the flow field is tangent to the wake surface and that the separation line corresponds to a stagnation line. The agreement with experimental results will be used as final criterion for assessing the improvement and/or correctness in the solution.

16

2.3   ROTOR WAKE GEOMETRY

The complex wake geometry of a helicopter during cruising flight is shown in Figure 3.   The most important parameters are the distribution and time history of blade loading*, which determine the internal structure of the wake as well as the varying size, shape, and deflection angle of the wake, which in turn determine the position of the wake elements with respect to components of the aircraft such as the fuselage.
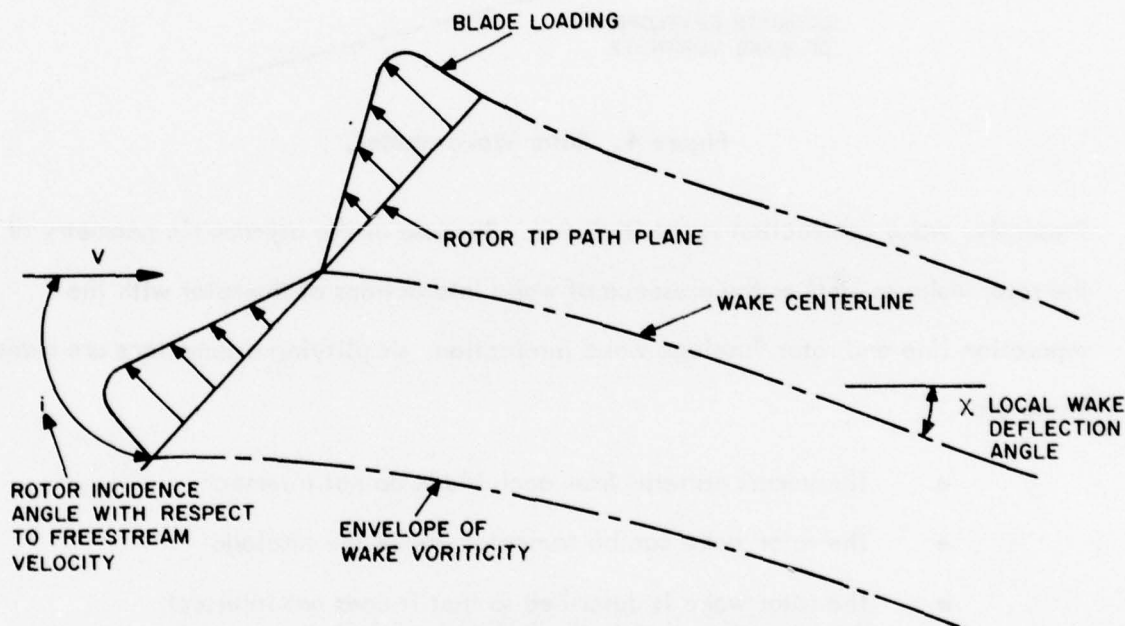
Figure 3. Helicopter Rotor Wake Geometry.

An approximation to the blade loading and vortex wake of the helicopter is made as follows. The wake for each blade is assumed to be a helicoidal surface of vorticity whose axis is at a wake deflection angle X to the free stream velocity, contained within a circular cylinder of fixed radius whose axis is at an angle $(i + X)$ with respect to the rotor tip-path plane. This rotor wake model is shown in Figure 4.

*It should be noted that the blade loading is automatically obtained in Program SOUSSA if the geometry of the wake is assumed.

17
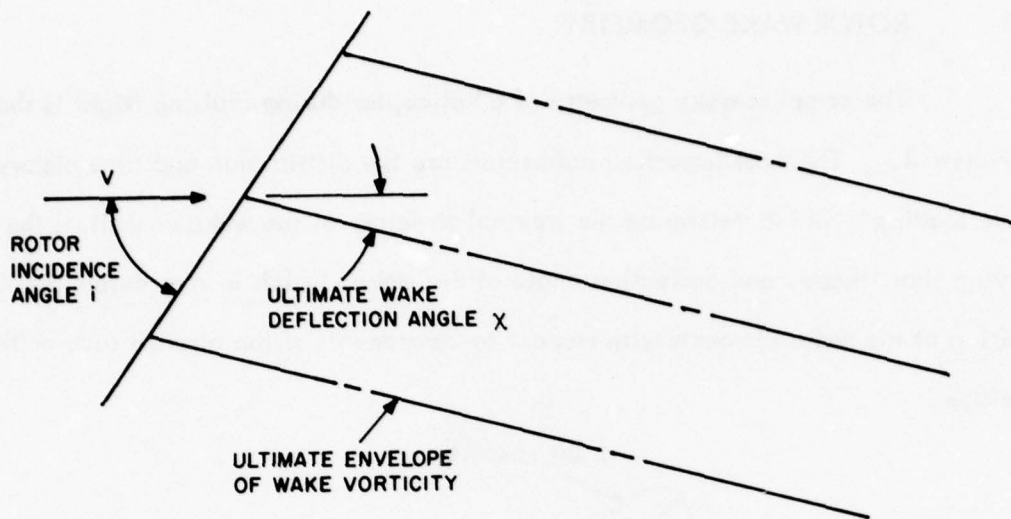
Figure 4. Rotor Wake Model.

Presently, wake contraction is not included. Because of the asymmetric geometry of

the rotor wake as well as the presence of wake interactions of the rotor with the

separation line and rotor/fuselage wake interaction, simplifying assumptions are made.

These are:

- The vortex patterns from each blade do not intersect

- The rotor wake can be truncated above the fuselage

- The rotor wake is described so that it does not intersect
  the separation line or the isolated vorticity

- The separation line and the isolated vorticity are not
  coplanar.

It is shown in References 34 and 35 that when the rotor has a small incidence

angle with respect to the freestream (less than 30°), the wake rapidly rolls up into two

concentrated vortices similar to the tip vortices of a monoplane wing. On this basis,

the wake model chosen for the helicopter is equivalent to two vortices trailed from the

ends of the lateral diameter of the rotor disk. The strength of the vortices is obtained

by assuming that the rotor behaves as an elliptical monoplane wing of span 2R (the

18

Glauert hypothesis) whose lift, i.e., thrust, T, is given by

$$T = \rho V \int_{-R}^{R} \Gamma_o \left[1 - \left(\frac{y}{R}\right)^2\right]^{1/2} dy \tag{1}$$

where ρ = air density

V = flight velocity

Γ_o = midspan value of elliptical circulation distribution

y = spanwise coordinate measured from midspan

R = rotor radius

Making the transformation $y = R \cos \theta$, $dy = -R \sin \theta \, d\theta$, the thrust becomes

$$T = \rho V \Gamma_o R \int_{0}^{\pi} \sin^2 \theta \, d\theta$$

$$= \frac{\pi}{2} \rho V \Gamma_o R \tag{2}$$

Then the strength of the trailing vortices is given by the strength of the midspan circulation, i.e.,

$$\Gamma_o = \frac{T}{\frac{\pi}{2} \rho V R} \tag{3}$$

In the far wake the two vortices are assumed to be convected downward at one-half the local downwash velocity, due to vortex sheet rollup effects, as suggested by the results on page 45 of Reference 34. The resultant flow velocity is then given by the vector

$$\overline{V}' = [(V + 2v \cos i), (v \sin i)] \tag{4}$$

19

where from Reference 36, page 185,

$$v = \frac{C_T \Omega R}{2 [\mu^2 + \lambda^2]^{1/2}} \tag{5}$$

and

$$\mu = \frac{V \sin i}{\Omega R} \tag{6}$$

$$\lambda = \frac{V \cos i + v}{\Omega R} \tag{7}$$

$$C_T = \frac{T}{\rho \pi R^2 (\Omega R)^2} \tag{8}$$

Consequently, the wake deflection angle χ to the freestream is

$$\chi = \tan^{-1} \left[\frac{v \sin i}{V + 2v \cos i} \right] \tag{9}$$

20

SECTION 3

INCOMPRESSIBLE POTENTIAL AERODYNAMICS FOR SEPARATED FLOWS

The general formulation for incompressible potential aerodynamics for separated flows is presented in this section. For incompressible fluids, potential flows are obtained if the fluid is inviscid and the velocity flow field is irrotational at time $t = 0$. Accordingly, these hypotheses are invoked here. Since the analysis of separated flows was not included in the preceding descriptions of the formulation for SOUSSA, a new formulation is presented here, starting from basic principles and avoiding the hypothesis that the flow is not separated.

3.1   INCOMPRESSIBLE INVISCID FLOWS

Assuming the fluid to be [1]* inviscid, and [2] incompressible, the motion is governed by the Euler equations

$$\left(\frac{\partial}{\partial t} + \bar{V} \cdot \bar{\nabla} \right) \bar{V} = - \frac{1}{\rho} \bar{\nabla} p \tag{10}$$

and the continuity equation (for incompressible fluid)

$$\bar{\nabla} \cdot \bar{V} = 0 \tag{11}$$

where $\bar{V}$ is the velocity vector with respect to a prescribed frame of reference, p is the pressure, ρ the density (constant for incompressible fluid), t the time, whereas

$$\bar{\nabla} = \bar{i} \frac{\partial}{\partial x} + \bar{i} \frac{\partial}{\partial y} + \bar{k} \frac{\partial}{\partial z} \tag{12}$$

is the del operator. Equations (10) and (11) form a system of four partial differential equations for four unknowns V_x, V_y, V_z, and p.

---

*Numbers in brackets indicate new hypotheses introduced in the formulation.

21

In order to complete the formulation of the problem, the boundary conditions at infinity on the body and on the wake must be obtained. Here it will be assumed that [3] the unperturbed flow consists of uniform translation, e.g., in the x-axis direction. Hence, the boundary condition at infinity may be written as

$$\bar{V} = U_{\infty} \bar{i} \quad \text{(for P at } \infty\text{)} \tag{13}$$

where U_{∞} is the freestream velocity. In particular, $U_{\infty} = 0$ for helicopters in hover.

On the body it is assumed that [4] the surface of the body is impermeable, i.e., the normal components of the velocity $\bar{V}$ of the fluid, and of the velocity $\bar{V}_B$ of the body coincide at point P on the surface Σ_B of the body:

$$(\bar{V} - \bar{V}_B) \cdot \bar{n} = 0 \quad \text{(for P on } \Sigma_B\text{)} \tag{14}$$

where $\bar{n}$ is the normal to Σ_B at P.

Next, the boundary condition on the wake for lifting bodies is considered. It is assumed that [5] the body has certain separation lines (in particular sharp trailing edges) and that the velocity flow field has surfaces of discontinuity (wakes) emanating from these separation lines (or trailing edges). Indicating by subscripts 1 and 2 the two sides of the wake, let $\bar{n}$ be the outward normal on side 1 and let

$$\Delta f = f_1 - f_2 \tag{15}$$

denote the discontinuity of any functions f across the wake surface. (For the classical wing wake, 1 and 2 correspond to upper and lower sides, respectively; $\bar{n}$ is the upper normal and $\Delta f = f_u - f_\ell$.) The boundary condition on the wake surface Σ_W is that there is no pressure discontinuity at point P on the wake

$$\Delta p = 0 \quad \text{(for P on } \Sigma_W\text{)} \tag{16}$$

22

This condition can be expressed more conveniently in terms of the velocity discontinuity. However, this requires the introduction of the concept of Lamb surfaces. These surfaces may be avoided in the case of potential flow and, therefore, the boundary condition is given here for potential flows only.

Equations (10), (11), (13), (14), and (16) completely define the problem in terms of four partial differential equations for four unknowns V_x, V_y, V_z and p, with the corresponding boundary conditions.

3.2 DIFFERENTIAL FORMULATION FOR INCOMPRESSIBLE POTENTIAL FLOWS

In the preceding section, the flow was assumed to be [1] inviscid and [2] incompressible. Next assume [6] the flow to be initially irrotational; then the flow remains irrotational at all times and, therefore, there exists a potential function Φ such that

$$\bar{V} = \bar{\nabla} \Phi \tag{17}$$

In this case, Equation (10) may be integrated to yield Bernoulli's theorem*

$$\frac{\partial \Phi}{\partial t} + \frac{1}{2} |\bar{\nabla} \Phi|^2 + \frac{p}{\rho} = \frac{1}{2} U_\infty^2 + \frac{p_\infty}{\rho} \tag{18}$$

_____

*The x derivative of Equation (18) yields

$$\frac{\partial}{\partial x} \left(\frac{\partial \Phi}{\partial t} + \frac{1}{2} |\bar{\nabla} \Phi|^2 + \frac{p}{\rho} \right) = \frac{\partial}{\partial t} \left(\frac{\partial \Phi}{\partial x} \right) + \frac{\partial \Phi}{\partial x} \frac{\partial^2 \Phi}{\partial x^2} + \frac{\partial \Phi}{\partial y} \frac{\partial^2 \Phi}{\partial x \partial y}$$

$$+ \frac{\partial \Phi}{\partial z} \frac{\partial^2 \Phi}{\partial x \partial z} + \frac{1}{\rho} \frac{\partial p}{\partial x}$$

$$= \left(\frac{\partial}{\partial t} + \bar{V} \cdot \bar{\nabla} \right) V_x + \frac{1}{\rho} \frac{\partial p}{\partial x} = 0$$

in agreement with the first component of Equation (10).

23

The constant on the right-hand side of Equation (18) is obtained from the boundary conditions at infinity.

Furthermore, Equation (11) may be rewritten as

$$\nabla^2 \Phi = 0 \tag{19}$$

where ∇^2 is the Laplacian operator.

Similarly, Equation (13) may be rewritten as

$$\Phi = U_\infty x \quad \text{(for P at } \infty) \tag{20}$$

and Equation (14) becomes

$$\frac{\partial \Phi}{\partial n} = \bar{V}_B \cdot \bar{n} \tag{21}$$

Next consider the boundary condition on the wake given by Equation (16). Combining Equations (16) and (18) yields

$$\frac{\partial}{\partial t} \left(\Phi_1 - \Phi_2 \right) + \frac{1}{2} \left(\overline{\nabla \Phi}_1 \cdot \overline{\nabla \Phi}_1 - \overline{\nabla \Phi}_2 \cdot \overline{\nabla \Phi}_2 \right) = 0 \tag{22}$$

or

$$\left(\frac{\partial}{\partial t} + \bar{V}_A \cdot \bar{\nabla} \right) \Delta \Phi = 0 \tag{23}$$

with

$$\Delta \Phi = \Phi_1 - \Phi_2 \tag{24}$$

and

$$\bar{V}_A = \frac{1}{2} \left(\overline{\nabla \Phi}_1 + \overline{\nabla \Phi}_2 \right) = \frac{1}{2} \left(\bar{V}_1 + \bar{V}_2 \right) \tag{25}$$

is the average value of the velocity. This average value may be attributed to the point P_w on the wake. Equation (23) may thus be interpreted as

24

$$\Delta \Phi (P_w) = \text{constant in time} \tag{26}$$

where P_w is the physical point of the wake being convected with velocity $\overline{V}_A$. Note that Equation (23) implies that the wake is tangent to $\overline{V}_A$. In particular, for the steady state, the wake is composed of the streamlines of points P_w emanating from trailing edges or other separation lines. Equation (19) is a partial differential equation for Φ with boundary conditions given by Equations (20), (21), and (23). Once Φ is known, the velocity is given by Equation (17), while the pressure is obtained from Equation (18). It may be worth noting that the potential aerodynamics formulation considered in this section is considerably simpler than the formulation based upon physical variables ($\overline{V}$ and p) since the former gives one linear partial differential equation instead of four nonlinear ones.

3.3   PERTURBATION POTENTIAL

In order to use the Green's theorem approach, it is convenient to have homogeneous boundary conditions at infinity. This can be accomplished by introducing the perturbation potential φ, related to the potential Φ by

$$\Phi = U_\infty x + \varphi \tag{27}$$

Then, Equation (19) yields

$$\nabla^2 \varphi = 0 \tag{28}$$

while the condition at infinity, Equation (20), becomes homogeneous

$$\varphi = 0 \quad \text{(for P at } \infty \text{)}. \tag{29}$$

On the other hand, combining Equations (21) and (27), the boundary condition on the body is now given by

$$\frac{\partial \varphi}{\partial n} = \left(-U_\infty \, \bar{i} + \bar{V}_B\right) \cdot \bar{n} \tag{30}$$

while on the wake (see Equations (23) and (26))

$$\left(\frac{\partial}{\partial t} + \bar{V}_A \cdot \bar{\nabla}\right) \Delta \varphi = 0 \tag{31}$$

or

$$\Delta \varphi \, (P_w) = \text{constant in time} \tag{32}$$

Furthermore, once φ is known, the perturbation velocity

$$\bar{v} = \bar{\nabla} \varphi \tag{33}$$

may be evaluated and then the velocity is given by

$$\bar{V} = U_\infty \, \bar{i} + \bar{v} \, . \tag{34}$$

Accordingly, the Bernoulli theorem may be rewritten as

$$\frac{\partial \varphi}{\partial t} + U_\infty \frac{\partial \varphi}{\partial x} + \frac{1}{2} \, |\bar{\nabla}\varphi|^2 + \frac{p}{\rho} = \frac{p_\infty}{\rho} \, . \tag{35}$$

The above equations could be obtained in a slightly different way, i.e., by assuming the frame of reference to be connected with the undisturbed air. The velocity of the body in such a frame of reference would be given by $-U_\infty \, \bar{i} + \bar{V}_B$, in agreement with Equation (30).

3.4   GREEN'S FORMULA FOR LAPLACE EQUATION

Consider two arbitrary functions f and g and note that

$$\overline{\nabla} \cdot (f\overline{\nabla}g) = \overline{\nabla}f \cdot \overline{\nabla}g + f\nabla^2 g$$

and

$$\overline{\nabla} \cdot (g\overline{\nabla}f) = \overline{\nabla}g \cdot \overline{\nabla}f + g\nabla^2 f \tag{36}$$

or

$$\overline{\nabla} \cdot (f\overline{\nabla}g - g\overline{\nabla}f) = f\nabla^2 g - g\nabla^2 f. \tag{37}$$

Also, according to the Gauss theorem, for any arbitrary vector $\overline{a}$

$$\iiint_{V'} \overline{\nabla} \cdot \overline{a} \, dV = \oiint_{\Sigma} \overline{a} \cdot \overline{n} \, d\Sigma \tag{38}$$

where Σ surrounds V' and $\overline{n}$ is the inward directed normal. Combining Equations (37) and (38) yields

$$\iiint_{V'} (f\nabla^2 g - g\nabla^2 f) \, dV = \oiint (f\overline{\nabla}g - g\overline{\nabla}f) \cdot \overline{n} \, d\Sigma$$

$$= \oiint \left(f\frac{\partial g}{\partial n} - \frac{\partial f}{\partial n} \right) d\Sigma \tag{39}$$

Next, assume that both f and g satisfy the Laplace equation, that is

$$\nabla^2 f = \nabla^2 g = 0 \quad (\text{in } V). \tag{40}$$

Then Equation (39) yields

$$\oiint \left(f\frac{\partial g}{\partial n} - g\frac{\partial f}{\partial n} \right) d\Sigma = 0 \tag{41}$$

which is the desired Green's formula for the Laplace equation.

Next choose the function g to be the simplest function that satisfies the Laplace equation. If g is a function of the distance r from a specified point P_*, then

27

the function that satisfies the Laplace equation is

$$g = \frac{A}{r} + B \tag{42}$$

where

$$r = |P - P_*| \tag{43}$$

Note that P_* must be outside the volume V; otherwise Equation (40) is not satisfied at P_*. Also note that the value of B does not affect Equation (41) under the condition

$$\oiint \frac{\partial f}{\partial n} \, d\Sigma = 0 \tag{44}$$

which is obtained from Equation (41) with $g = 1$. Therefore, the convenient value $B = 0$ is used here. For this case the function g represents a source. It is convenient to choose A such that g represents <u>a unit source</u>, that is, a source with flux equal to 1. This is obtained with $A = -1/4\pi$, i.e.,*

$$g = -\frac{1}{4\pi r} \tag{45}$$

Combining Equations (41) and (44) yields the desired Green's formula for the Laplace equation

$$\oiint_{\Sigma} \left[f \frac{\partial}{\partial n} \left(\frac{-1}{4\pi r} \right) - \frac{\partial f}{\partial n} \left(\frac{-1}{4\pi r} \right) \right] d\Sigma = 0 \tag{46}$$

---

* For, in this case, the flux through a spherical surface of radius R is given by

$$\iint_{\Sigma} \bar{v} \cdot \bar{n} \, d\Sigma = \iint_{\Sigma} \frac{\partial g}{\partial r} \bigg|_{r=R} d\Sigma = \frac{1}{4\pi R^2} \cdot 4\pi R^2 = 1$$

28

3.5   GREEN'S THEOREM FOR INCOMPRESSIBLE POTENTIAL AERODYNAMICS

In order to obtain the Green's theorem for incompressible aerodynamics (Laplace equation for the exterior problem, i.e., for V' outside the surface Σ_0), it is convenient to consider the surface Σ composed of three branches as indicated in Figure 5. Note that the inward normal for V' is outward to Σ_0. Σ_1 is a spherical surface of radius ϵ and center P_*, while Σ_2 is a spherical surface of radius R and center P_*.

Then Equation (46), for $f = \varphi$, reduces to

$$\oiint_{\Sigma_0 + \Sigma_1 + \Sigma_2} \left[\varphi \frac{\partial}{\partial n} \left(\frac{-1}{4\pi r} \right) - \frac{\partial \varphi}{\partial n} \left(\frac{-1}{4\pi r} \right) \right] d\Sigma = 0 \tag{47}$$

Note that as the radius ϵ of Σ_1 goes to zero

$$\lim_{\epsilon \to 0} \oiint_{\Sigma_1} \left[\varphi \frac{\partial}{\partial n} \left(\frac{-1}{4\pi r} \right) - \frac{\partial \varphi}{\partial n} \left(\frac{-1}{4\pi r} \right) \right] d\Sigma$$

$$= \lim_{\epsilon \to 0} \left[\varphi_* \oiint_{\Sigma_1} \frac{\partial}{\partial r} \left(\frac{-1}{4\pi r} \right) d\Sigma - \left(\frac{\partial \varphi}{\partial n} \right)_* \oiint_{\Sigma_1} \frac{-1}{4\pi r} d\Sigma \right]$$

$$= \lim_{\epsilon \to 0} \left[\varphi_* \frac{1}{4\pi \epsilon^2} \oiint_{\Sigma_1} d\Sigma + \left(\frac{\partial \varphi}{\partial n} \right)_* \frac{1}{4\pi \epsilon} \oiint_{\Sigma_1} d\Sigma \right]$$

$$= \lim_{\epsilon \to 0} \left[\varphi_* + \left(\frac{\partial \varphi}{\partial n} \right)_* \epsilon \right] = \varphi_* \tag{48}$$

whereas, as the radius R_{Σ_2} of Σ_2 goes to infinity

29
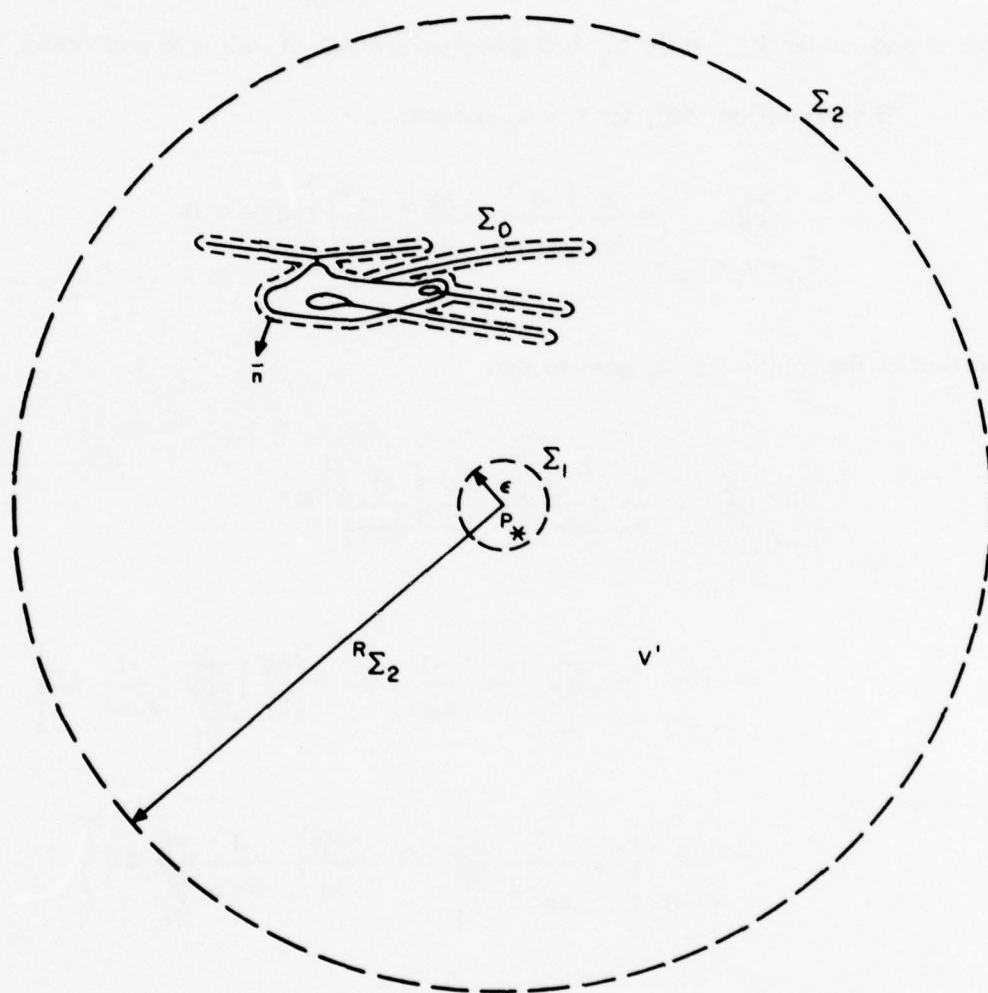
Figure 5. Geometry for Green's Theorem for Potential Aero-
dynamics of Separated Incompressible Flows.

30

$$\lim_{\substack{R \to \infty \\ \Sigma_2}} \oiint_{\Sigma_2} \left[\varphi \frac{\partial}{\partial n} \left(\frac{-1}{4\pi r} \right) - \frac{\partial \varphi}{\partial n} \left(\frac{-1}{4\pi r} \right) \right] d\Sigma$$

$$= \lim_{\substack{R \to \infty \\ \Sigma_2}} \left[\varphi_\infty + \left(\frac{\partial \varphi}{\partial n} \right)_\infty R \right] = 0 \tag{49}$$

under the conditions*

$$\lim_{\substack{R \to \infty \\ \Sigma_2}} \varphi = 0 \tag{50}$$

$$\lim_{\substack{R \to \infty \\ \Sigma_2}} \frac{\partial \varphi}{\partial n} R = 0 \tag{51}$$

Therefore, as ϵ tends to zero and R_{Σ_2} tends to infinity, Equation (37) becomes

$$\varphi_* = \oiint_{\Sigma_0} \left[\frac{\partial \varphi}{\partial n} \left(\frac{-1}{4\pi r} \right) - \varphi \frac{\partial}{\partial n} \left(\frac{-1}{4\pi r} \right) \right] d\Sigma_0 \tag{52}$$

If the point P_* is inside Σ_0, then there is no need for the surface Σ_1. In this case, Equation (47) yields simply

$$0 = \oiint_{\Sigma_0} \left[\frac{\partial \varphi}{\partial n} \left(\frac{-1}{4\pi r} \right) - \varphi \frac{\partial}{\partial n} \left(\frac{-1}{4\pi r} \right) \right] d\Sigma_0 \tag{53}$$

Equations (52) and (53) may be combined by writing

$$E_* \varphi_* = \oiint_{\Sigma_0} \left[\frac{\partial \varphi}{\partial n} \left(\frac{-1}{4\pi r} \right) - \varphi \frac{\partial}{\partial n} \left(\frac{-1}{4\pi r} \right) \right] d\Sigma_0 \tag{54}$$

---

* It is verified a posteriori (Equations (71) and (72)) that these conditions are satisfied.

31

where

$$E_* = E(P_*) = 1 \qquad (P_* \text{ outside } \Sigma_0)$$

$$= 0 \qquad (P_* \text{ inside } \Sigma_0) \tag{55}$$

3.6　ROTOR-FUSELAGE-WAKE INTERACTION WITH FLOW SEPARATION

The model considered here for the analysis of separated flows around rotor-fuselage configurations consists of the actual geometry of the fuselage and the rotor blades. In addition, a vortex-layer wake emanates from the trailing edge of each rotor blade, and a vortex-layer wake emanates from the separation line as shown in Figure 6. Finally, the vorticity in the separated wake is modeled as one single isolated vortex line.

The model described above is relatively crude. In particular, isolated vortices are transported by the flow field whereas the isolated vortex considered here is assumed to remain in a fixed position with respect to the helicopter. This apparent contradiction is explained by the fact that the distributed vorticity in the separated wake (converted downstream by the flow field) is continuously replaced by the vorticity coming from the boundary layer. Therefore, the vortex line should be thought of as an analytical model to represent the vorticity field in a form that is computationally efficient. As a consequence, the location of the vortex line is somewhat arbitrary, while the intensity can be used to obtain the condition that the velocity be equal to zero at Q_s (Figure 6).

The model described above can be analyzed using the potential flow formulation presented in the preceding section. In order to accomplish this, note that the flow field is potential everywhere except on the wakes and the isolated vortex line. Therefore, if one considers the surface Σ_0 depicted in Figure 7 (i.e., a surface surrounding

32
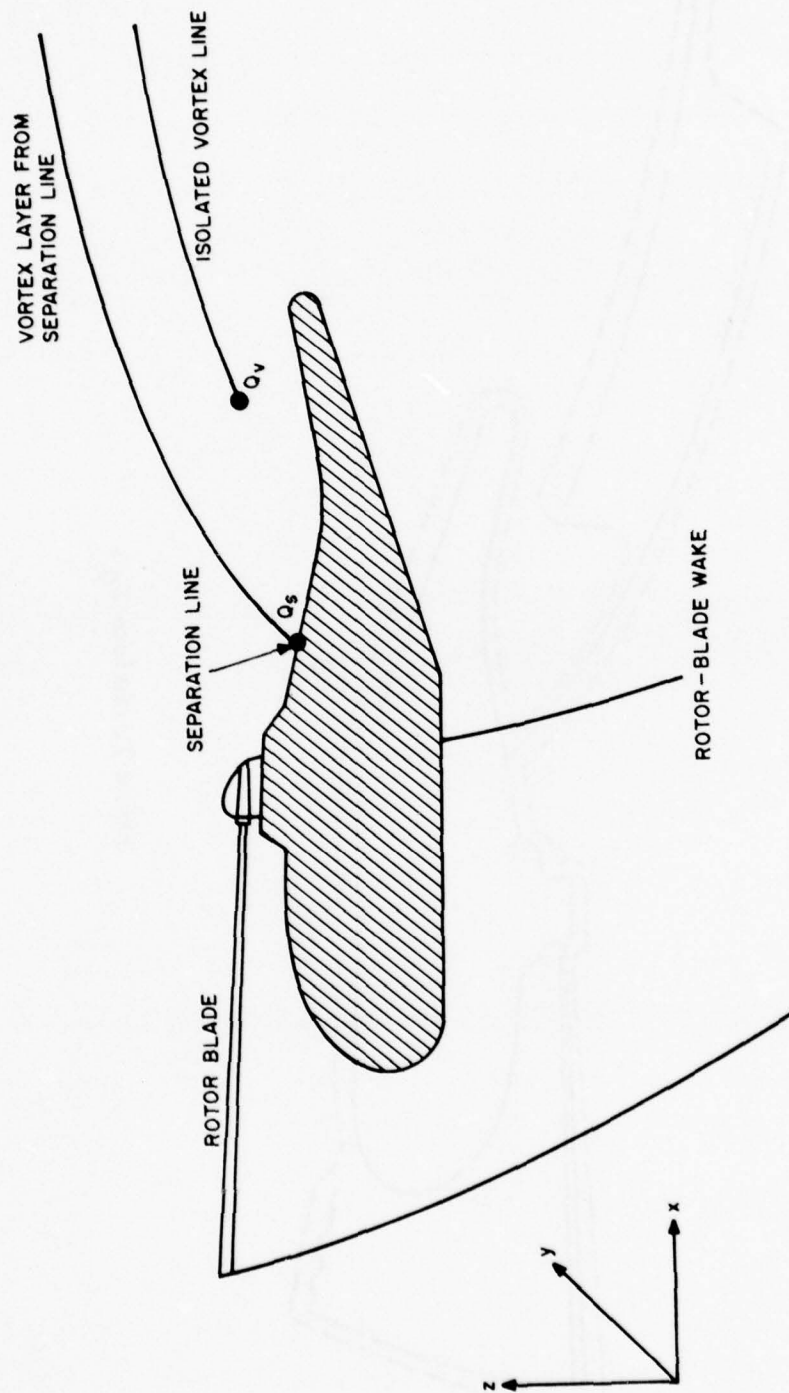
Figure 6. Model for Analysis of Separated Flow Around Rotor-Fuselage Configuration (Only $y > 0$ Half of Configuration is Shown).

Σ_0
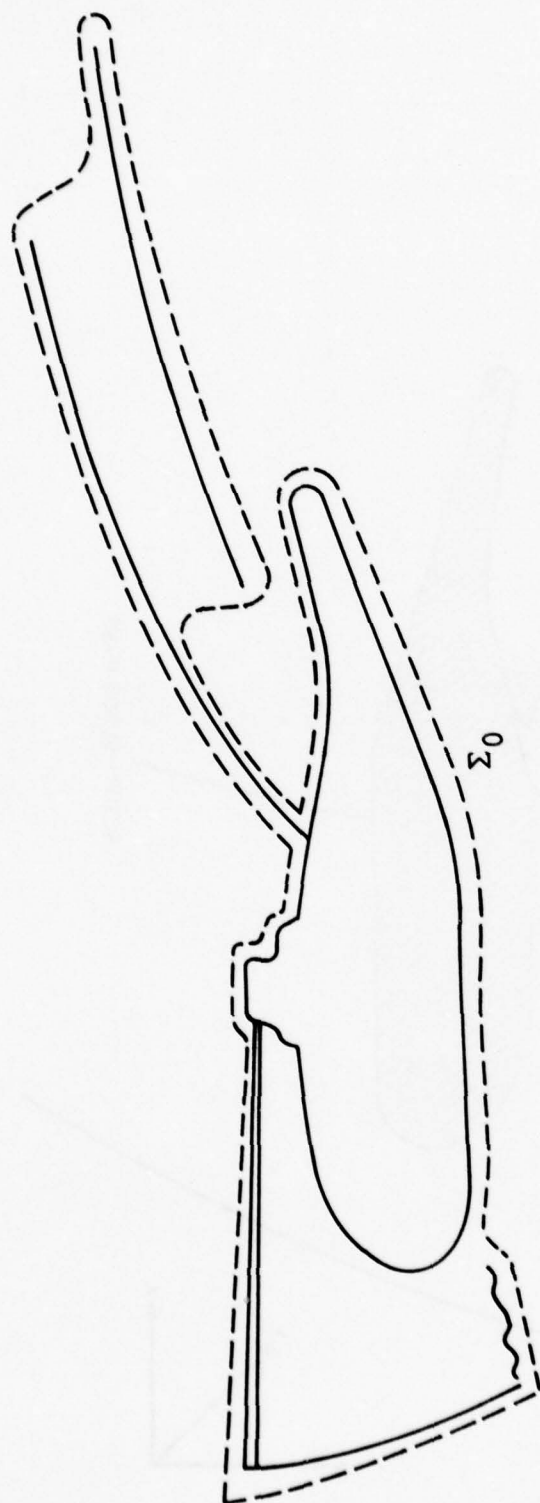
Figure 7. Surface Σ_0.

the rotor, fuselage, wakes, and the isolated vortex) the flow is potential outside Σ_0 and, therefore, Equation (54) is valid.

Next consider an open surface having as its boundary the isolated vortex line. Such a surface does not intersect any of the other surfaces (i.e., the fuselage, rotor, rotor wake, and separation wake) and has otherwise arbitrary shape. The function of this surface is similar to the one of the branch lines in the theory of complex variables and, therefore, it will be indicated as a <u>branch surface</u>, or <u>branch wake</u>, Σ_B', as shown in Figure 8.

Next let Σ_0 become infinitesimally close to the surfaces of the fuselage and wakes (including the branch wake). Note that in this process, the closed surface, Σ_W', surrounding each wake is replaced by the two sides of an open surface Σ_W' such that $\Sigma_W' = \Sigma_R' + \Sigma_B'$. For this case

$$\oiint_{\Sigma_W'} \frac{\partial \varphi}{\partial n} \frac{1}{r} \, d\Sigma \rightarrow \iint_{\Sigma_W'} \Delta \left(\frac{\partial \varphi}{\partial n}\right) \frac{1}{r} \, d\Sigma = 0 \tag{56}$$

since $\Delta \left(\dfrac{\partial \varphi}{\partial n}\right) = 0$, whereas

$$\oiint_{\Sigma_W'} \varphi \, \frac{\partial}{\partial n}\left(\frac{1}{r}\right) d\Sigma \rightarrow \iint_{\Sigma_W'} \Delta \varphi \, \frac{\partial}{\partial n}\left(\frac{1}{r}\right) d\Sigma \tag{57}$$

Therefore, in the limit, Equation (54) reduces to*

$$4\pi E_* \varphi_* = -\oiint_{\Sigma_F + \Sigma_R} \left[\frac{\partial \varphi}{\partial n} \frac{1}{r} - \varphi \, \frac{\partial}{\partial n}\left(\frac{1}{r}\right)\right] d\Sigma + \iint_{\Sigma_F' + \Sigma_B' + \Sigma_R'} \Delta \varphi \, \frac{\partial}{\partial n}\left(\frac{1}{r}\right) d\Sigma \tag{58}$$

---

* Note that the wake surfaces Σ_F', Σ_B', and Σ_R' are open surfaces. The source integrals on the wake surfaces are identically equal to zero since the values of $\partial \varphi / \partial n$ on the opposite sides of these surfaces are equal to zero.

35

Figure 8. Surfaces Σ_F, Σ_R, Σ'_F, Σ'_R, and Σ'_B.
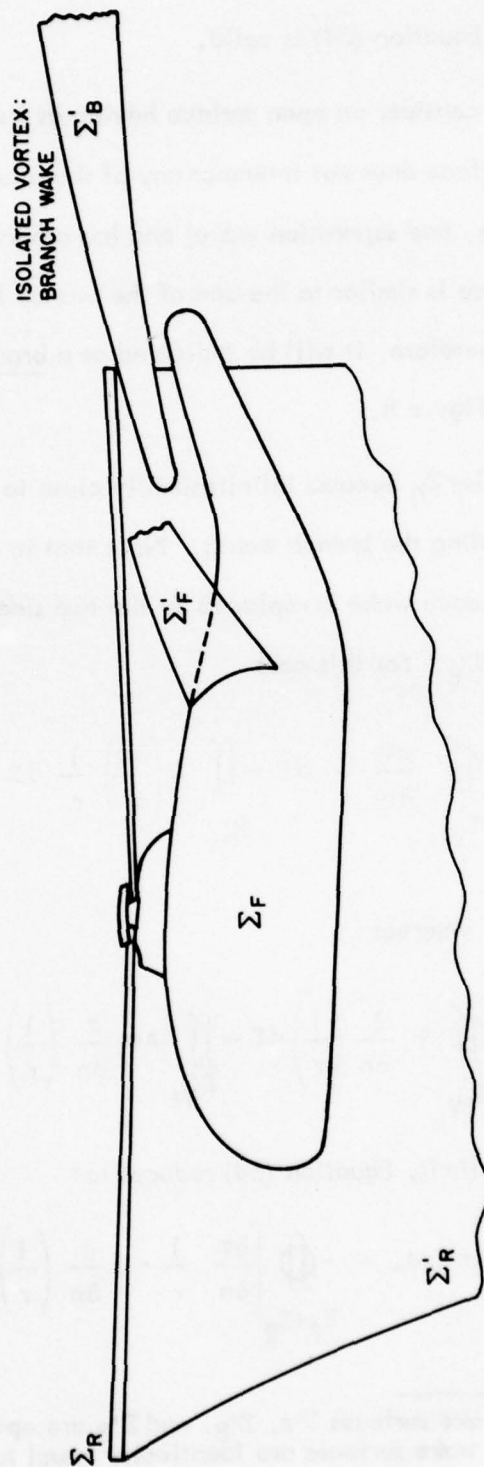
where Σ_F is the (closed) surface of the fuselage, Σ_R is the (closed) surface of the rotor blades, Σ'_F is the (open) surface of the body wake (emanating from the separation line), Σ'_B is the (open) surface of the branch wake, and Σ'_R represents the wakes of the rotor blades (see Figure 8). Furthermore (see Equation (15)),

$$\Delta\varphi = \varphi_1 - \varphi_2 \tag{59}$$

while $\bar{n}$ is the normal on the side 1 of the wake. Note that $\Delta\varphi$ is known from Equation (32), on Σ'_F and Σ'_B, while $\Delta\varphi$ is constant and equal to the vortex intensity on Σ'_B (Appendix A). Note also that the vortex-layer wake of the fuselage and rotor are represented as a doublet layer. The proof of the equivalence of doublet layers and vortex layers is briefly outlined in Reference 40.

In addition, if P_* is on $\Sigma_F + \Sigma_R$ then, as shown in Reference 23, $E_* = 1/2$. Thus, Equation (55) may be rewritten as

$$
\begin{aligned}
E_* = E(P_*) &= 1 && (P_* \text{ outside } \Sigma_F + \Sigma_R) \\
&= 1/2 && (P_* \text{ on } \Sigma_F + \Sigma_R) \\
&= 0 && (P_* \text{ inside } \Sigma_F + \Sigma_R)
\end{aligned} \tag{60}
$$

Note that on Σ_F and Σ_R, $\partial\varphi/\partial n$ is prescribed by the boundary conditions of Equation (30). Thus for P_* on $\Sigma_F + \Sigma_R$, Equation (54) is an integral equation relating φ to the prescribed $\partial\varphi/\partial n$. That equation is used to analyze the potential flow for interaction of fuselage, rotor, and wakes in the presence of flow separation.

3.7 ALTERNATIVE TREATMENT OF THE ISOLATED VORTEX

An alternative treatment of the isolated vortex is presented here. This treatment is similar to the formulation of rotational aerodynamics presented in Reference 30, and the derivation of this treatment could be obtained from that reference.

37

However, since the vorticity is represented by a single vortex, the same results may be obtained directly from Equation (58).

Note that combining Equations (33) and (58), one obtains

$$\bar{v} = \bar{\nabla}_{\star}\varphi = \bar{\nabla}_{\star}\oiint_{\Sigma_F + \Sigma_R} \left[\frac{\partial\varphi}{\partial n}\left(\frac{-1}{4\pi r}\right) - \varphi\,\frac{\partial}{\partial n}\left(\frac{-1}{4\pi r}\right) \right] d\Sigma$$

$$+ \bar{\nabla}_{\star}\iint_{\Sigma'_F + \Sigma'_B + \Sigma'_R} \Delta\varphi\,\frac{\partial}{\partial n}\left(\frac{1}{r}\right) d\Sigma \tag{61}$$

Equation (61) may be rewritten as

$$\bar{v} = \bar{\nabla}_{\star}\check{\varphi} + \bar{v}_{\Gamma} \tag{62}$$

where $\bar{v}_{\Gamma}$ is the velocity induced by the isolated vortex (with $\Delta\varphi = \Gamma$; see Equations (A-26) and (A-27) of Appendix A),

$$\bar{v}_{\Gamma} = \Gamma\bar{\nabla}_{\star}\iint_{\Sigma'_B} \frac{\partial}{\partial n}\left(\frac{-1}{4\pi r}\right) d\Sigma \tag{63}$$

while $\check{\varphi}$ is the potential in absence of the isolated vortex, which therefore satisfies the equation

$$4\pi E_{\star}\check{\varphi}_{\star} = \oiint_{\Sigma_F + \Sigma_R} \left[\frac{\partial\check{\varphi}}{\partial n}\left(\frac{-1}{4\pi r}\right) - \check{\varphi}\,\frac{\partial}{\partial n}\left(\frac{-1}{4\pi r}\right) \right] d\Sigma$$

$$+ \iint_{\Sigma'_F + \Sigma'_R} \Delta\check{\varphi}\,\frac{\partial}{\partial n}\left(\frac{1}{r}\right) d\Sigma \tag{64}$$

38

Note that the boundary condition on $\overset{\vee}{\varphi}$ is different from the one on φ, for, according to Equations (14), (34) and (40), the boundary condition for $\overset{\vee}{\varphi}$ is

$$\frac{\partial \overset{\vee}{\varphi}}{\partial n} = (-U_\infty \bar{i} - \bar{v}_\Gamma + \bar{v}_B) \cdot \bar{n} \tag{65}$$

Note that in this formulation $\bar{v}_B$ appears only in the boundary conditions. Also, according to Equations (62), (A-27), and (A-30),

$$\bar{v}_\Gamma = \Gamma \oint \bar{\nabla} \left(\frac{-1}{4\pi r} \right) \times d\bar{\ell} \tag{66}$$

Equation (66) implies the evaluation of a vortex line integral while Equation (63) (and thus the preceding formulation) requires the evaluation of a doublet layer integral. The last is much more lengthy than the first one. Therefore, the formulation presented here is preferable for the analysis of the problem considered here.

A further advantage is that the formulation may be easily extended to the case in which the vorticity is represented by a continuous distribution. For this case this formulation is still valid if Equation (66) is replaced by (see Reference 30)

$$\bar{v}_\Gamma = \bar{\nabla}_* \times \iiint \bar{\varsigma} \frac{-1}{4\pi r} \, dV \tag{67}$$

For the above reasons the formulation presented in this subsection is used in the remainder of this report.

3.8   CONDITIONS AT INFINITY

In this subsection Equations (50) and (51) are verified. Note that as r goes to infinity, Equation (52) yields

39

$$\lim_{R \to \infty} R\, \varphi_* = \lim_{R \to \infty} R \oiint_{\Sigma_0} \left[\frac{\partial \varphi}{\partial n} \left(\frac{-1}{4\pi r} \right) - \varphi \frac{\partial}{\partial n} \left(\frac{-1}{4\pi r} \right) \right] d\Sigma$$

$$= \lim_{R \to \infty} R \left[\frac{1}{4\pi r} \oiint_{\Sigma_0} \frac{\partial \varphi}{\partial n} \, d\Sigma - \frac{1}{4\pi r^2} \oiint_{\Sigma_0} \varphi \frac{\overline{r} \cdot \overline{n}}{r} \, d\Sigma \right] = 0 \tag{68}$$

since the flux through Σ_0 is equal to zero, i.e.,

$$\oiint \frac{\partial \varphi}{\partial n} \, d\Sigma = 0 \tag{69}$$

while

$$\lim_{R \to \infty} \oiint \varphi \frac{\overline{r} \cdot \overline{n}}{r} \, d\Sigma = \text{finite.} \tag{70}$$

Equation (58) implies

$$\varphi = \frac{C}{r^2} + O(r^{-3}) \quad \text{at } \infty \tag{71}$$

and

$$\frac{\partial \varphi}{\partial n} = \frac{D}{r^3} + O(r^{-4}) \text{ at } \infty. \tag{72}$$

SECTION 4

WAKE DYNAMICS

In this section, the fundamental aspects of wake dynamics are presented. These require some basic concepts on the dynamics of vortex layers. Also, it should be noted that vortex layers are not used in Program SOUSSA, which deals only with source and doublet layers. However, it may be shown that a vortex layer (and isolated vortices) may be represented by a doublet layer. Therefore, discussion on doublet and vortex layers is presented in Appendix A as background material; source layers are also included. Here vorticity dynamics are presented and finally the results are applied to the wake dynamics.

4.1 VORTICITY DYNAMICS

In order to formulate the wake dynamics problem, it is necessary to reformulate some classical results on vorticity dynamics in a novel fashion that is particularly suitable for the analysis of wake dynamics.

Consider the equilibrium equation for an inviscid fluid (Euler's equation)

$$\frac{D\bar{V}}{Dt} = -\frac{1}{\rho}\bar{\nabla}p \tag{73}$$

Note that

$$\frac{D\bar{V}}{Dt} = \frac{\partial \bar{V}}{\partial t} + (\bar{V}\cdot\bar{\nabla})\bar{V}$$

$$= \frac{\partial \bar{V}}{\partial t} + \frac{1}{2}\bar{\nabla}(\bar{V}\cdot\bar{V}) + \bar{\zeta}\times\bar{V} \tag{74}$$

41

where

$$\bar{\zeta} = \bar{\nabla} \times \bar{V} \tag{75}$$

Taking the curl of Equation (73) yields, for incompressible flow

$$\bar{\nabla} \times \frac{D\bar{V}}{Dt} = 0$$

or, according to Equations (74) and (75)

$$\frac{\partial \bar{\zeta}}{\partial t} + \bar{\nabla} \times (\bar{\zeta} \times \bar{V}) = 0 \tag{76}$$

Equation (76) may be rewritten in a more useful form by noting that (Reference 41, page 43)

$$\bar{\nabla} \times (\bar{a} \times \bar{b}) = (\bar{b} \cdot \bar{\nabla})\bar{a} - (\bar{a} \cdot \bar{\nabla})\bar{b} - \bar{b}(\bar{\nabla} \cdot \bar{a}) + \bar{a}(\bar{\nabla} \cdot \bar{b}) \tag{77}$$

and, therefore, combining Equations (76) and (77) and noting that $\bar{\nabla} \cdot \bar{\zeta} = 0$ and $\bar{\nabla} \cdot \bar{V} = 0$ (incompressible flow), yields

$$\frac{\partial \bar{\zeta}}{\partial t} + (\bar{V} \cdot \bar{\nabla})\bar{\zeta} - (\bar{\zeta} \cdot \bar{\nabla})\bar{V} = 0 \tag{78}$$

or

$$\frac{D\bar{\zeta}}{Dt} = (\bar{\zeta} \cdot \bar{\nabla})\bar{V} \tag{79}$$

Equation (79) is a classical result known as the third vortex theorem. Equation (79) may be integrated in closed form as shown in Reference 41, page 80. However, a novel method of solution was obtained in Reference 30 and is briefly

- 42

presented here since this new result facilitates the discussion on wake dynamics. Note first that by introducing a system of curvilinear coordinates, ξ^α, the vector $\bar{\zeta}$ may be written as (Reference 30)

$$\bar{\zeta} = \zeta^\alpha \, \bar{g}_\alpha \tag{80}$$

where

$$\bar{g}_\alpha = \frac{\partial \bar{X}}{\partial \xi^\alpha} \qquad\qquad \alpha = 1, 2, 3 \tag{81}$$

are the base vectors, while ζ^α are the contravariant components of the vector $\bar{\zeta}$. Note that

$$\zeta^\alpha = \bar{\zeta} \cdot \bar{g}^\alpha \tag{82}$$

where

$$\bar{g}^\alpha = g^{\alpha\beta} \, \bar{g}_\beta \tag{83}$$

with

$$g^{\alpha\beta} g_{\beta\gamma} = \delta^\alpha_\gamma \tag{84}$$

where δ^α_γ is the Kronecker delta and $g_{\beta\gamma}$ is the metric tensor given by

$$g_{\beta\gamma} = \bar{g}_\beta \cdot \bar{g}_\gamma \tag{85}$$

Note that

$$\frac{D\bar{\zeta}}{Dt} = \frac{D\zeta^\alpha}{Dt} \, \bar{g}_\alpha + \zeta^\alpha \, \frac{D\bar{g}_\alpha}{Dt} \tag{86}$$

43

Next assume that the coordinate system, ξ^α, moves with the fluid. Such a system describes the motion from a Lagrangian (rather than Eulerian) point of view; therefore, it may be called a Lagrangian coordinate system. Such a system is also called a material coordinate system (since at any time the point, $\xi^\alpha = $ constant, represents a material point) or convected coordinate system (since the coordinate points are convected by the system). Note that, in this coordinate system, the total time derivative coincides with the partial time derivative, since the total time derivative is, by definition, the time derivative in a system moving with the fluid. Therefore,

$$\frac{D\overline{g}_\alpha}{Dt} = \frac{\partial}{\partial t} \, \overline{g}_\alpha \, (\xi^1, \xi^2, \xi^3, t)$$

$$= \frac{\partial^2}{\partial \xi^\alpha \partial t} \, \overline{X}(\xi^1, \xi^2, \xi^3, t) = \frac{\partial \overline{V}}{\partial \xi^\alpha} \tag{87}$$

Hence,

$$\zeta^\alpha \frac{D\overline{g}_\alpha}{Dt} = \zeta^\alpha \frac{\partial \overline{V}}{\partial \xi^\alpha} = (\overline{\zeta} \cdot \overline{\nabla}) \overline{V} \tag{88}$$

and Equation (86) may be rewritten as

$$\frac{D\overline{\zeta}}{Dt} = \frac{D\zeta^\alpha}{Dt} \, \overline{g}_\alpha + (\overline{\zeta} \cdot \overline{\nabla}) \overline{V} \tag{89}$$

Comparing with Equation (79) one obtains

$$\frac{D\zeta^\alpha}{Dt} \, \overline{g}_\alpha = 0 \tag{90}$$

or

$$\frac{D\zeta^\alpha}{Dt} = \frac{\partial}{\partial t} \, \zeta^\alpha (\xi^1, \xi^2, \xi^3, t) = 0 \tag{91}$$

44

i.e.,

$$\zeta^\alpha(\xi^1, \xi^2, \xi^3, t) = \zeta^\alpha(\xi^1, \xi^2, \xi^3, 0) \tag{92}$$

Equation (92) indicates that in a Lagrangian coordinate system, ζ^α is only a function of ξ^α; i.e., ζ^α is a function of the material point and not of time. In particular, in steady state, ζ^α is constant along a streamline.

The result obtained above yields two important properties of flow fields:

(a)   A particle or a portion of fluid initially irrotational remains irrotational at all times (Lagrange-Cauchy theorem).

(b)   Vortex lines are material lines, i.e., the set of particles that composes a vortex line at one instant will continue to form a vortex line at later instants.

The first property is an immediate consequence of Equation (91). In order to prove the second one, consider a material line, L_M, described by a parameter $\varkappa$,

$$\overline{X} = \overline{X}[\xi^\alpha(\varkappa), t] = \overline{X}(\varkappa, t) \tag{93}$$

which at time $t = 0$ coincides with a vortex line, i.e., $\overline{\zeta}$ is tangent to L_M, or

$$\overline{\zeta}(\varkappa, 0) = \overline{\zeta}[\xi^\alpha(\varkappa), 0] = \lambda_0(\varkappa) \frac{\partial \overline{X}}{\partial \varkappa}[\xi^\alpha(\varkappa), 0] \tag{94}$$

Then the proof of property (b) consists of showing that $\overline{\zeta}$ remains parallel to L_M at all times. Note first that Equation (94) is equivalent to

$$\zeta^\alpha[\xi^\alpha(\varkappa), 0] \, \overline{g}_\alpha[\xi^\alpha(\varkappa), 0] = \lambda_0 \frac{\partial \overline{X}}{\partial \xi^\alpha} \frac{\partial \xi^\alpha}{\partial \varkappa}$$

$$= \lambda_0(\varkappa) \frac{\partial \xi^\alpha}{\partial \varkappa}(\varkappa) \, \overline{g}_\alpha[\xi^\alpha(\varkappa), 0] \tag{95}$$

45

or

$$\zeta^{\alpha}[\xi^{\alpha}(\varkappa), 0] = \lambda_0(\varkappa) \frac{\partial \xi^{\alpha}}{\partial \varkappa}(\varkappa) \tag{96}$$

At time t, using Equations (92) and (96) results in

$$\overline{\zeta}(\varkappa, t) = \zeta^{\alpha}[\xi^{\alpha}(\varkappa), t] \, \overline{g}_{\alpha}[\xi^{\alpha}(\varkappa), t]$$

$$= \zeta^{\alpha}[\xi^{\alpha}(\varkappa), 0] \, \overline{g}_{\alpha}[\xi^{\alpha}(\varkappa), t]$$

$$= \lambda_0(\varkappa) \frac{\partial \xi^{\alpha}}{\partial \varkappa}(\varkappa) \, \overline{g}_{\alpha}[\xi^{\alpha}(\varkappa), t]$$

$$= \lambda_0(\varkappa) \frac{\partial \overline{X}}{\partial \varkappa}[\xi^{\alpha}(\varkappa), t] \tag{97}$$

Equation (97) indicates that $\overline{\zeta}$ remains parallel to the material line, L_M, and, therefore, vortex lines are material lines.

An additional result (on vortex stretching) may be obtained from Equation (97). Consider an element, $d\overline{\ell}$, of the vortex line, given by

$$d\overline{\ell} = \frac{\partial \overline{X}}{\partial \varkappa} \, d\varkappa \tag{98}$$

Then Equation (97) indicates that

$$\frac{|\zeta|}{|d\ell|} = \frac{|\zeta|_0}{|d\ell|_0} \tag{99}$$

which is the well-known vortex-stretching law for incompressible fluid; the ratio

46

between the intensity, $|\zeta|$, of the vorticity and the length, $|d\ell|$, of the vortex element remains constant in time.*

4.2   WAKE DYNAMICS

In the formulation presented in Section 3, the wakes are represented as doublet layers. On the other hand, it is shown in Appendix A that doublet layers are equivalent to vortex sheets. Also, a vortex sheet may be thought of as the limiting use of a distribution of vorticity in a thin volume surrounding the vortex sheet. This is very close to the physical reality; the wake is actually the volume of the flow field where the vorticity generated by the presence of the aircraft is not negligible.

The above considerations indicate that the results obtained in Subsection 4.1 are applicable to the analysis of the dynamics of the doublet layer wake. The first consequence is that the points of the wake may be considered as material points. However, the velocity flow field is discontinuous through a doublet layer and, therefore, the velocity of a point of the wake is not clearly defined. It was Helmholtz who first suggested that the velocity of a point on the wake is the average of the values on the two sides of the wake

$$\overline{V}_A = \frac{\overline{V}_1 + \overline{V}_2}{2} \tag{100}$$

This result may be obtained by evaluating the velocity of a point on the wake in the limiting use as the thin layer of vorticity reduces to a vortex sheet. Also, this is in agreement with the result obtained in Section 3 where it was shown that (see Equation (31))

---

*Note that the same result is obtained from Kelvin's theorem, which yields in the limit,

$$\Gamma = \oint \nabla \cdot d\overline{s} = \zeta dV/d\ell = \text{constant}$$

47

$$\frac{D_A(\Delta\varphi)}{Dt} = 0 \tag{101}$$

where

$$\frac{D_A}{Dt} = \frac{\partial}{\partial t} + \overline{V}_A \cdot \overline{\nabla} \tag{102}$$

may now be interpreted as the total derivative for a material point on the wake.

Based on the above discussion, the following procedure may be used to evaluate the geometry of the wake. First, a point on the wake is a material point having velocity, V_A. Therefore, given its location $\overline{x}_M$ at this time, t_o, the new location at time $t_o + dt$ is given by

$$\overline{x}_M(t_o + dt) = \overline{x}_M(t_o) + \overline{V}_A\, dt \tag{103}$$

This yields the geometry of the wake at any time t. Furthermore, Equation (101) indicates that $\Delta\varphi$ is a function of $\overline{x}_M$ but not of time. Therefore, the distribution of $\Delta\varphi$ on the wake is immediately available once the location of each material point is obtained.

Summarizing, the dynamics of the wake is solved by following the locations of the material points in time and by the fact that using the value of $\Delta\varphi$ corresponding to each material point does not change in time.

48

SECTION 5

NUMERICAL FORMULATION

The numerical formulation used to approximate Equation (58) with a system of algebraic equations is presented in this section. In summary, the procedure is as follows. The surfaces of the rotor, fuselage and their respective wakes are divided into small surface elements, Σ_i. The potential φ and the normal wash Ψ are assumed to be constant within each element. This yields a set of linear delay equations relating the values of the potential, φ_n, at the centroids of the elements, Σ_n, to the values of the normal wash, Ψ_n, at the centroids of the elements, Σ_n. The coefficients are evaluated analytically for quadrilateral hyperboloidal elements.

5.1 APPROXIMATION OF INTEGRAL EQUATION

For the geometry used in deriving Equation (58) (see Figure 8), divide the surfaces of fuselage and rotor Σ_F and Σ_R, into N surface elements Σ_n. Also, divide the surfaces of their wakes, Σ_F' and Σ_R' into M surface elements Σ_m'. Then Equation (58) may be rewritten as:

$$2E(P*,t)\, \varphi\,(P*,t) = \sum_{n-1}^{N} \Psi_n(t) \iint_{\Sigma_n(t)} \frac{-1}{2\pi r}\, d\Sigma_n$$

$$+ \sum_{n-1}^{N} \Psi_n(t) \iint_{\Sigma_n(t)} \frac{\partial}{\partial n} \left(\frac{1}{2\pi r}\right) d\Sigma_n$$

$$+ \sum_{m=1}^{M} \Delta\varphi_m(t) \iint_{\Sigma_m(t)} \frac{\partial}{\partial n} \left(\frac{1}{2\pi r}\right) d\Sigma_m' \qquad (104)$$

49

or

$$2 E (P_*, t) \varphi (P_*, t) = \sum_{n=1}^{N} B_n (P_*, t) \Psi_n (t)$$

$$+ \sum_{n=1}^{N} C_n (P_*, t) \varphi_n (t)$$

$$+ \sum_{m=1}^{M} F_m (P_*, t) \Delta \varphi_m (t) \qquad (105)$$

where

$$\Psi_n = \left. \frac{\partial \varphi}{\partial n} \right|_{P = P_n} \qquad (106)$$

and

$$B_n (P_*, t) = \iint_{\Sigma_n(t)} \frac{-1}{2 \pi r} \, d \Sigma_n$$

$$C_n (P_*, t) = \iint_{\Sigma_n (t)} \frac{\partial}{\partial n} \left(\frac{1}{2 \pi r} \right) d \Sigma_n$$

$$F_m (P_*, t) = \iint_{\Sigma'_m (t)} \frac{\partial}{\partial n} \left(\frac{1}{2 \pi r} \right) d \Sigma'_m \qquad (107)$$

By imposing the condition that Equation (105) be satisfied at the centroids P_h of the elements Σ_h, one obtains (note that according to Equation (60) $E(P_h) = 1/2$, since P_h is on $\Sigma_F + \Sigma_R$),

$$\varphi_h(t) = \sum_{n=1}^{N} B_{hn}(t) \, \Psi_n(t) + \sum_{n=1}^{N} C_{hn}(t) \, \varphi_n(t) + \sum_{m=1}^{M} F_{hm}(t) \, \Delta \varphi_m(t) \qquad (108)$$

50

where

$$B_{hn}(t) = B_n (P_h, t)$$
$$C_{hn}(t) = C_n (P_h, t)$$
$$F_{hm}(t) = F_m (P_h, t)$$

(109)

It should be emphasized that (unlike in the formulation for aircraft, Reference 42) the coefficients B_{hn}, C_{hn}, and F_{hm} are time dependent. This is due to the fact that the surfaces Σ_n and Σ'_m vary with time (except for the ones of the fuselage) and also to the fact that the points P_h move in time (except for those on the fuselage).

Next the relationship between $\Delta\varphi_m$ and φ_n is obtained. Consider the trajectory of the centroid, P'_m, of the element Σ'_m of the wake. Let P_m^{TE} indicate the point of the trailing edge from which the above trajectory starts (see Figure 9). Then, according to Equation (32),

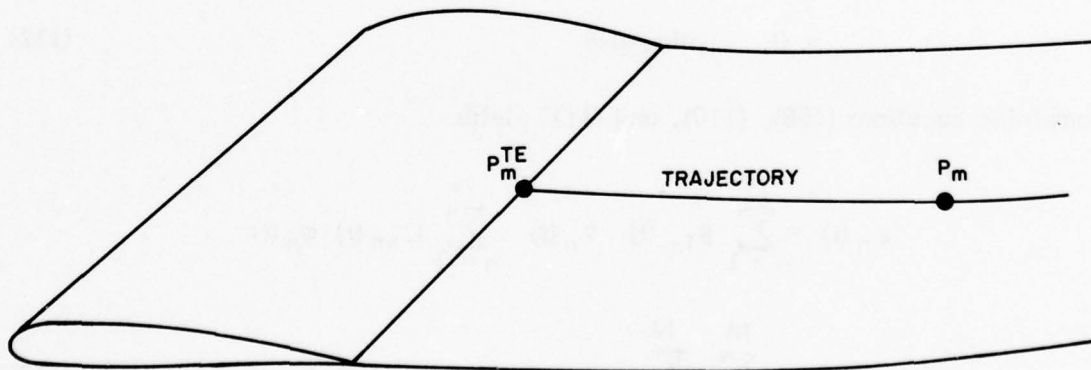$$\Delta\varphi_m(t) = \Delta\varphi_m^{TE} (t - \tau_m)$$

(110)

Figure 9. Relation of Wake Trajectory to Trailing Edge.

51

where $\Delta\varphi_m^{TE}$ is the value of $\Delta\varphi$ at P_m^{TE}, whereas τ_m is the time necessary for the material point of the wake to move from P_m^{TE} to P_m' with velocity $\bar{V}_A$ given by Equation (25).

In addition, it is possible to express the value of $\Delta\varphi_m^{TE}$ in terms of the values, φ_n, of the potential at the centroids of the elements, Σ_n. A simple expression is obtained by assuming that (in view of the Kutta condition) the value of $\Delta\varphi_m^{TE}$ may be approximated with the value of $\Delta\varphi$ at the centroids of the elements in contact with the point P_m^{TE}. This yields

$$\Delta\varphi_m^{TE}(t) = \sum S_{mn}\,\varphi_n(t) \tag{111}$$

where S_{mn} is equal to 1 (-1) for the point of the upper-surface (lower-surface) element in contact with the point P_m^{TE} of the trailing edge and equal to zero otherwise. In other words,

$$S_{mn} = 1 \qquad \text{if } P_m^{TE} \in \Sigma_n \text{ (on upper surface)}$$

$$= -1 \qquad \text{if } P_m^{TE} \in \Sigma_n \text{ (on lower surface)}$$

$$= 0 \qquad \text{otherwise} \tag{112}$$

Combining Equations (108), (110), and (111) yields

$$\varphi_n(t) = \sum_{n=1}^{N} B_{hn}(t)\,\psi_n(t) + \sum_{n=1}^{N} C_{hn}(t)\,\varphi_n(t)$$

$$+ \sum_{m=1}^{M} \sum_{n=1}^{N} F_{hm}(t)\,S_{mn}\,\varphi_n(t-\tau_m) \tag{113}$$

This is a system of linear delay equations with time-dependent coefficients that may be solved with a step-by-step procedure, once the coefficients $B_{hn}(t)$, $C_{hn}(t)$, and $F_{hm}(t)$ have been evaluated. An explicit expression for these coefficients is given in Subsection 5.2. An alternative iterative procedure for the solution of Equation (113) is presented in Subsection 5.3.

5.2   ANALYTICAL EXPRESSION FOR COEFFICIENTS B_{hn}, C_{hn}, F_{hm}

Consider the coefficients $B_{hn}(t)$ and $C_{hn}(t)$ that, according to Equation (107) and (109), are given by

$$B_{hn}(t) = \iint_{\Sigma_n(t)} \frac{-1}{2\pi r} \, d\Sigma_n \tag{114}$$

$$C_{hn}(t) = \iint_{\Sigma_n(t)} \frac{\partial}{\partial_n}\left(\frac{1}{2\pi r}\right) d\Sigma_n = \iint_{\Sigma_n(t)} \frac{-1}{2\pi r^3} \, r \cdot n \, d\Sigma_n \tag{115}$$

where $r = |\bar{r}|$ with

$$\bar{r} = \bar{P}(t) - \bar{P}_h(t). \tag{116}$$

$\bar{P}_h(t)$ is the centroid of the element $\Sigma_h(t)$, whereas $\bar{P}(t)$ is the dummy point of integration on the element $\Sigma_n(t)$. The integrals in Equations (114) and (115) may be evaluated analytically if the surface element $\Sigma_n(t)$ is quadrilateral and is approximated by the hyperboloidal element of Reference 43, i.e., the portion of a hyperboloidal paraboloid of the type (see Figure 10),

$$\bar{P}(t) = \bar{P}_0(t) + \xi \bar{P}_1(t) + \eta \bar{P}_2(t) + \xi \eta \bar{P}_3(t) \tag{117}$$
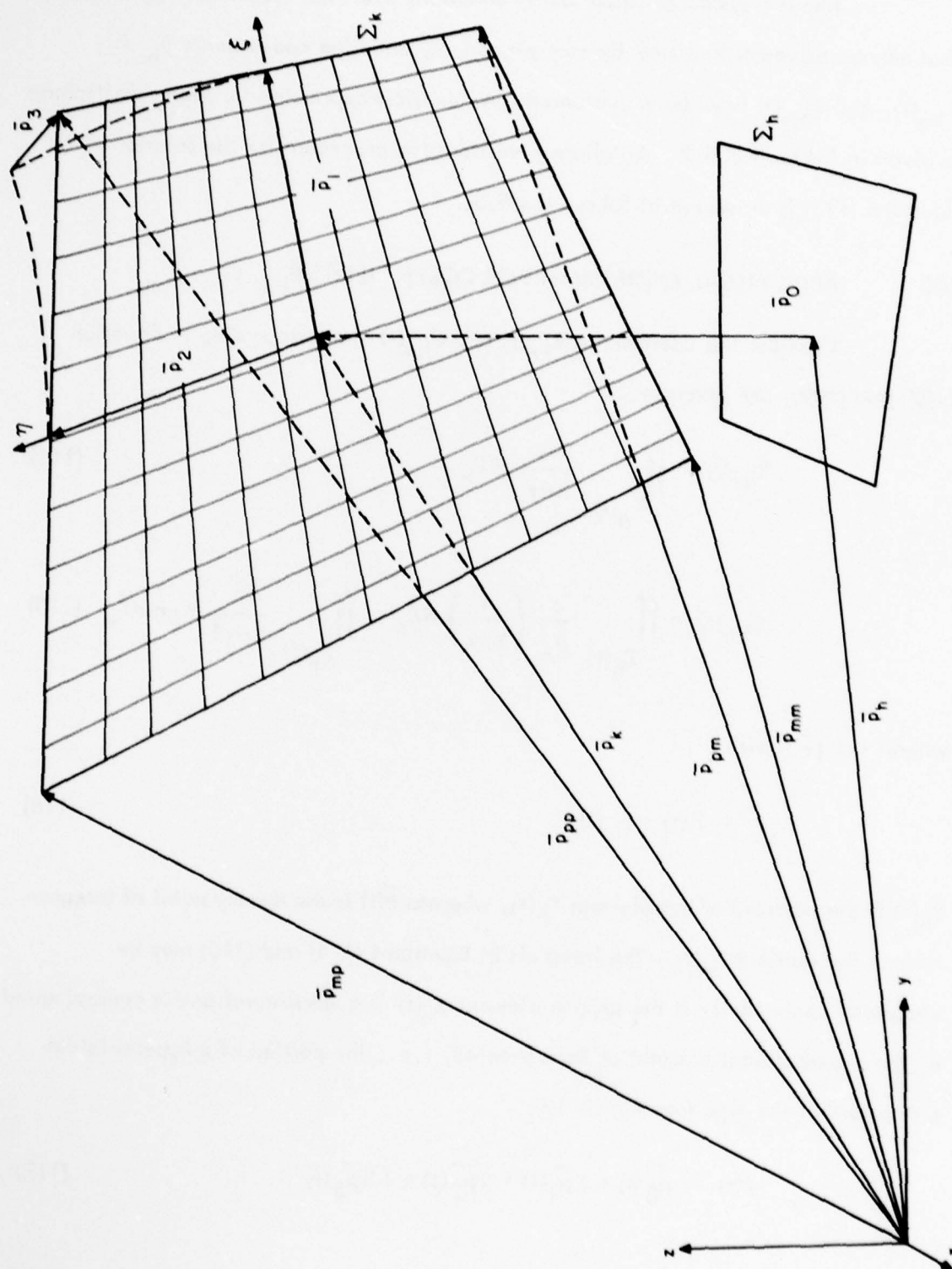
Figure 10. Hyperboloidal Element.

where the surface coordinates ξ and η are bounded by

$$-1 \le \xi \le 1$$
$$-1 \le \eta \le 1$$

(118)

The vectors $\bar{p}_0(t)$, $\bar{p}_1(t)$, $\bar{p}_2(t)$, and $\bar{p}_3(t)$ are related to the corner points $\bar{p}_{pp}(t)$, $\bar{p}_{pm}(t)$, $\bar{p}_{mp}(t)$, and $\bar{p}_{mm}(t)$ of the element $\Sigma_n(t)$ by the relationship

$$\begin{Bmatrix} \bar{p}_0(t) \\ \bar{p}_1(t) \\ \bar{p}_2(t) \\ \bar{p}_3(t) \end{Bmatrix} = 1/4 \begin{bmatrix} 1 & 1 & 1 & 1 \\ 1 & 1 & -1 & -1 \\ 1 & -1 & 1 & -1 \\ 1 & -1 & -1 & 1 \end{bmatrix} \begin{Bmatrix} \bar{p}_{pp}(t) \\ \bar{p}_{pm}(t) \\ \bar{p}_{mp}(t) \\ \bar{p}_{mm}(t) \end{Bmatrix}$$

(119)

Note that

$$d\Sigma_n = |\bar{a}_1 \times \bar{a}_2| \, d\xi \, d\eta$$

(120)

where $\bar{a}_i$ ($i = 1, 2$) are the surface base vectors

$$\bar{a}_1 = \partial \bar{P}/\partial \xi$$
$$\bar{a}_2 = \partial \bar{P}/\partial \eta$$

(121)

Note also that the surface unit normal $\bar{n}$ may be expressed as

$$\bar{n} = (\bar{a}_1 \times \bar{a}_2)\big/ |\bar{a}_1 \times \bar{a}_2|$$

(122)

Combining Equations (114), (115), (118), (120), and (122) yields

$$B_{hn}(t) = \int_{-1}^{1} \int_{-1}^{1} \frac{-1}{2\pi r} |\bar{a}_1 \times \bar{a}_2| \, d\xi \, d\eta$$

(123)

55

$$C_{hn}(t) = \int_{-1}^{1} \int_{-1}^{1} \frac{-1}{2\pi r^3} \, \bar{r} \cdot \bar{a}_1 \times \bar{a}_2 \, d\xi \, d\eta \quad . \tag{124}$$

Note that both integrals are of the type

$$I = \int_{-1}^{1} \int_{-1}^{1} f(\xi^1, \xi^2) \, d\xi \, d\eta \tag{125}$$

which may be evaluated as

$$I = F(1, 1) - F(1, -1) - F(-1, 1) + F(-1, -1) \tag{126}$$

where $F(\xi, \eta)$ is such that

$$\frac{\partial^2 F}{\partial \xi \partial \eta} = f(\xi, \eta) \tag{127}$$

Therefore, $B_{hn}(t)$ and $C_{hn}(t)$ are easily evaluated if one notes that (Reference 43)

$$\frac{1}{r^3} \, \bar{r} \cdot \bar{a}_1 \times \bar{a}_2 = \frac{\partial^2}{\partial \xi \partial \eta} \left[-\tan^{-1} \left(\frac{\bar{r} \times \bar{a}_1 \cdot \bar{r} \times \bar{a}_2}{|\bar{r}| \, \bar{r} \cdot \bar{a}_1 \times \bar{a}_2} \right) \right] \tag{128}$$

whereas, assuming $\bar{n}$ to be approximately constant within $\Sigma_n(t)$ *,

$$\frac{1}{r} \, |\bar{a}_1 \times \bar{a}_2| = \frac{\partial^2}{\partial \xi \partial \eta} \left[-\bar{r} \times \bar{a}_1 \cdot \bar{n} \, \frac{1}{|\bar{a}_1|} \, \sinh^{-1} \left(\frac{\bar{r} \cdot \bar{a}_1}{|\bar{r} \times \bar{a}_1|} \right) \right.$$

$$+ \bar{r} \times \bar{a}_2 \cdot \bar{n} \, \frac{1}{|\bar{a}_2|} \, \sinh^{-1} \left(\frac{\bar{r} \cdot \bar{a}_2}{|\bar{r} \times \bar{a}_2|} \right)$$

$$\left. + \bar{r} \cdot \bar{n} \, \tan^{-1} \left(\frac{\bar{r} \times \bar{a}_1 \cdot \bar{r} \times \bar{a}_2}{|\bar{r}| \, \bar{r} \cdot \bar{a}_1 \times \bar{a}_2} \right) \right] \quad . \tag{129}$$

---

*This is consistent with the hypothesis that φ and $\psi = \partial\varphi/\partial\eta$ are constant within Σ_n .

56

Next note that the definition of the coefficients $F_{hm}(t)$ is identical to the one for the coefficients $C_{hn}(t)$ with the exception that the surface elements Σ'_m are on the wake. Therefore, if the wake elements are approximated by quadrilateral hyperboloidal elements, the coefficients F_{hm} are evaluated by using the same procedure outlined for the coefficients C_{hn}.

5.3   ITERATIVE PROCEDURE FOR SOLUTION OF DELAY EQUATION

In order to solve Equation (113), a step-by-step procedure may be used; however, this is expected to be time consuming (because of limitations on Δt due to stability constraints usually connected with step-by-step procedures). Therefore, for the steady state (periodic) solution, an alternate scheme may be usefully employed. This scheme is based upon the following iterative procedure: for the zero[th] iteration, assume that the variation of $\Delta\varphi_m{}^{TE}$ in time is small enough so that

$$\varphi_n^{(0)}(t - \tau) \sim \varphi^{(0)}(t) \tag{130}$$

Introducing this approximation, Equation (113) reduces to

$$\left(\left[\delta_{hn} \right] - \left[C_{hn}(t) \right] - \left[F_{hm}(t) \right] \left[S_{mn} \right] \right) \left\{ \varphi_n^{(0)}(t) \right\} = \left[B_{hn}(t) \right] \left\{ \psi_n(t) \right\} \tag{131}$$

This is a system of algebraic equations (with time appearing as a parameter) that may be solved for $\varphi_n^{(0)}$ at discrete angular positions, χ_i, of the rotor, corresponding to time, $t_i = \chi_i/\Omega$ (where Ω is the angular velocity of the rotor). For the successive iterations, Equation (113) may be rewritten as

$$\left[\delta_{hn} - C_{hn}(t) \right] \left\{ \varphi_n^{(k)}(t) \right\} = \left[B_{hn}(t) \right] \left\{ \psi_n(t) \right\}$$
$$+ \left[F_{hm}(t) \right] \left[S_{mn} \right] \left\{ \varphi_n^{(k-1)}(t - \tau_m) \right\} . \tag{132}$$

57

If the iteration scheme converges, the converged values of $\varphi_n^{(k)}(t)$ are the solutions for Equation (113).

5.4   EVALUATION OF PERTURBATION VELOCITY AND PRESSURE

Equation (113) is a system of linear delay equations with time-dependent coefficients. After the potential φ at the centroid of each element is obtained, the perturbation velocities and pressure can be evaluated. As shown in Subsection 4.1, the velocity can be decomposed as follows:

$$\bar{v} = v_\alpha \, \bar{a}^\alpha \qquad \alpha = 1, 2, 3 \tag{133}$$

where $\bar{a}^\alpha$ denotes the adjoint base vector and v_α is the covariant component of the vector $\bar{v}$. Note that

$$v_\alpha = \frac{\partial \varphi}{\partial \xi^\alpha} \tag{134}$$

with ξ^α representing the curvilinear coordinates. If ξ and η are the surface curvilinear coordinates and $\bar{a}_1$ and $\bar{a}_2$ are the base vectors, Equation (133) becomes

$$\bar{v} = v_1 \bar{a}^1 + v_2 \bar{a}^2 + v_3 \bar{a}^3 \tag{135}$$

where

$$\bar{a}^1 = \frac{\bar{a}_2 \times \bar{a}_3}{\bar{a}_1 \cdot \bar{a}_2 \times \bar{a}_3} \tag{136}$$

$$\bar{a}^2 = \frac{\bar{a}_3 \times \bar{a}_1}{\bar{a}_1 \cdot \bar{a}_2 \times \bar{a}_3} \tag{137}$$

and

$$\bar{a}^3 = \frac{\bar{a}_1 \times \bar{a}_2}{\bar{a}_1 \cdot \bar{a}_2 \times \bar{a}_3} \tag{138}$$

58

since

$$a_{\alpha\beta} = \bar{a}_\alpha \cdot \bar{a}_\beta = a_{\beta\alpha} \tag{139}$$

$$a^{\gamma\beta} a_{\beta\alpha} = a_{\alpha\beta} a^{\beta\gamma} = \delta_\alpha^\gamma \tag{140}$$

with

$$\delta_\alpha^\gamma = \begin{cases} 1 & \alpha = \gamma \\ 0 & \alpha \neq \gamma \end{cases} \tag{141}$$

The perturbation velocities in Cartesian coordinates at the centroid of the element are given by

$$v_x = v_1 \bar{a}^1 \cdot \bar{i} + v_2 \bar{a}^2 \cdot \bar{i} + v_3 \bar{a}^3 \cdot \bar{i} \tag{142}$$

$$v_y = v_1 \bar{a}^1 \cdot \bar{j} + v_2 \bar{a}^2 \cdot \bar{j} + v_3 \bar{a}^3 \cdot \bar{j} \tag{143}$$

and

$$v_z = v_1 \bar{a}^1 \cdot \bar{k} + v_2 \bar{a}^2 \cdot \bar{k} + v_3 \bar{a}^3 \cdot \bar{k} \tag{144}$$

where $\bar{i}$, $\bar{j}$, and $\bar{k}$ are the unit base vectors.

Finally, Bernoulli's equation for incompressible potential flow, given by Equation (18), is used to obtain the pressure, that is,

$$\frac{\partial \Phi}{\partial t} + \frac{1}{2} |\bar{\nabla}_\Phi|^2 + \frac{p}{\rho} = \frac{1}{2} U_\infty^2 + \frac{p_\infty}{\rho} \tag{145}$$

or

$$C_p = \frac{p - p_\infty}{\frac{1}{2} \rho U_\infty^2} = - \frac{2 \frac{\partial \Phi}{\partial t} + 2 v_x U_\infty + v_x^2 + v_y^2 + v_z^2}{U_\infty^2} \tag{146}$$

where $\frac{\partial \Phi}{\partial t} = 0$ on body and $\frac{\partial \Phi}{\partial t} = \bar{\Omega} \times \bar{r} \cdot \bar{\nabla} \varphi$ on rotor.

59

5.5 EVALUATION OF THE AERODYNAMIC COEFFICIENTS

After the pressures have been obtained at the centroids of the aerodynamic panels, the aerodynamic coefficients can be obtained by summing the contribution of each surface panel. Hence, the lift on the helicopter is given by the expression

$$C_L = - \iint_\Sigma C_p \, \bar{n} \cdot \bar{k} \, d\Sigma$$

$$= - \sum \int_{-1}^{1} \int_{-1}^{1} C_p \, \bar{a}_1 \times \bar{a}_2 \cdot \bar{k} \, d\xi \, dy$$

$$\cong -4 \sum_h C_{p_h} (\bar{a}_1 \times \bar{a}_2 \cdot \bar{k})_h \qquad (147)$$

since

$$\int_{-1}^{1} \int_{-1}^{1} d\xi \, d\eta = 4 \qquad (148)$$

Similarly, the induced drag is given by

$$C_D = - \iint_\Sigma C_p \, \bar{n} \cdot \bar{i} \, d\Sigma$$

$$\cong -4 \sum_h C_{p_h} (\bar{a}_1 \times \bar{a}_2 \cdot \bar{i})_h \quad . \qquad (149)$$

Note that C_{p_h} denotes the pressure coefficient at the centroid of the hth element.

SECTION 6
RESULTS AND CONCLUSIONS

The formulation presented in Sections 3 and 4 for incompressible potential aerodynamics with separated flow was incorporated into a computer program SHAPES to study the rotor wake effects on hub pylon/flow separation. The program SHAPES is an acronym for Subsonic Helicopter Aerodynamic Program with Effects of Separation. The effects of the presence of the rotor in its various operating conditions as well as the presence of separation on the pressure of the helicopter components beneath the rotor were investigated. Extensive numerical results showing the flexibility and accuracy of the method were obtained from the program SHAPES. Also, comparison with several existing results was made. Concluding remarks are given in Subsection 6.3.

6.1 NUMERICAL RESULTS

Convergence analysis was performed on an ellipsoidal helicopter configuration. The case of a modified BO-105 helicopter fuselage configuration without rotor was analyzed to study the effects of separation. Results for a single-bladed rotor and four-bladed (XH-51A) rotor were obtained and compared with available theoretical/ experimental results. A fuselage configuration (Model 1) with a prescribed separation wake and a single two-bladed rotor with classical helicoidal wake geometry were treated separately and combined for analysis at forward flight, and compared with existing experimental results.

6.1.1 CONVERGENCE

Convergence studies were conducted to identify the approximate number of aerodynamics elements required for the analysis.

61

Convergence analyses were performed on an ellipsoidal fuselage configuration with separation effects at an airspeed of 150 mph, zero angle of attack, and zero sideslip angle. The overall length, width, and height of the fuselage were 41, 14.5, and 16.5 inches, respectively. Results are given in Figure 11. Two different aerodynamic paneling schemes were used: nonuniform and uniform elements.

Results for nonuniform elements are given in Figures 11(a) through 11(d); Figures 11(e) through 11(h) present corresponding results using uniform elements. Both the velocity potential and pressure distribution along the top fuselage centerline and the side of the fuselage were obtained. The four cases used for each aerodynamic panel breakup scheme were as follows:

Run	Symbol	Number of Elements
1	△	64
2	○	120
3	□	168
4	◇	200

It is noted that the geometric symmetry of the fuselage, i.e., left- and right-hand side, was not used, and the number of aerodynamic panels represents the total number of elements used. On the CDC 6600 computer systems, 250 seconds of computer time were required to run four cases.

It is seen that the use of the uniform elements yields slower convergence of the perturbation potential near the nose and tail sections of the fuselage. A slower rate of convergence is seen when the pressure distribution along the top centerline and the side of the fuselage is computed. Hence, the use of nonuniform elements is desirable, i.e., smaller panels near the nose and tail sections of the fuselage. It is
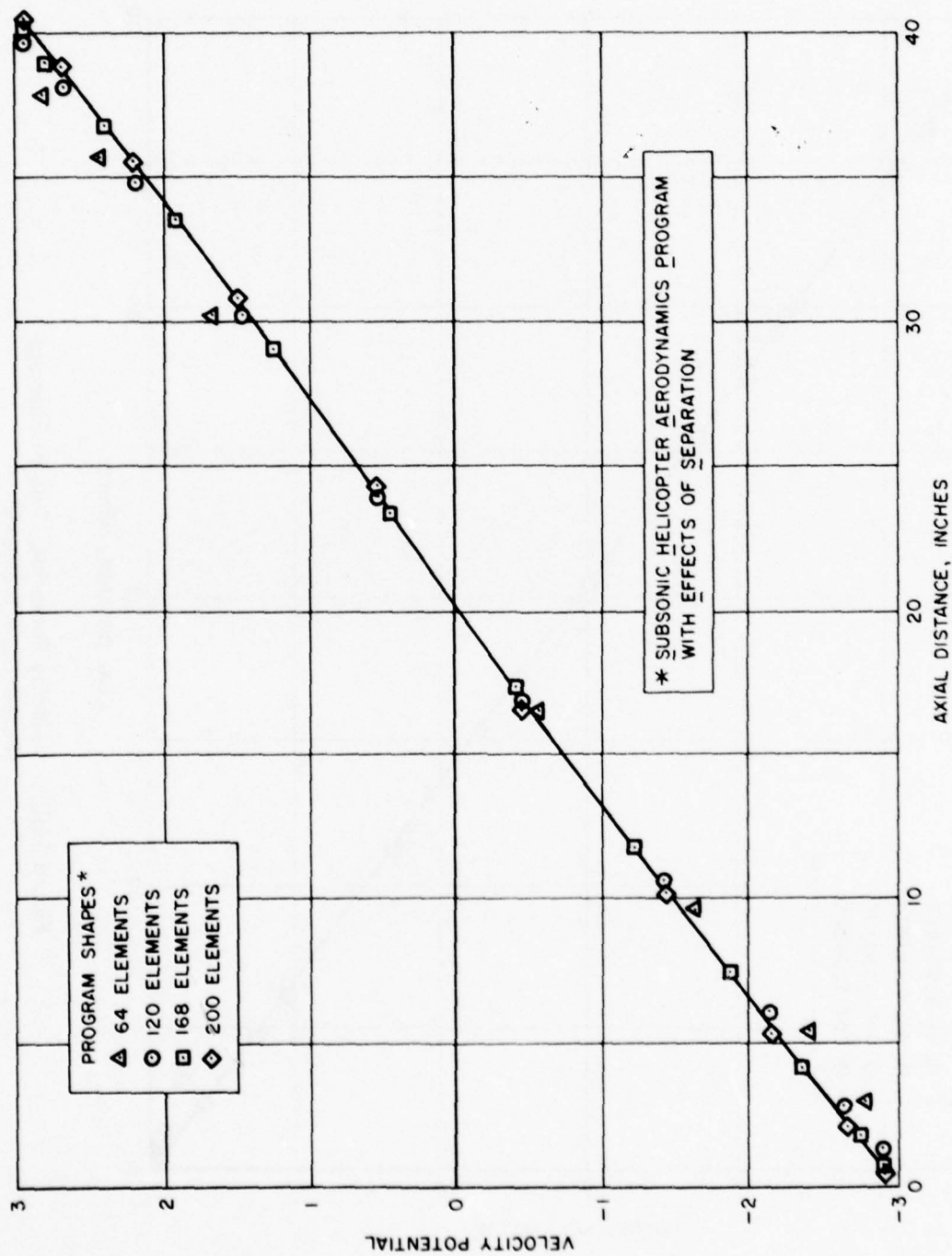
62

Figure 11(a). Velocity Potential, Top Centerline (Nonuniform Elements).

Figure 11(b). Velocity Potential, Side of Fuselage (Nonuniform Elements).

Figure 11(c). Pressure Coefficient, Top Centerline (Nonuniform Elements).

65

Figure 11(d). Pressure Coefficient, Side of Fuselage (Nonuniform Elements).

Figure 11(e). Velocity Potential, Top Centerline (Uniform Elements).

67
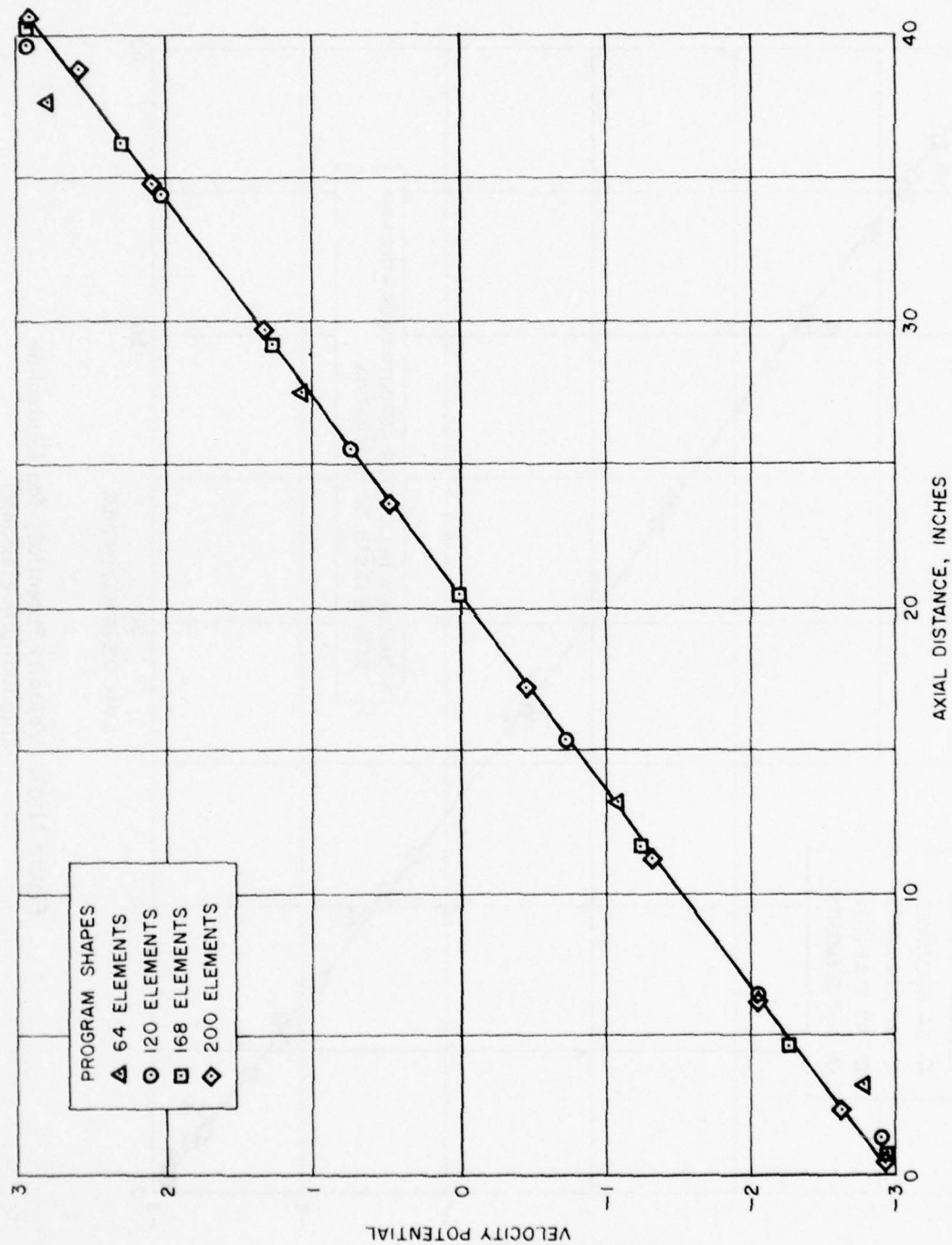
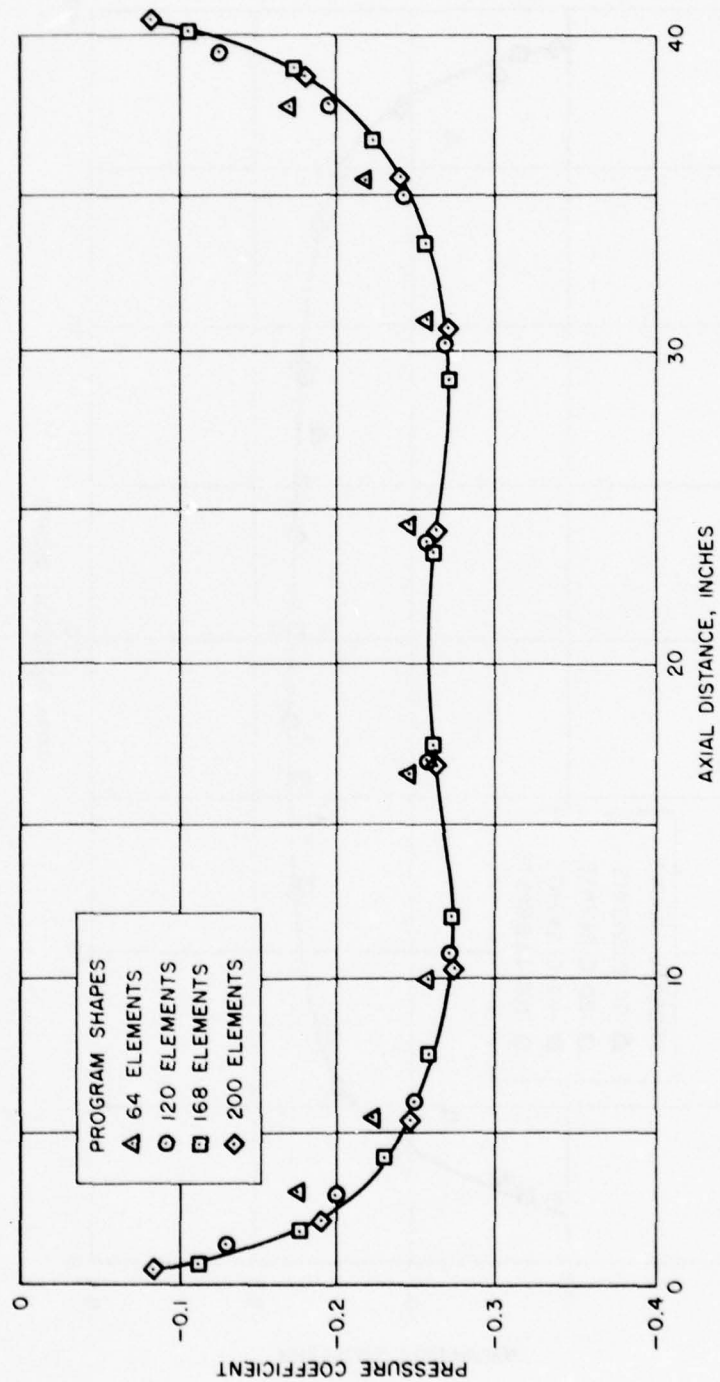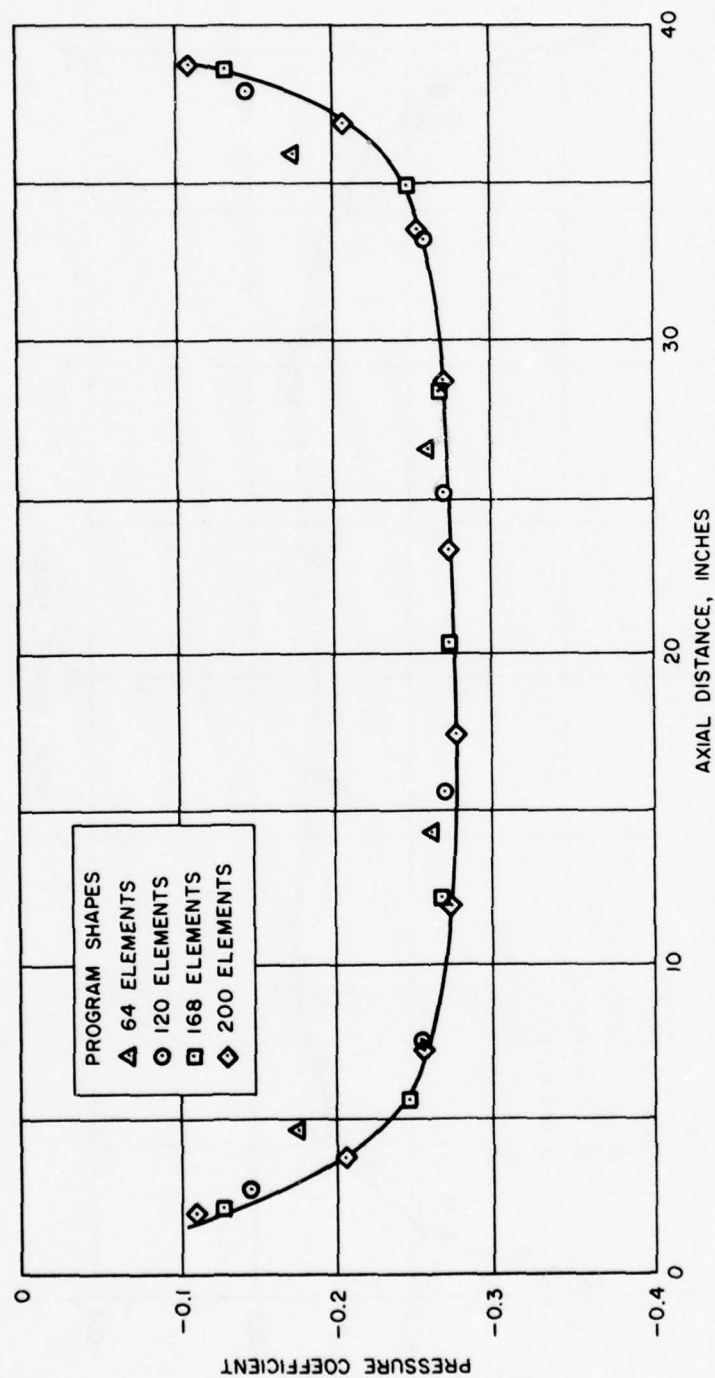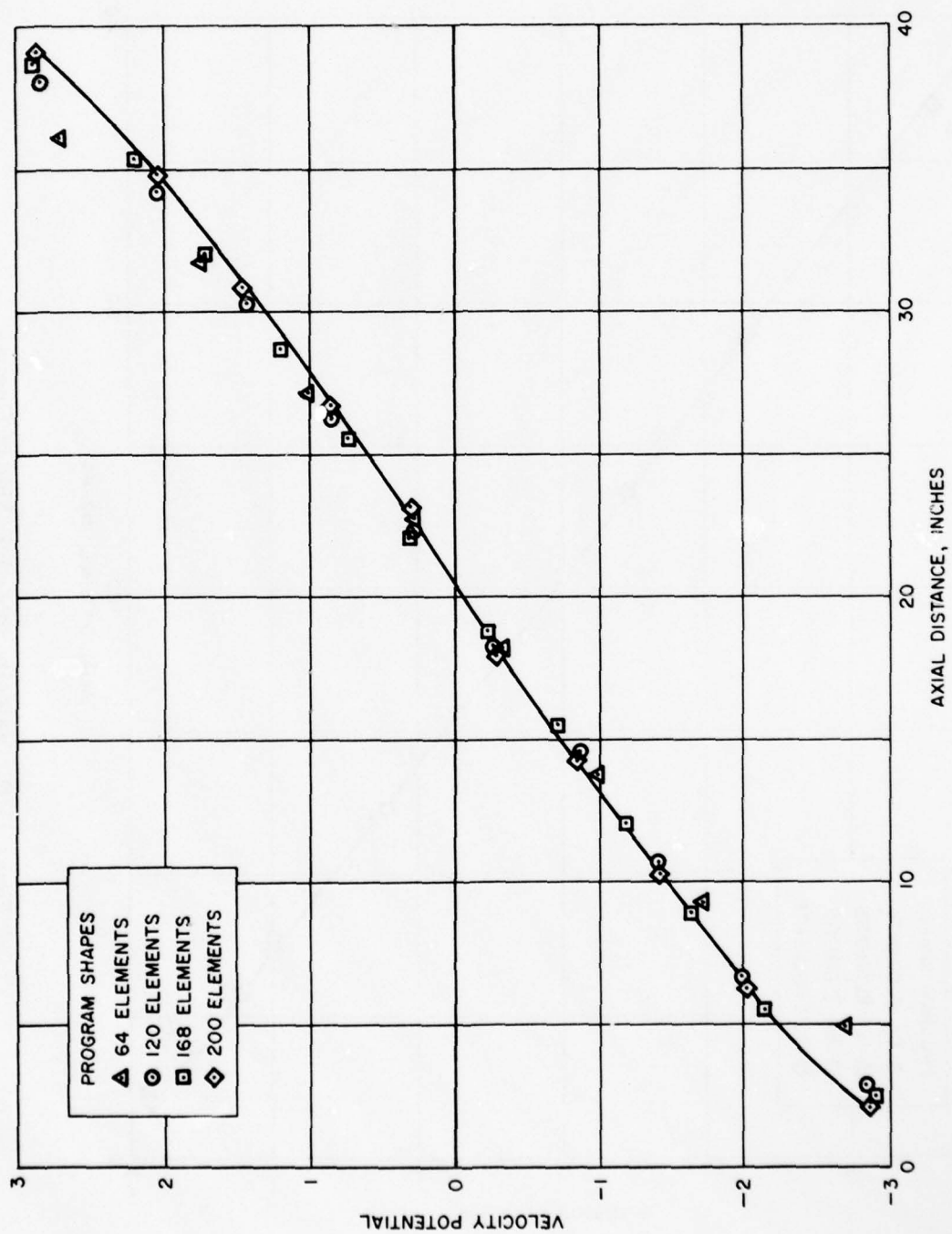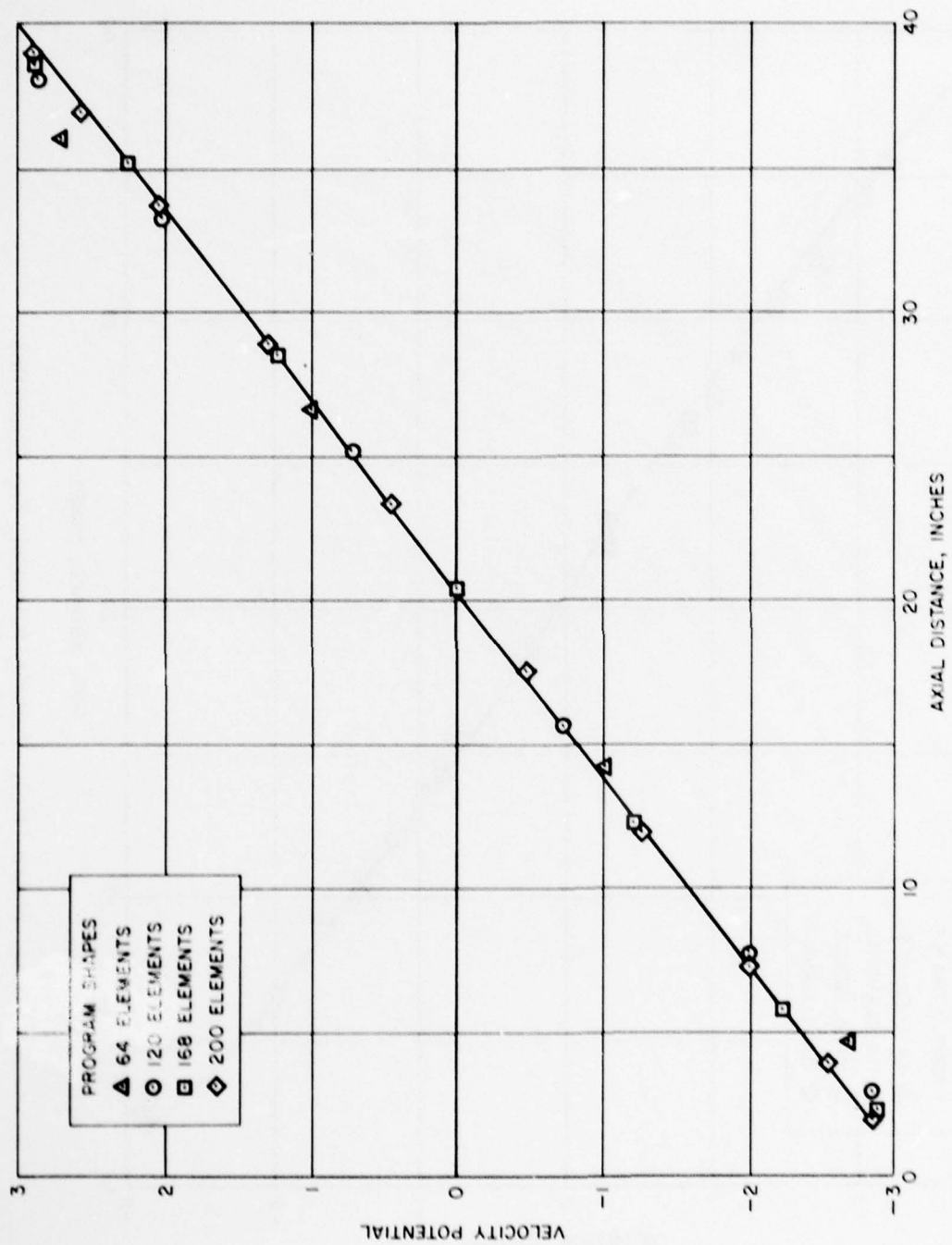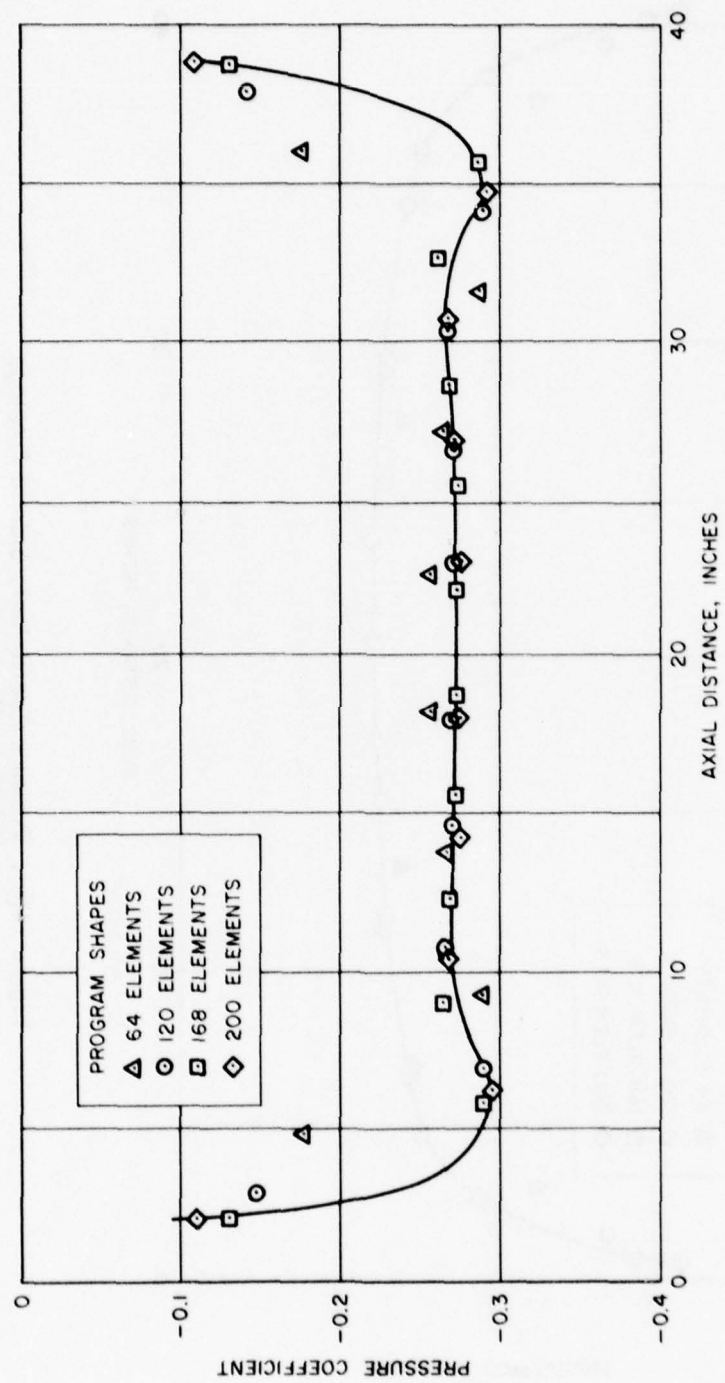Figure 11(f). Velocity Potential, Side of Fuselage (Uniform Elements).

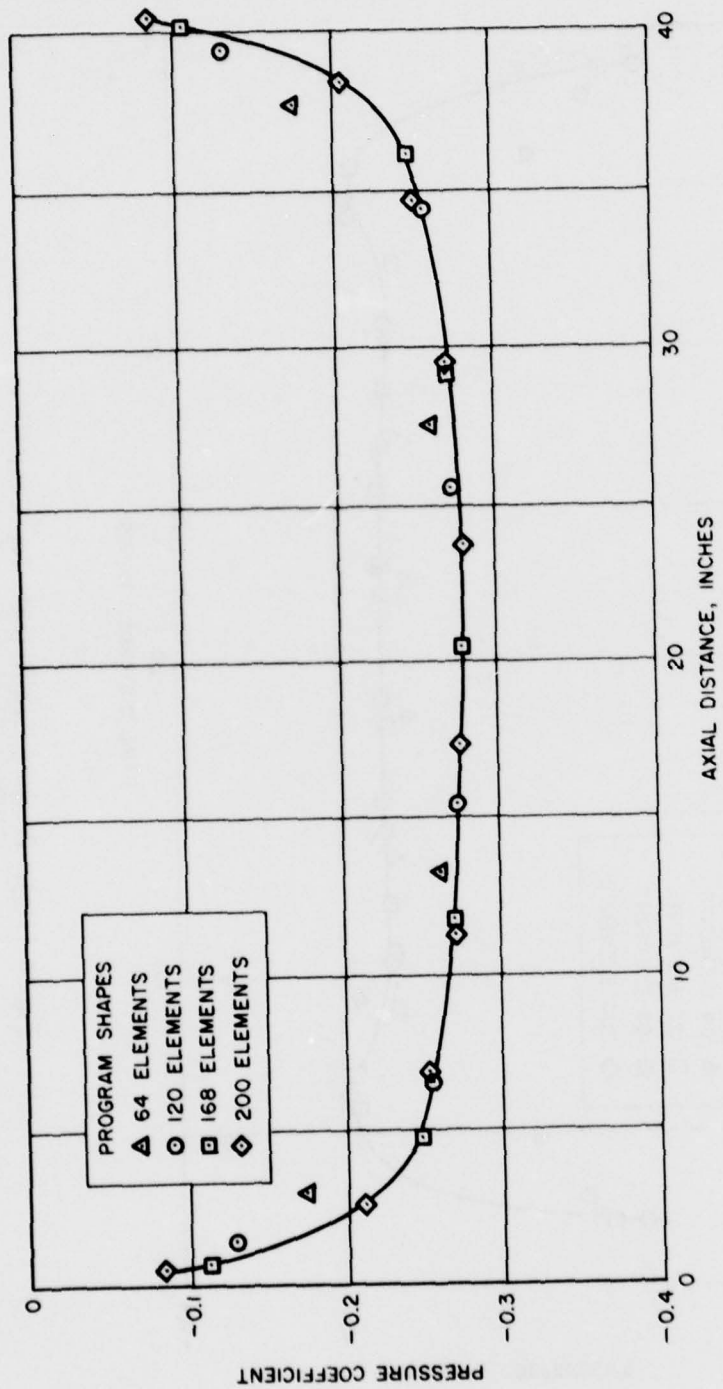Figure 11(g). Pressure Coefficient, Top Centerline (Uniform Elements).

69

Figure 11(h). Pressure Coefficient, Side of Fuselage
(Uniform Elements).

estimated that for this fuselage approximately 168 nonuniform elements are sufficient for convergence, whereas the use of the uniform element scheme requires more than 200 elements for analysis.

6.1.2   SEPARATION EFFECTS

The study of the effects of the separation wake on an ellipsoidal helicopter fuselage configuration is given in Figure 12. The location of the separation line is prescribed and can be determined from existing flow visualization data or estimated by the use of analytical criteria for separation.

The strength of the isolated vortex element is varied such that the velocity is zero at the prescribed separation location. Figure 12 shows the effect of the strength of an isolated vortex element on the potential difference distribution and pressure on the top centerline of a simple ellipsoidal fuselage at 150 mph, $\alpha = 0^{\circ}$, and $\beta = 0^{\circ}$. Again the overall dimensions of the fuselage are 41, 14.5, and 16.5 inches, respectively. The four cases run are shown below.

Run	Symbol	Vortex Strength
1	△	20
2	○	40
3	▢	60
4	◇	80

The number of aerodynamic elements used in each case is 186. On the CDC 6600 computer system, the required computer time was approximately 80 seconds per case, i.e., for each value of vortex strength. Again, the symmetry of the helicopter fuselage was not employed.
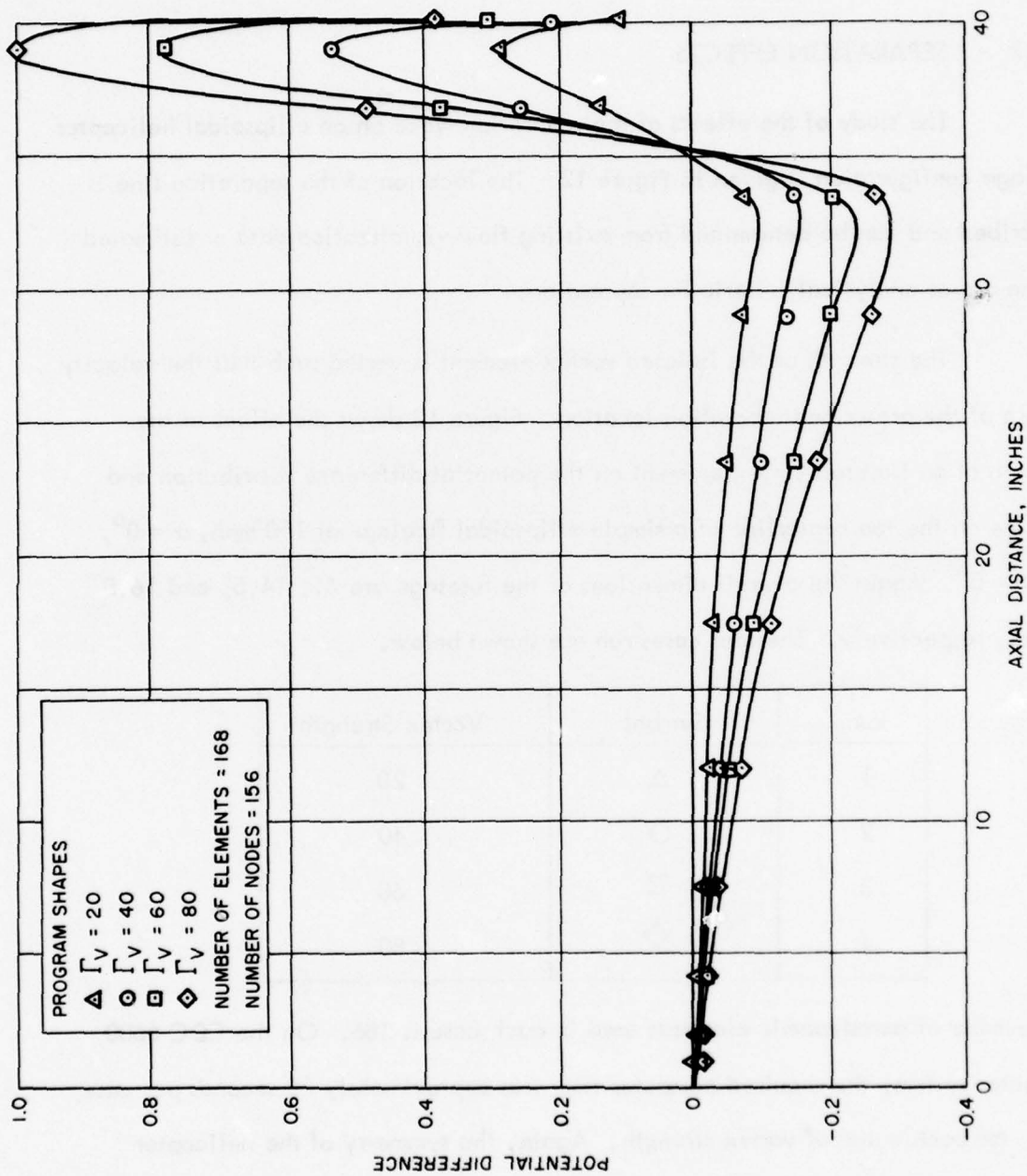
71

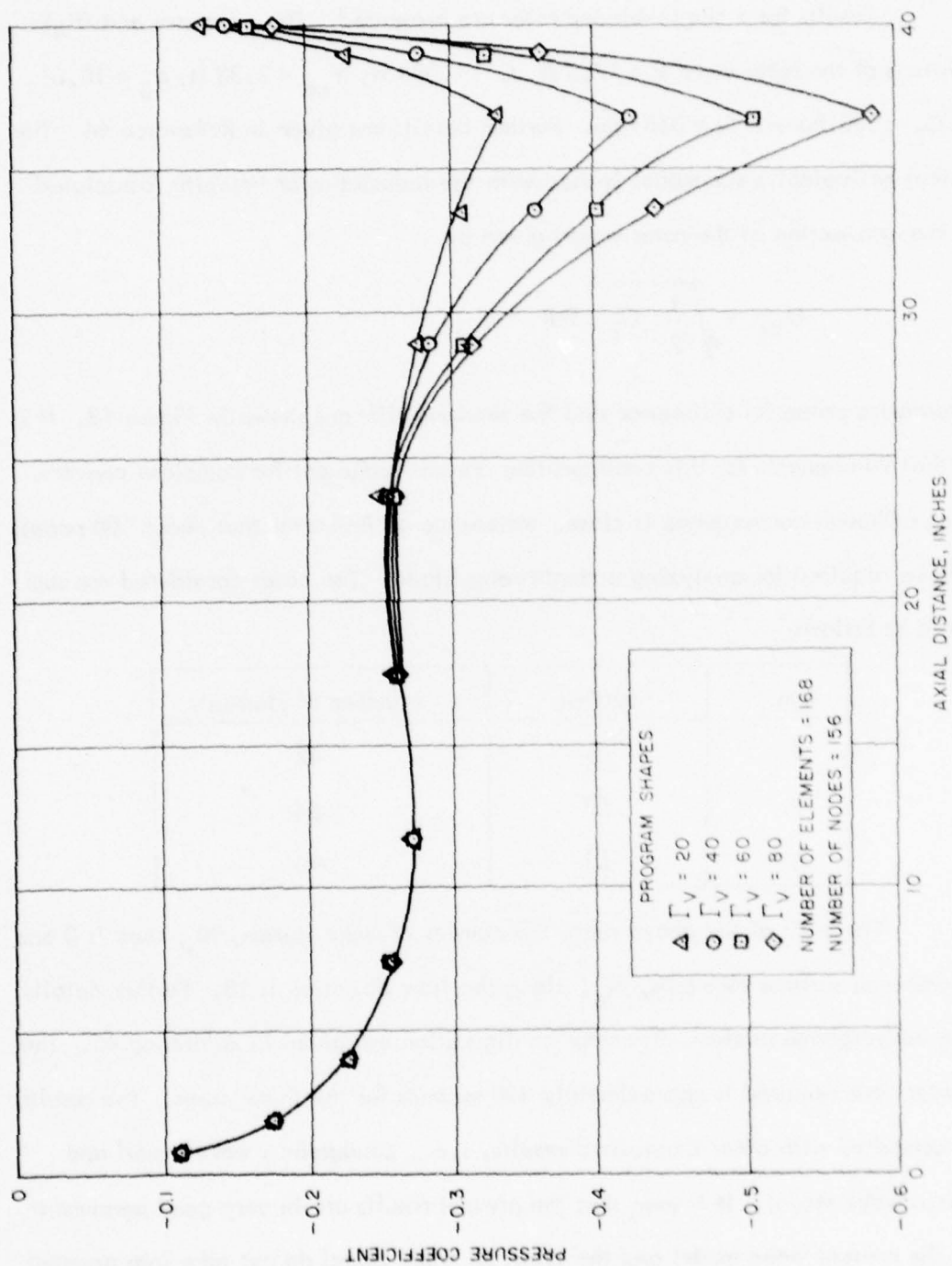Figure 12(a). Potential Difference, Top Centerline.

Figure 12(b). Pressure Coefficient, Top Centerline.

6.1.3   ROTOR EFFECTS

Results for a single-bladed rotor are presented. The geometry and flight conditions of the rotor were $R = 17.5$ ft, $C = 1.083$ ft, $Y_{co} = 2.33$ ft, $\alpha_B = 10.61$ with $C_T = .00186$ and $\Omega = 355$ rpm. Further details are given in Reference 44. The classical helicoidal wake model is used with the induced rotor velocity (associated with the convection of the rotor wake) given by

$$U_W = \sqrt{\frac{1}{2}\, C_T}\ \ \Omega R$$

The spanwise potential difference and the sectional lift are shown in Figure 13. It is seen that 90 elements for this configuration are not sufficient for complete convergence, although convergence is close. Reference 45 indicates that about 100 panels should be required for analyzing a single rotor blade. The cases considered are summarized as follows:

Run	Symbol	Number of Elements
1	◇	42
2	○	64
3	□	90

For each of the above runs, the number of wake spirals, N_s, used is 3 and the number of surface elements, N_e, along the flow direction is 18. Further details on the convergence analysis of a rotor configuration are given in Reference 45. The computer time required is approximately 400 seconds for the three cases. The results were compared with other theoretical results, i.e., Landgrebe's wake model and classical wake model. It is seen that the present results are in very good agreement since the present wake model and the classical wake model do not take into account
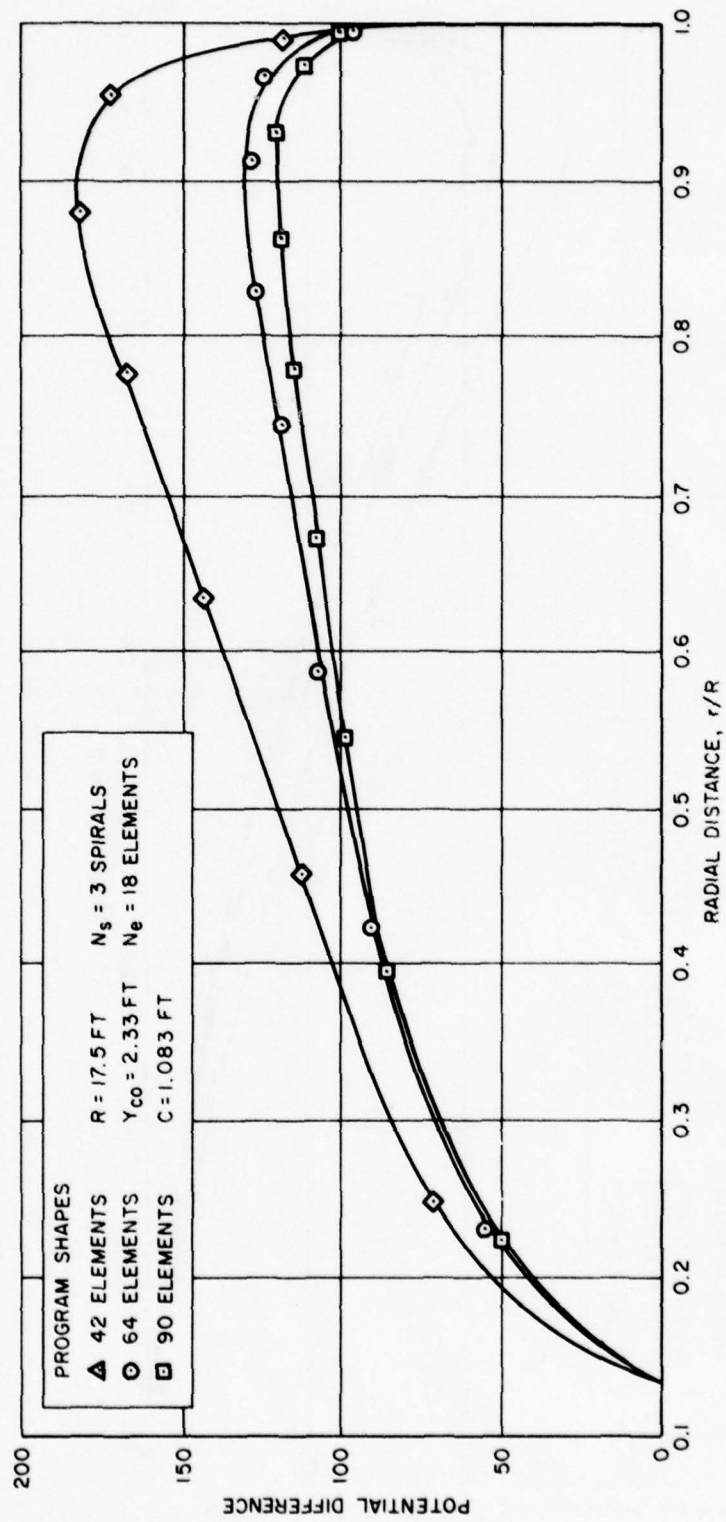
74

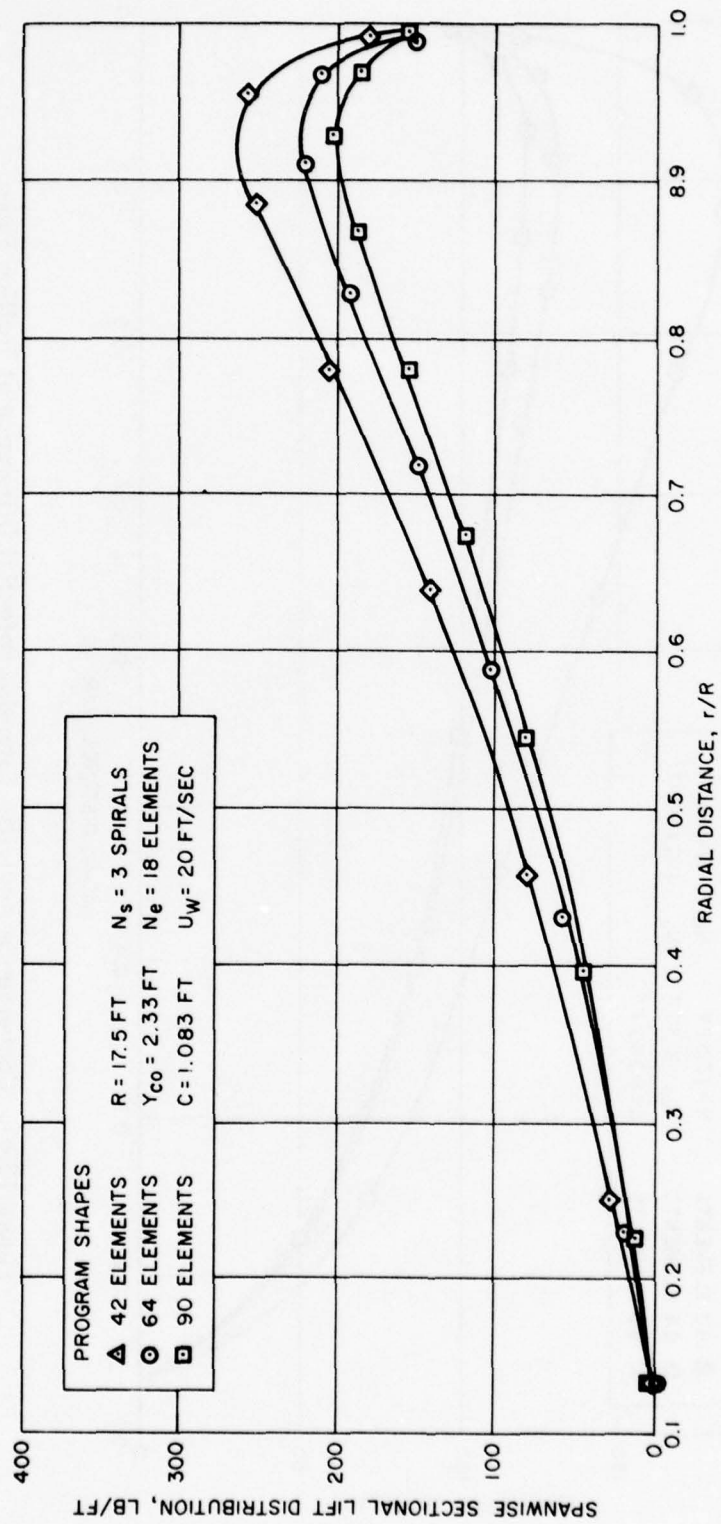Figure 13(a). Convergence Analysis: Spanwise Potential Difference at Trailing Edge.

75

Figure 13(b). Convergence Analysis: Spanwise Sectional Lift Distribution.
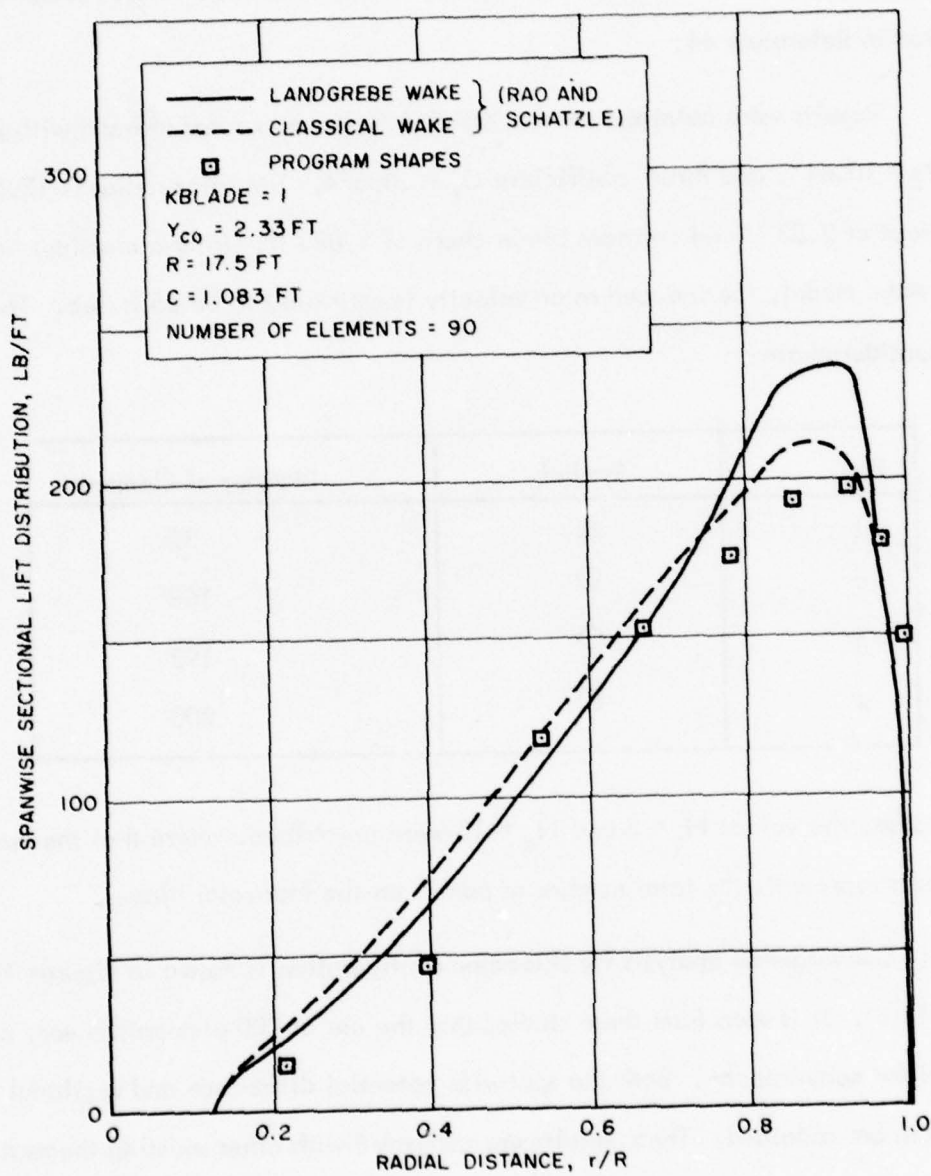
76

Figure 13(c). Comparison with Other Theoretical Results.

the concentration of the vortex sheet into a tip vortex (not included in the present analysis). It is noted that the Landgrebe wake model (Reference 46) is obtained from experiments and includes the effect of the tip vortex. Details of these results are presented in Reference 44.

Results were obtained for the XH-51A Helicopter rotor at hand with $\Omega = 355$ rpm, $\alpha_B = 10.61^\circ$, and thrust coefficient $C_T = .00574$. The rotor radius is 17.5 ft with root cutout at 2.33 ft and constant blade chord of 1.083 ft. Using a classical helicoidal wake model, the induced rotor velocity is estimated to be 35 ft/sec. The four cases considered are:

Run	Symbol	Number of Elements
1	△	32
2	○	168
3	◇	192
4	□	200

In each case, the values $N_s = 3$ and $N_e = 18$ were prescribed. Note that the number of elements represents the total number of panels on the four rotor blades.

Convergence analysis for this rotor configuration is shown in Figures 14(a) through 14(c). It is seen from these studies that the use of 200 elements is very nearly sufficient for convergence. Both the spanwise potential difference and sectional lift distribution are obtained. These results are compared with other existing theoretical and experimental results and are shown in Figure 14(c). Results are in excellent agreement with experimental data for the XH-51A obtained in Reference 47. Also, present results are in good agreement with results obtained using both the Landgrebe
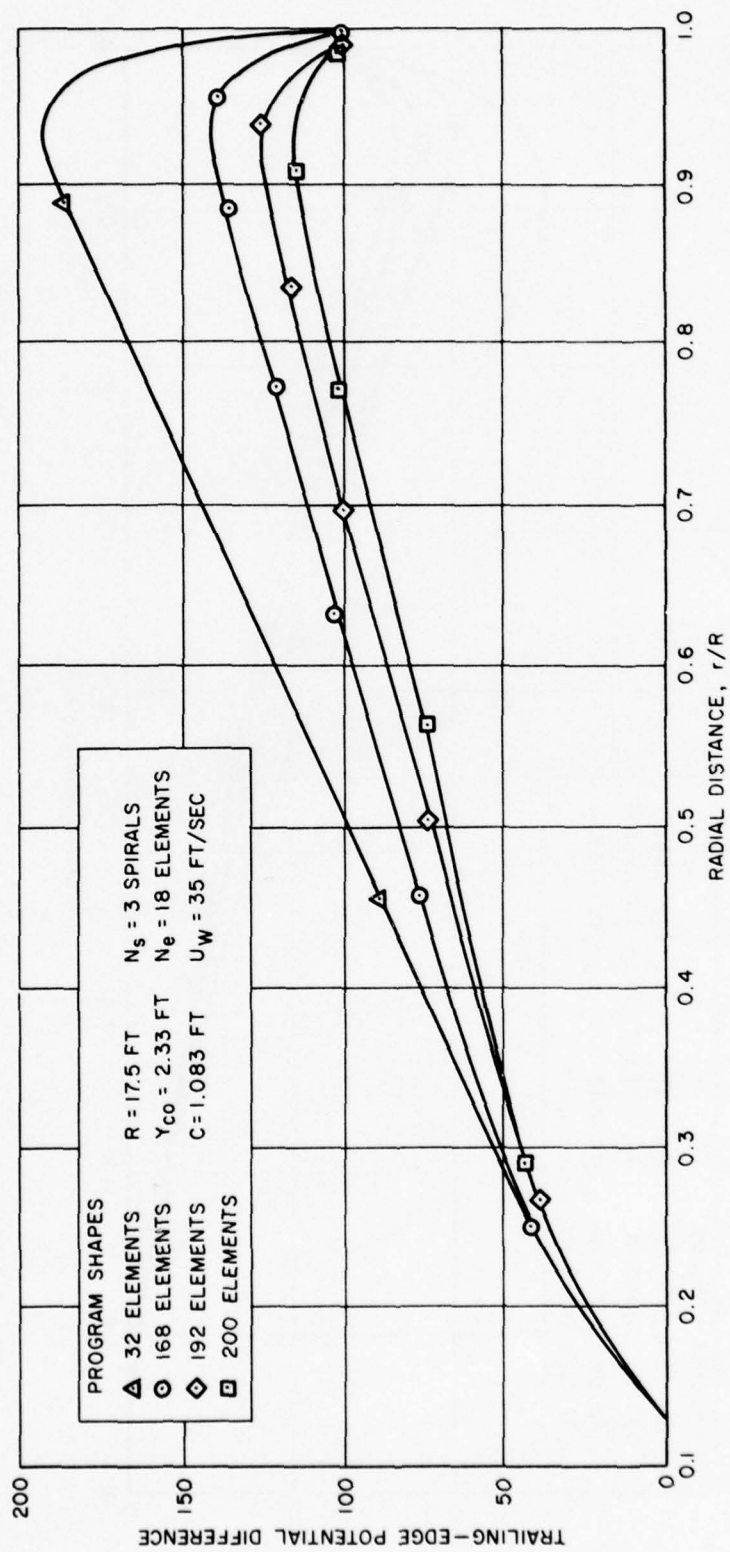
78

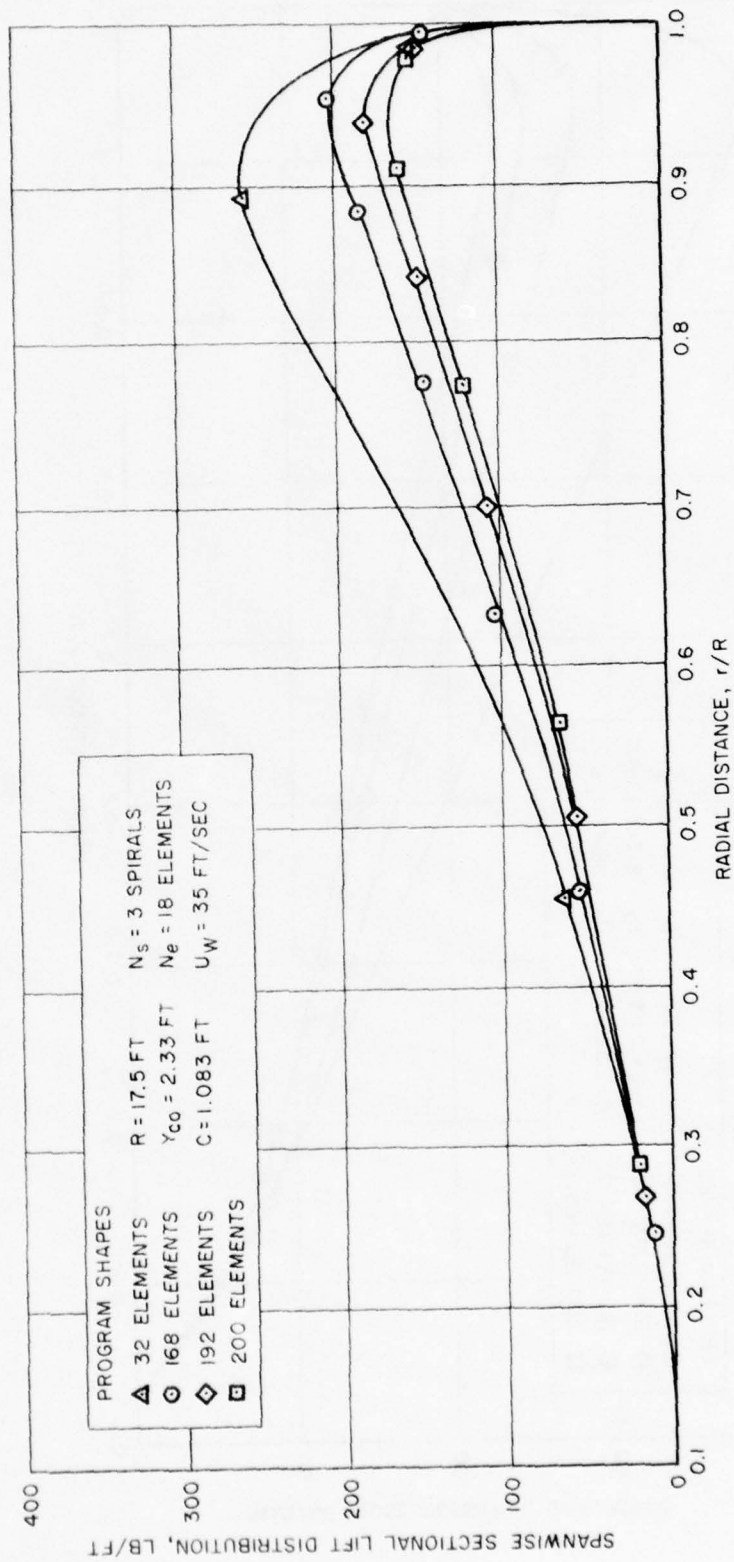Figure 14(a). Convergence Analysis: Spanwise Potential Difference at Trailing Edge.

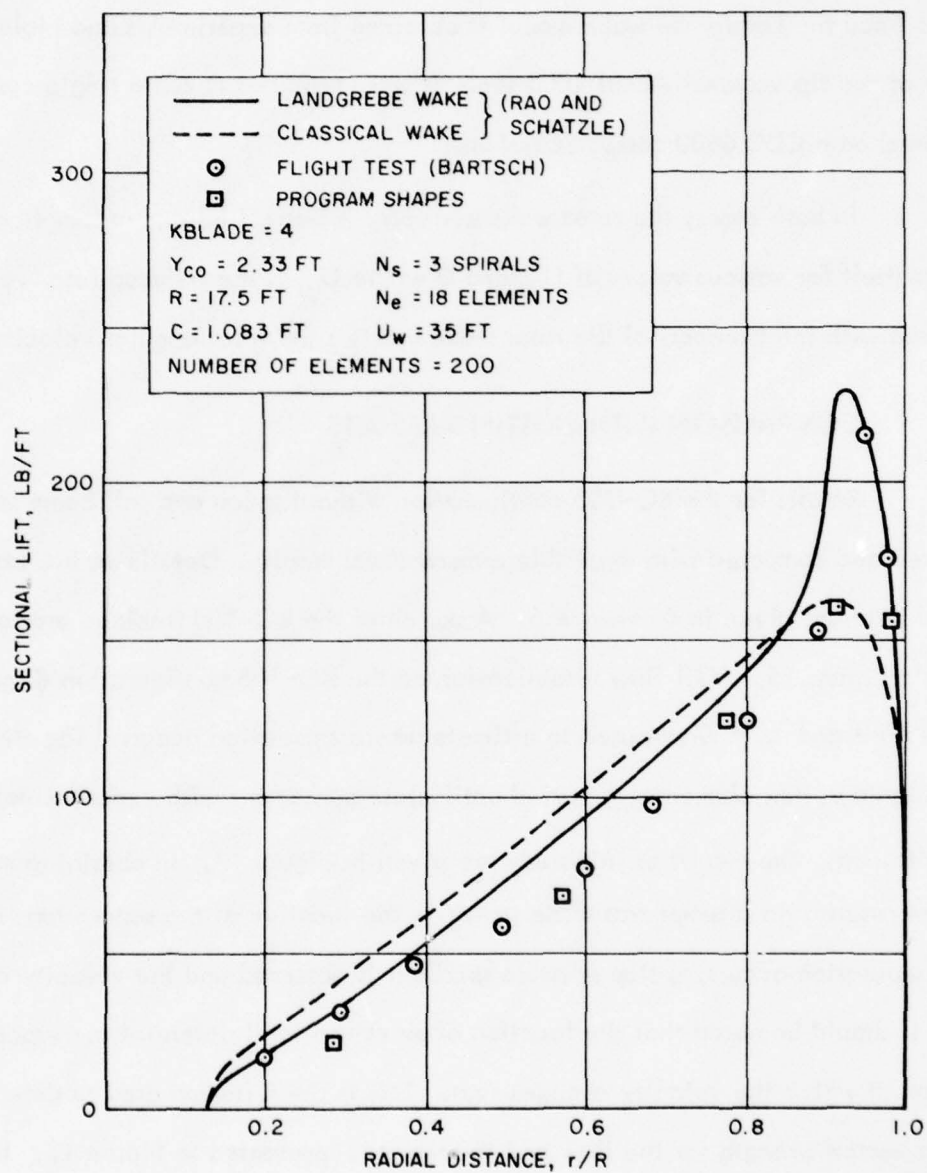Figure 14(b). Convergence Analysis: Spanwise Sectional Lift Distribution at Trailing Edge.

Figure 14(c). Comparison with Other Results.

wake model and classical wake model. Overall, the results are in exceptionally good agreement if one considers that the effect of the concentration of the vorticity into a tip vortex is not taken into account. This effect is clearly shown by Landgrebe wake results since the Landgrebe wake model is obtained from experiments and includes the effect of the tip vortex. About 1000 seconds were required to run a single case (200 elements) on a CDC 6600 computer system.

In both cases, the rotor wake geometry is helicoidal and automatically adjusts itself for various values of U_W and Ω where U_W is the induced rotor velocity involved with the transport of the rotor wake and Ω is the rotor angular velocity.

6.2 COMPARISON WITH EXISTING RESULTS

Results for the BO-105 configuration without pylon and tail boom section were obtained and compared with available experimental results. Details on the experimental data are given in Reference 5. A sketch of the BO-105 fuselage section is given in Figure 15. Oil flow visualization on the BO-105 configuration (Figure 16) at 150 MPH and $\alpha = 0$ was used to estimate where separation occurs. The strength of the isolated vortex element was varied until close agreement with experimental results was obtained. The results of this study are given in Figure 17. In obtaining most of these results, no attempt was made to verify the location of the separation line. When separation occurs, a step pressure gradient is observed and the velocity changes sign. It should be noted that the location of maximum total potential corresponds to the location at which the velocity changes sign. This is the criterion used to determine the correct vortex strength for the flow and the result is presented in Figure 17. In general, the results are good although some improvement is desirable. Improvement can be accomplished by moving the separation line, varying the vortex strength at smaller increments, and including a more complete vortex dynamic model.

82

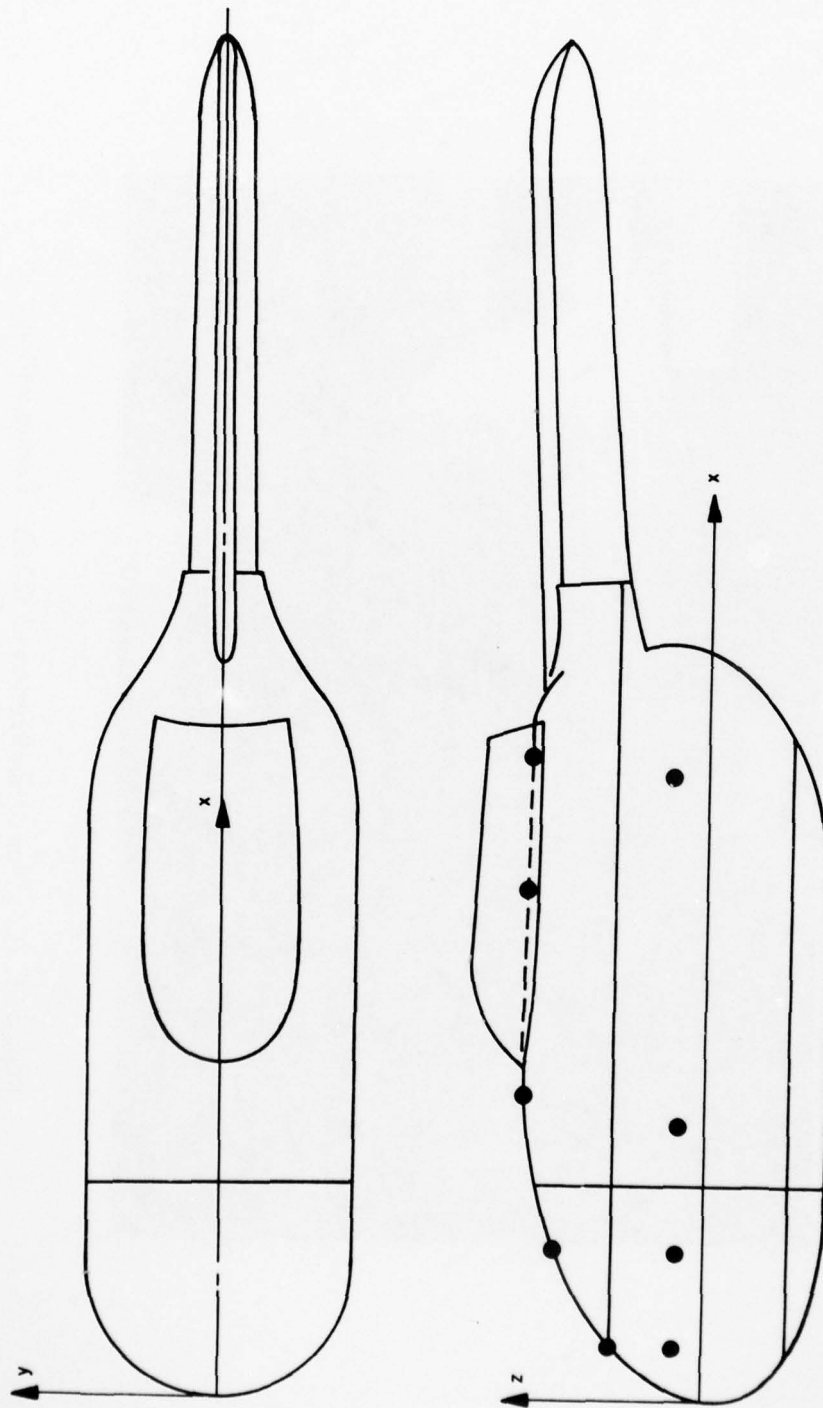● DENOTES LOCATION OF BOUNDARY LAYER PROBE

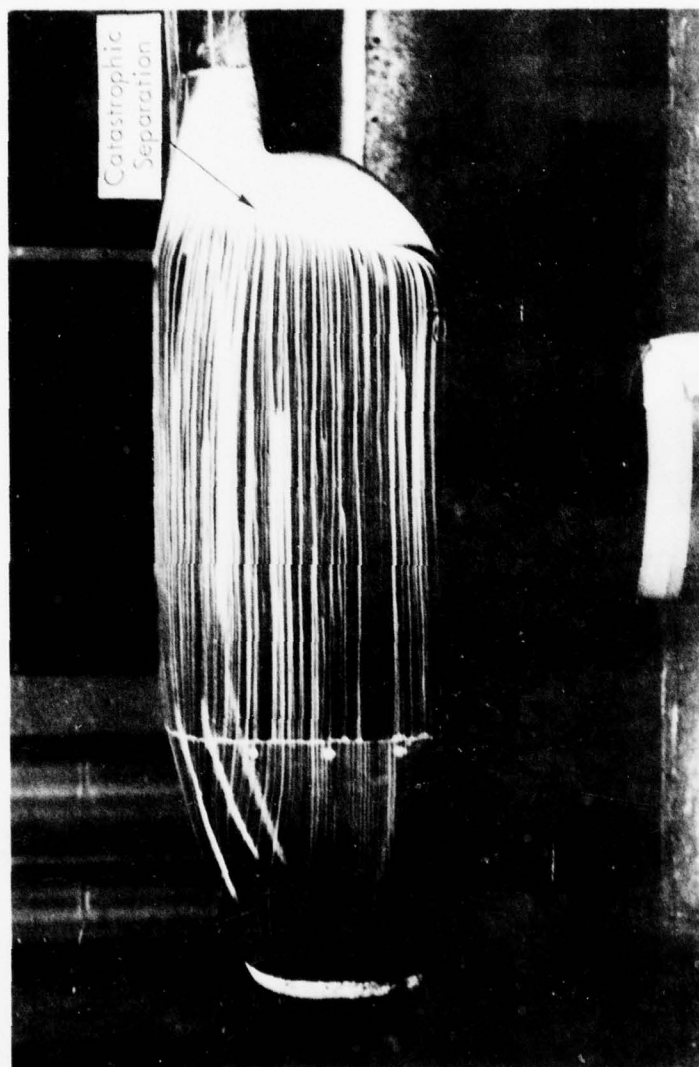Figure 15. Sketch of BO-105 Fuselage Section.

Catastrophic Separation

Figure 16. Oil Flow Visualization on BO-105 Configuration Without Pylon (Reference 5).
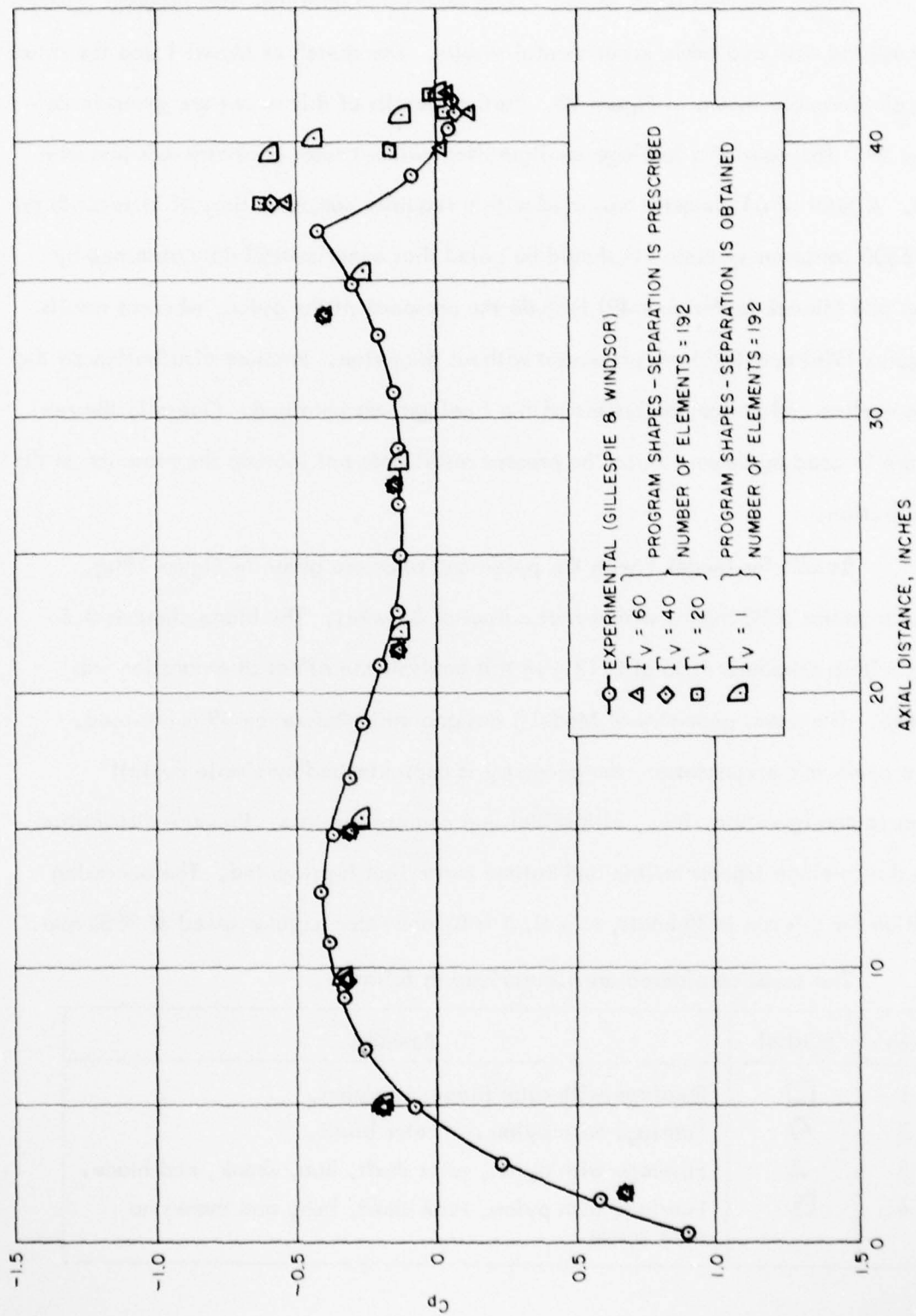
Figure 17. Pressure Coefficient, Top Centerline.

Next, the results for Model 1 with separation obtained from Program SHAPES are compared with available experimental results. The sketch of Model 1 and the rotor blade planform are shown in Figure 18. Further details of this model are given in Reference 49. The case of a fuselage configuration without rotor geometry was investigated. A total of 64 elements was used with a required computer time of 31 seconds on CDC 6600 computer systems. It should be noted that experimental data obtained by Wilson and Mineck (Reference 49) include the presence of the pylon, whereas results in Figures 19(a) and 19(b) are presented without the pylon. Pressure distribution on the top centerline and bottom centerline of the fuselage was obtained. Overall, the results are in good agreement since the present result does not include the presence of the pylon section.

Results for Model 1 with the pylon and rotor are given in Figure 19(c). The rotor radius is 20 inches with a root cutout of 8 inches. The blade chord is 3.5 inches with a thickness ratio of 0.12. In this analysis the effect of separation was included. The exact geometry of Model 1 designated in Reference 49 is not used. With a geometric preprocessor, the geometry is approximated by simple overall geometric configuration, i.e., ellipsoidal and conical sections. Pressure distribution along the fuselage top centerline and bottom centerline is presented. The operating condition for this run is 30 knots, $\alpha = 0$, $\beta = 0$, and rotor angular speed of 3600 rpm.

The cases considered are summarized as follows.

Run	Symbol	Remarks
1	□	Fuselage with rotor blade; no pylon.
2	◇	Fuselage with pylon and rotor blade.
3	△	Fuselage with pylon, rotor shaft, hub, shank, and blade.
4	◻	Fuselage with pylon, rotor shaft, hub, and shank; no rotor blade.

Figure 18(a). Geometry of Model 1.
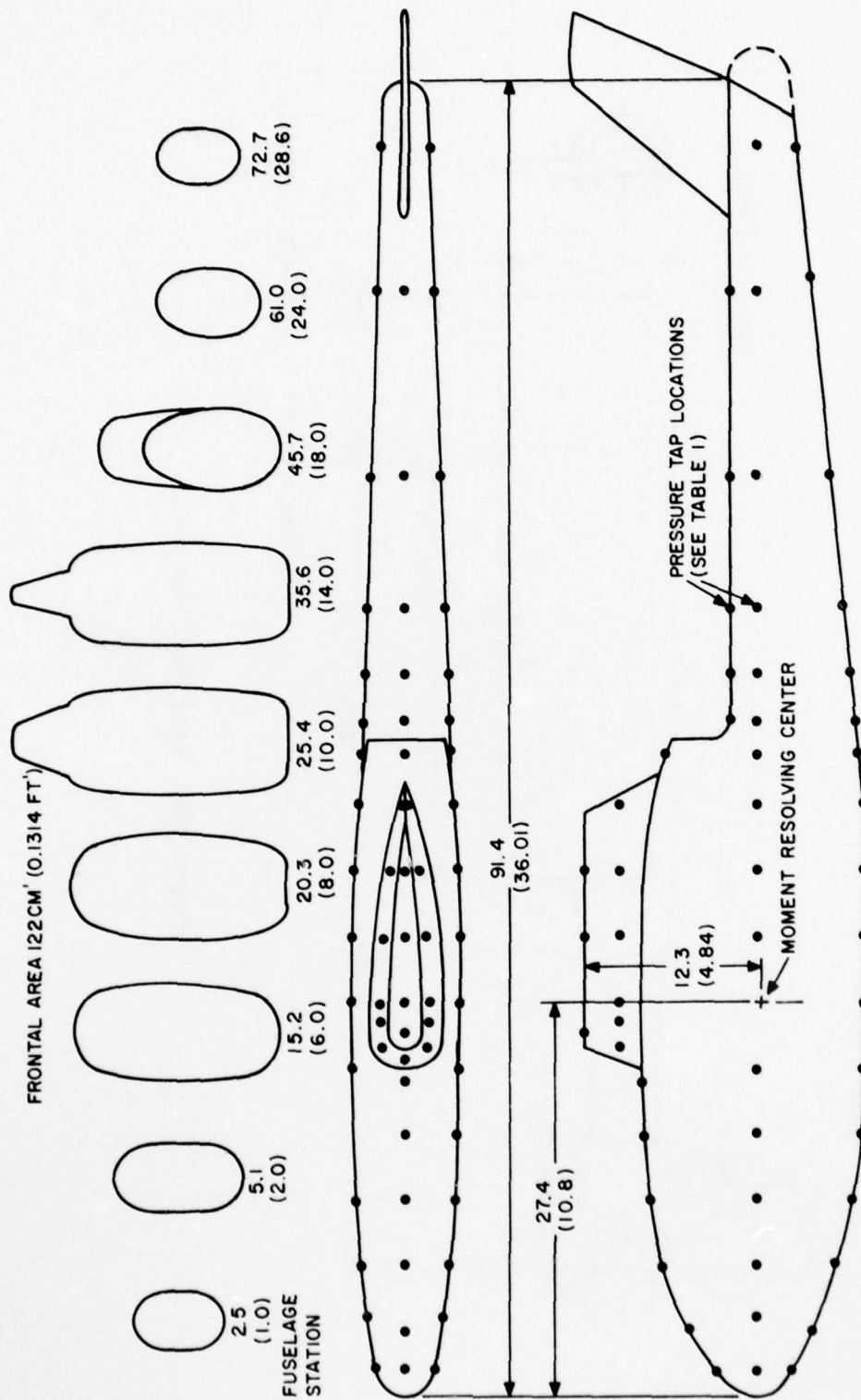
(All dimensions are in centimeters (inches) unless otherwise noted.)

87

NACA 0012 AIRFOIL

8.9
(3.5)

30.4
(12.0)

50.8
(20.0)

30°

FLAPPING AXIS
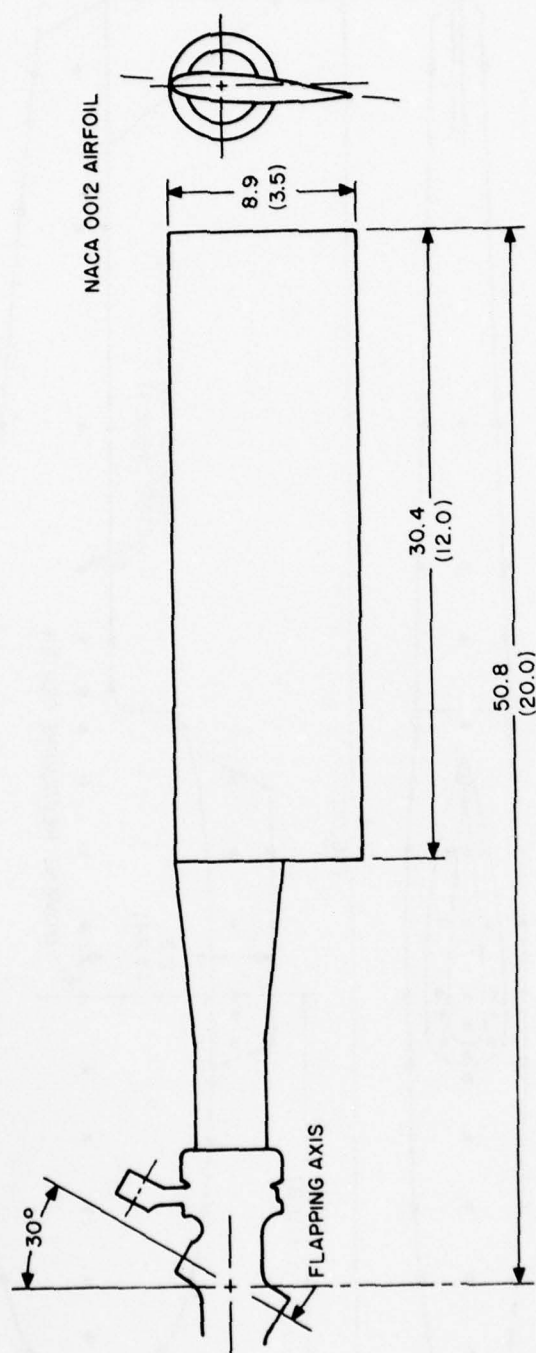
(Dimensions are in centimeters (inches).)

Figure 18(b). Rotor Blade Planform.
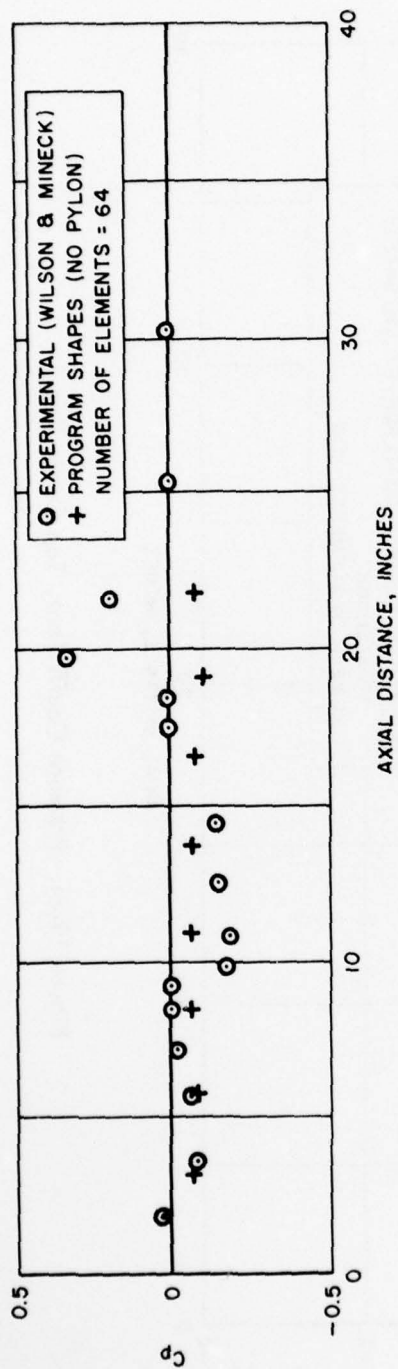
Figure 19(a). Pressure Coefficient, Top Centerline.
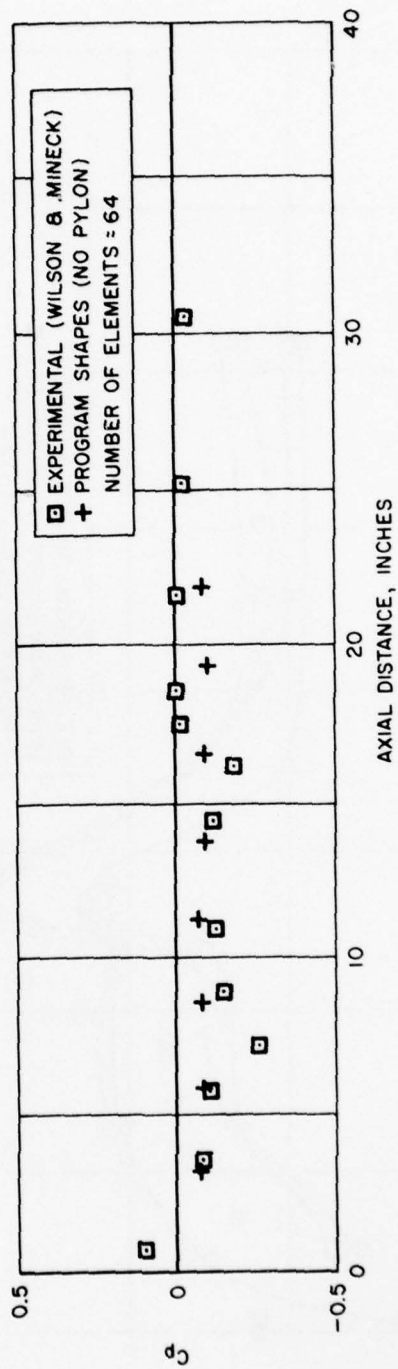
Figure 19(b). Pressure Coefficient, Bottom Centerline.

89
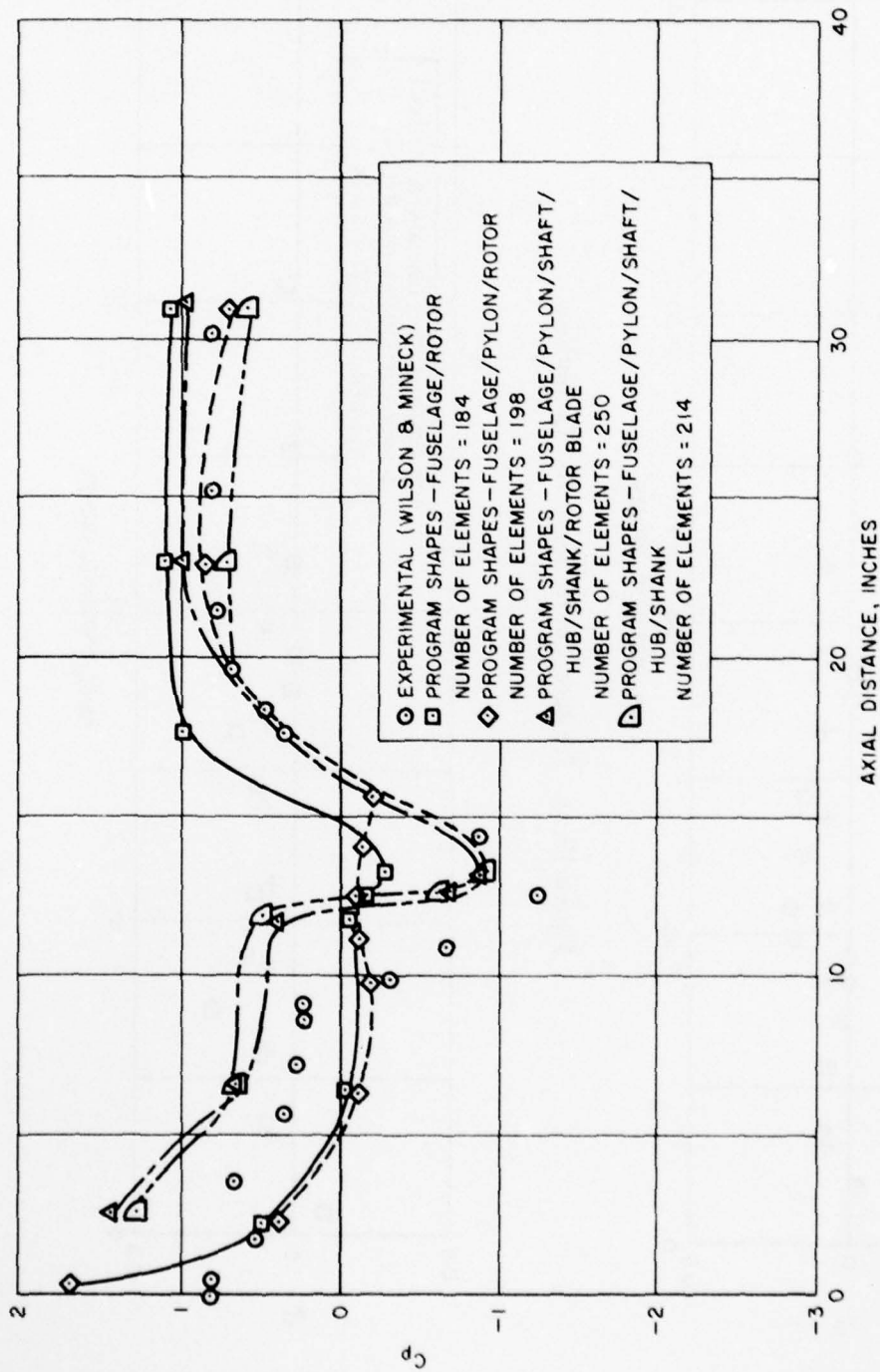
Figure 19(c). Pressure Coefficient, Top Centerline.

A typical computer time required for a case of Model 1 with rotor blade is approximately 600 seconds on the CDC 6600 computer system with 184 elements used. Again, the results obtained here compare very well with experimental data presented in Reference 49. It is seen that the effect of the pylon is small because the actual pylon geometry is replaced with a streamlined ellipsoidal pylon section. Hence, the pressure change on this fuselage/pylon section is smooth and not abrupt.

6.3 CONCLUDING REMARKS

The theoretical formulation and corresponding numerical procedure for the study of the total effect of the presence of the rotor in its various operating conditions on the pressure distribution and drag (induced) of the helicopter components beneath the rotor were presented. A potential flow aerodynamic program, SHAPES, with suitable rotor wake representation was developed to predict the separation characteristics of arbitrary three-dimensional helicopter configurations, with lifting surfaces in yawed flow. In particular, the effect of the rotor blade wake, blade shank wake, and hub wake on the separation of the flow over a lifting helicopter in forward flight was analyzed.

Specific capabilities of Program SHAPES include:

- Complete 3-D representation of fuselage/pylon/rotor/hub.

- Capability to input arbitrary aerodynamic paneling geometry.

- Preprocessor for simplified helicopter geometry to enhance parameter studies.

- Capability to run all or part of helicopter configuration.

- Capability to analyze separation effects on fuselage and pylon.

- Automatic generation of rotor and hub wake dynamics.

- Capability to run multibladed rotor problem.

91

The method is very flexible and simple to use; the use of quadrilateral hyperboloidal elements (which can be used to yield any arbitrary closed surface), defined in terms of their corner points, is one of the original features of the method. Other features of the method are the simplicity of the expression for the coefficients. This makes the method extremely efficient from a practical point of view. Also, the method is accurate and relatively fast, despite the fact that no effort has been made to minimize the computational time.

In contrast to existing methods, which in many instances require an extensive user's background in aerodynamics and familiarity with the specific method, the present code requires very limited human intervention and is extremely easy to use. It is emphasized that the only required inputs to the program are the locations of the corner points of the aerodynamic elements and certain specifications to the problem; i.e., Mach number, rotor angular speed, angle of attack, and the location of the separation line. In addition, the geometry of the wake is automatically generated. Present outputs available from the computer program include the aerodynamic coefficients, i.e., lift and induced drag, as well as the pressure and velocity flow field around the configuration.

It should be noted that the CPU time for the evaluation of the coefficient matrix is a large percentage (typically 80 to 90 percent) of the total CPU time. An improved computational scheme (Reference 50) has recently been developed. This scheme consists of combined numerical (Gaussian quadrature) and analytical procedures for the evaluation of the source and doublet integrals used in the program. The method employed in SOUSSA (Reference 50) is very accurate. However, the analytical evaluation of the coefficients (which is necessary for "near elements") requires an unnecessary amount of CPU time. A hybrid numerical–analytical scheme

for the evaluation of the coefficient is used. This scheme yields an appreciable re-duction of computer time (80 to 90 percent of the original time; i.e., after this modification, SOUSSA requires one-tenth of the original CPU time for the evaluation of the coefficients). Larger savings are expected for complex configurations, since in those cases a large number of elements is required simply to describe the geometry accurately. Hence, it is recommended that the optimal combination of the various schemes as well as the trade-off between accuracy and computer time be investigated.

Comparison with the results of References 44 and 46 - 49 indicates that the present results are in excellent agreement with existing ones and demonstrate the flexi-bility and usefulness of the program. A number of improvements are now under in-vestigation. It is seen that the present wake model does not take into account the concentration of the vortex sheet into a tip vortex. This tip vortex concentration has a strong effect on the flow field around the helicopter fuselage/rotor configuration. Also, a more complete separation representation can be incorporated. Improvement can be accomplished by moving the separation line and by varying the strength of the isolated vortex element to verify the area of separation. It is recommended that the aforementioned improvements be included in Program SHAPES.

The present method has potential application in the design of helicopter configurations because it provides an analytical capability to the engineer that is simple to apply and which can be used to develop a low-drag profile as well as to explore problem areas.

93

REFERENCES

1. Linville, J.C., AN EXPERIMENTAL INVESTIGATION OF THE EFFECTS OF ROTOR HEAD CONFIGURATION AND FUSELAGE YAW ON THE WAKE CHARACTERISTICS AND ROTOR PERFORMANCE OF A 1/8TH SCALE HELI-COPTER, Sikorsky Aircraft Division, United Aircraft Corporation; USAAVLABS Technical Report 69-94, U.S. Army Aviation Materiel Laboratories, Fort Eustis, VA, February 1970, AD 869390.

2. Linville, J.C., AN EXPERIMENTAL INVESTIGATION OF HIGH-SPEED ROTORCRAFT DRAG, Sikorsky Aircraft Division, United Aircraft Corporation; USAAMRDL Technical Report 71-46, Eustis Directorate, U.S. Army Air Mobility Research and Development Laboratory, Fort Eustis, VA, February 1972, AD 740771.

3. Gillespie, J., AN INVESTIGATION OF THE FLOW FIELD AND DRAG OF HELICOPTER FUSELAGE CONFIGURATIONS, Presented at the 29th Annual National Forum of the American Helicopter Society, Washington, DC, May 1973.

4. Julien, D., WIND TUNNEL TEST TO MEASURE SURFACE PRESSURE DISTRI-BUTIONS ON THE 1/12 SCALE HLH, Boeing Document D210-106771-1, Boeing Vertol Company, Philadelphia, PA, July 1973.

5. Gillespie, J., Jr., and Windsor, R.I., AN EXPERIMENTAL AND ANALYTI-CAL INVESTIGATION OF THE POTENTIAL FLOW FIELD, BOUNDARY LAYER, AND DRAG OF VARIOUS HELICOPTER FUSELAGE CONFIGURATIONS, USAAMRDL Technical Note 13, Eustis Directorate, U.S. Army Air Mobility Research and Development Laboratory, Fort Eustis, VA, January 1974, AD 777798.

6. Gillespie, J., Jr., STREAMLINE CALCULATIONS USING THE XYZ POTEN-TIAL FLOW PROGRAM, USAAMRDL Technical Note 16, Eustis Directorate, U.S. Army Air Mobility Research and Development Laboratory, Fort Eustis, VA, May 1974, AD 782955.

7. Woodward, F.S., Dvorak, F.S., and Geller, E.W., A COMPUTER PROGRAM FOR THREE-DIMENSIONAL LIFTING BODIES IN SUBSONIC INVISCID FLOW, Flow Research, Inc., USAAMRDL Technical Report 74-18, Eustis Directorate, U.S. Army Air Mobility Research and Development Laboratory, Fort Eustis, VA, April 1974, AD 782202.

8. Williams, R.M., and Montana, P.S., A COMPREHENSIVE PLAN FOR HELI-COPTER DRAG REDUCTION, Proceedings of the National Symposium on Helicopter Aerodynamic Efficiency, American Helicopter Society, Washington, DC, March 1975.

9. Keys, C., and Wiesner, R., GUIDELINES FOR REDUCING HELICOPTER PARASITE DRAG, Proceedings of the National Symposium on Helicopter Aerodynamic Efficiency, American Helicopter Society, Washington, DC, March 1975.

10. Sheehy, T.W., A SIMPLIFIED APPROACH TO GENERALIZED HELICOPTER CONFIGURATION MODELING AND THE PREDICTION OF FUSELAGE SURFACE PRESSURES, Proceedings of the National Symposium on Helicopter Aerodynamic Efficiency, American Helicopter Society, Washington, DC, March 1975.

11. Ashley, H., Widnall, S., and Landahl, M.T., NEW DIRECTIONS IN LIFTING SURFACE THEORY, AIAA Journal, Vol. 3, No. 1, January 1965, pp. 3-16.

12. Ashley, H., and Rodden, W.P., WING-BODY AERODYNAMIC INTERACTION, Annual Review of Fluid Mechanics, Vol. 4, 1972, pp. 431-472.

13. Hess, J.L., and Smith, A.M.O., CALCULATION OF NONLIFTING POTENTIAL FLOW ABOUT ARBITRARY THREE-DIMENSIONAL BODIES, Report No. ES 40622, Douglas Aircraft Company, Long Beach, CA, 1962.

14. Rubbert, P.E., and Saaris, G.R., REVIEW AND EVALUATION OF THREE-DIMENSIONAL LIFTING POTENTIAL FLOW ANALYSIS METHOD FOR ARBITRARY CONFIGURATIONS, AIAA Paper No. 72-188, January 1972.

15. Hess, J.L., CALCULATION OF POTENTIAL FLOW ABOUT ARBITRARY THREE-DIMENSIONAL LIFTING BODIES, Report No. MDC J5679-01, Douglas Aircraft Company, Long Beach, CA, 1972.

16. Labrujere, T.G., Loeve, W., and Sloof, J.W., AN APPROXIMATE METHOD FOR THE CALCULATION OF THE PRESSURE DISTRIBUTION OF WING-BODY COMBINATIONS AT SUBCRITICAL SPEEDS, AGARD Specialist Meeting on Aerodynamic Interference, Silver Spring, Maryland, September 1970, AGARD Conference Proceedings No. 71.

17. Woodward, F.A., ANALYSIS AND DESIGN OF WING-BODY COMBINATIONS AT SUBSONIC AND SUPERSONIC SPEEDS, Journal of Aircraft, Vol. 5, No. 6, November-December 1968, pp. 528-534.

18. Fox, C.H., Jr., and Breedlove, W.J., Jr., APPLICATION OF AN IMPROVED UNIFIED SUBSONIC-SUPERSONIC POTENTIAL FLOW METHOD FOR THE AERODYNAMIC ANALYSIS OF AIRCRAFT CONFIGURATIONS, AIAA Paper No. 74-186, January-February 1974.

19. Albano, E., and Rodden, W.P., A DOUBLET LATTICE METHOD FOR CALCULATING LIFT DISTRIBUTIONS ON OSCILLATING SURFACES IN SUBSONIC FLOWS, AIAA Journal, Vol. 7, No. 2, February 1969, pp. 279-285.
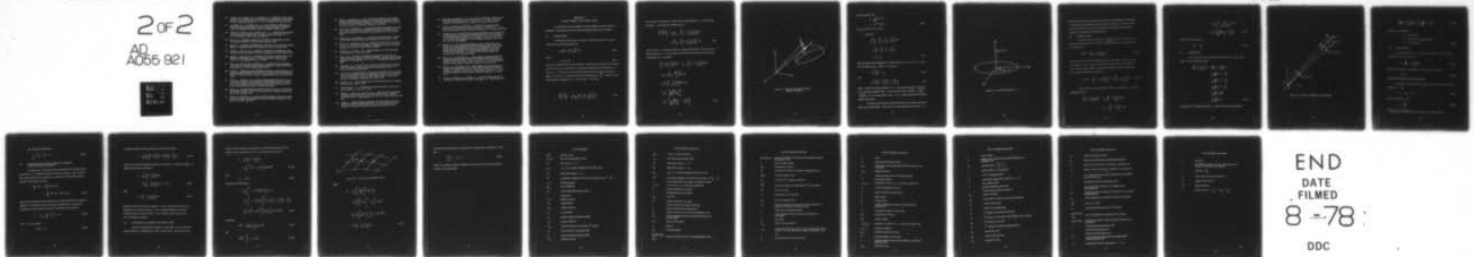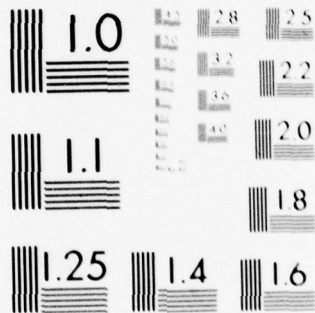
MICROCOPY RESOLUTION TEST CHART
NATIONAL BUREAU OF STANDARDS-1963-A

20. Giesing, J.P., Kalman, T.P., and Rodden, W.P., SUBSONIC STEADY AND OSCILLATORY AERODYNAMICS FOR MULTIPLE INTERFERING WINGS AND BODIES, Journal of Aircraft, Vol. 9, No. 10, October 1972, pp. 693-702.

21. Carmichael, R.L., and Woodward, F.A., AN INTEGRATED APPROACH TO THE ANALYSIS AND DESIGN OF WINGS AND WING-BODY COMBINATIONS IN SUPERSONIC FLOW, NASA TN D-3685, October 1966.

22. Baals, D.D., Robins, A.W., and Harris, R.V., Jr., AERODYNAMIC DESIGN INTEGRATION OF SUPERSONIC AIRCRAFT, Journal of Aircraft, Vol. 7, No. 7, September-October 1970, pp. 385-394.

23. Morino, L., A GENERAL THEORY OF UNSTEADY COMPRESSIBLE POTENTIAL AERODYNAMICS, NASA CR-2464, December 1974.

24. Morino, L., UNSTEADY COMPRESSIBLE POTENTIAL FLOW AROUND LIFTING BODIES - GENERAL THEORY, AIAA Paper No. 73-196, January 1973.

25. Morino, L., and Kuo, C.C., UNSTEADY SUBSONIC COMPRESSIBLE FLOW AROUND FINITE-THICKNESS WINGS, AIAA Paper No. 73-313, March 1973.

26. Morino, L., and Kuo, C.C., SUBSONIC POTENTIAL AERODYNAMICS FOR COMPLEX CONFIGURATIONS: A GENERAL THEORY, AIAA Journal, Vol. 12, No. 2, February 1974, pp. 191-197.

27. Chen, L.T., Suciu, E.O., and Morino, L., A FINITE ELEMENT METHOD FOR POTENTIAL AERODYNAMICS AROUND COMPLEX CONFIGURATIONS, AIAA Paper No. 74-107, January-February 1974.

28. Morino, L., SUBSONIC AND SUPERSONIC INDICIAL AERODYNAMICS AND AERODYNAMIC TRANSFER FUNCTION FOR COMPLEX CONFIGURATIONS, TN-74-01, Boston University, College of Engineering, Boston, MA, September 1974.

29. Morino, L., and Chen, L.T., INDICIAL COMPRESSIBLE POTENTIAL AERODYNAMICS AROUND COMPLEX AIRCRAFT CONFIGURATIONS, Presented at the NASA Conference on Aerodynamic Analysis Requiring Advanced Computers, Langley Research Center, VA, March 4-6,1975.

30. Morino, L., A FINITE ELEMENT METHOD FOR ROTATIONAL INCOMPRESSIBLE AERODYNAMICS, TN-74-04, Boston University, College of Engineering, Boston, MA, December 1974.

31. Tseng, K., and Morino, L., A NEW UNIFIED APPROACH FOR ANALYZING WING-BODY-TAIL CONFIGURATIONS WITH CONTROL SURFACES, AIAA Paper No. 76-418, July 1976.

32. Tseng, K., and Morino, L., FULLY UNSTEADY SUBSONIC AND SUPER-SONIC POTENTIAL AERODYNAMICS OF COMPLEX AIRCRAFT CONFIGU-RATIONS FOR FLUTTER APPLICATIONS, AIAA/ASME/SAE 17th Structures, Structural Dynamics, and Material Conference, May 1976.

33. Suciu, E.O., and Morino, L., A NONLINEAR FINITE-ELEMENT ANALYSIS OF WINGS IN STEADY INCOMPRESSIBLE FLOWS WITH WAKE ROLL-UP, AIAA 14th Aerospace Sciences Meeting, AIAA Paper No. 76-64, January 1976.

34. Heyson, H.H., and Katzoff, S., INDUCED VELOCITIES NEAR A LIFTING ROTOR WITH NONUNIFORM DISK LOADING, NACA TR-1319, 1957.

35. Marr, R.L., and Roderick, W.E.B., HANDLING QUALITIES EVALUATION OF THE XV-15 TILT ROTOR AIRCRAFT, Journal of the American Helicopter Society, Vol. 20, No. 2, April 1975, pp. 23-33.

36. Gessow, A., and Myers, G.C., AERODYNAMICS OF THE HELICOPTER, The Macmillan Co., New York, 1952.

37. Drees, J.M., A THEORY OF AIRFLOW THROUGH ROTORS AND ITS APPLICATION TO SOME HELICOPTER PROBLEMS, Journal of the Helicopter Association of Great Britain, Vol. 3, No. 2, July-September 1949, pp. 79-104.

38. Landgrebe, A.J., AN ANALYTICAL METHOD FOR PREDICTING ROTOR WAKE GEOMETRY, Journal of the American Helicopter Society, Vol. 14, No. 4, October 1969, pp. 20-32.

39. Scully, M.P., COMPUTATION OF HELICOPTER ROTOR WAKE GEOMETRY AND ITS INFLUENCE ON ROTOR HARMONIC AIRLOADS, MIT Aeroelastic and Structures Research Laboratory Report ASRL TR 178-1, Massachusetts Institute of Technology, Cambridge, MA, March 1975.

40. Batchelor, G.K., AN INTRODUCTION TO FLUID DYNAMICS, Cambridge University Press, 1970, p. 130.

41. Milne-Thomson, L.M., THEORETICAL HYDRODYNAMICS, Third Edition, The Macmillan Co., New York, 1957.

42. Morino, L., Chen, L.T., and Suciu, E.O., STEADY AND OSCILLATORY SUBSONIC AND SUPERSONIC AERODYNAMICS AROUND COMPLEX CONFIGURATIONS, AIAA Journal, Vol. 13, No. 3, March 1975, pp. 368-374.

43. Morino, L., FINITE-ELEMENT FORMULATION FOR SUBSONIC FLOWS AROUND COMPLEX CONFIGURATIONS, TR-73-05, Boston University, Department of Aerospace Engineering, Boston, MA, December 1973.

44. Rao, B.M., and Schatzle, P.R., ANALYSIS OF UNSTEADY AIRLOADS OF HELICOPTER ROTORS IN HOVER, AIAA Paper No. 77-159, AIAA 15th Aerospace Sciences Meeting, Los Angeles, CA, January 24-26, 1977.

45. Suciu, E., Preuss, R., and Morino, L., POTENTIAL AERODYNAMIC ANALYSES OF HORIZONTAL-AXIS WINDMILLS, AIAA Paper No. 77-132, AIAA 15th Aerospace Sciences Meeting, Los Angeles, CA, January 24-26, 1977.

46. Landgrebe, A.J., AN ANALYTICAL AND EXPERIMENTAL INVESTIGATION OF HELICOPTER ROTOR HOVER PERFORMANCE AND WAKE GEOMETRY CHARACTERISTICS, USAAMRDL Technical Report 71-24, Eustis Directorate, U.S. Army Air Mobility Research and Development Laboratory, Fort Eustis, VA, June 1971, AD 728835.

47. Bartsch, E.A., IN-FLIGHT MEASUREMENT AND CORRELATION WITH THEORY OF BLADE AIRLOADS AND RESPONSES ON THE XH-51A COMPOUND HELICOPTER ROTOR-VOLUME I: MEASUREMENT AND DATA REDUCTION OF AIRLOADS AND STRUCTURAL LOADS, USAAVLABS Technical Report 68-22A, U.S. Army Aviation Materiel Laboratories, Fort Eustis, VA, May 1968, AD 674193.

48. Wilson, J.C., and Mineck, R.E., WIND-TUNNEL INVESTIGATION OF HELICOPTER-ROTOR WAKE EFFECTS ON THREE HELICOPTER FUSELAGE MODELS, NASA TM X-3185, Langley Directorate, U.S. Army Air Mobility Research and Development Laboratory, Hampton, VA, March 1975.

49. Wilson, J.C., and Mineck, R.E., WIND-TUNNEL INVESTIGATION OF HELICOPTER-ROTOR WAKE EFFECTS ON THREE HELICOPTER FUSELAGE MODELS - Supplement, NASA TM X-3185, Langley Directorate, U.S. Army Air Mobility Research and Development Laboratory, Hampton, VA, March 1975.

50. Tseng, K., Puglise, J.A., and Morino, L., RECENT DEVELOPMENTS IN THE GREEN'S FUNCTION METHOD, AIAA Paper No. 77-456, March 1977.

APPENDIX A
SOURCE, DOUBLET, AND VORTEX LAYERS

In this appendix the main properties of source, doublet, and vortex layers are considered. The equivalence of vortex layers and doublet layers is also considered.

A.1 SOURCE LAYER

A distribution of sources over a surface Σ is called a source layer. The potential due to a source layer is given by

$$\varphi_S(\bar{P}_*) = \iint I_S \frac{-1}{4\pi r} \, d\Sigma \tag{A-1}$$

where

$$r = |\bar{P}_* - \bar{P}| \tag{A-2}$$

and I_S is the intensity of the source distribution. Note that a source layer does not yield any discontinuity on φ_S; therefore, the tangential components of the velocity are continuous on Σ. However, the normal component of the velocity due to a source layer, $\frac{\partial \varphi}{\partial n}$, is discontinuous. In order to determine the discontinuity of $\frac{\partial \varphi_S}{\partial n}$ consider the normal derivative of Equation (A-1) at a point $\bar{P}_o$ on Σ. This yields

$$\left(\frac{\partial \varphi_S}{\partial n} \right)_o = \lim_{\bar{P}_* \to \bar{P}_o} \iint I_S \frac{\partial}{\partial n_o} \left(\frac{-1}{4\pi r} \right) d\Sigma \tag{A-3}$$

99

Next consider on the surface Σ a small circular surface element, Σ_ϵ, with center $\bar{P}_o$ and radius ϵ. Then isolate the contribution of Σ_ϵ,

$$\left(\frac{\partial \varphi_S}{\partial n}\right)_o = \lim_{\bar{P}_* \to \bar{P}_o} \iint_{\Sigma - \Sigma_\epsilon} I_S \frac{\partial}{\partial n_o}\left(\frac{-1}{4\pi r}\right) d\Sigma$$

$$+ \lim_{\bar{P}_* \to \bar{P}_o} \iint_{\Sigma_\epsilon} I_S \frac{\partial}{\partial n_o}\left(\frac{-1}{4\pi r}\right) d\Sigma \qquad (A-4)$$

Note that when ϵ is sufficiently small, Σ_ϵ is approximately planar. Then considering a frame of reference X, Y, Z with origin at $\bar{P}_*$ and the Z-axis directed like the normal $\bar{n}$ (see Figure A-1), one obtains

$$\iint_{\Sigma_\epsilon} I_S \frac{\partial}{\partial n_o}\left(\frac{-1}{4\pi r}\right) d\Sigma = I_{S_o} \iint_{\Sigma_\epsilon} \bar{n}_o \cdot \nabla_*\left(\frac{-1}{4\pi r}\right) dX\, dY$$

$$= I_{S_o} 2\pi \int_0^\epsilon \bar{n}_o \cdot \frac{(\bar{P}_* - \bar{P})}{4\pi r^3} R\, dR$$

$$= I_{S_o} \frac{1}{2} \int_0^\epsilon \frac{Z_*}{(R^2 + Z_*^2)^{3/2}} R\, dR$$

$$= I_{S_o} \frac{1}{2} \left[\frac{-Z_*}{\sqrt{R^2 + Z_*^2}}\right]_0^\epsilon$$

$$= I_{S_o} \frac{1}{2} \left[\frac{-Z_*}{\sqrt{\epsilon^2 + Z_*^2}} + \frac{Z_*}{|Z_*|}\right] \qquad (A-5)$$

100
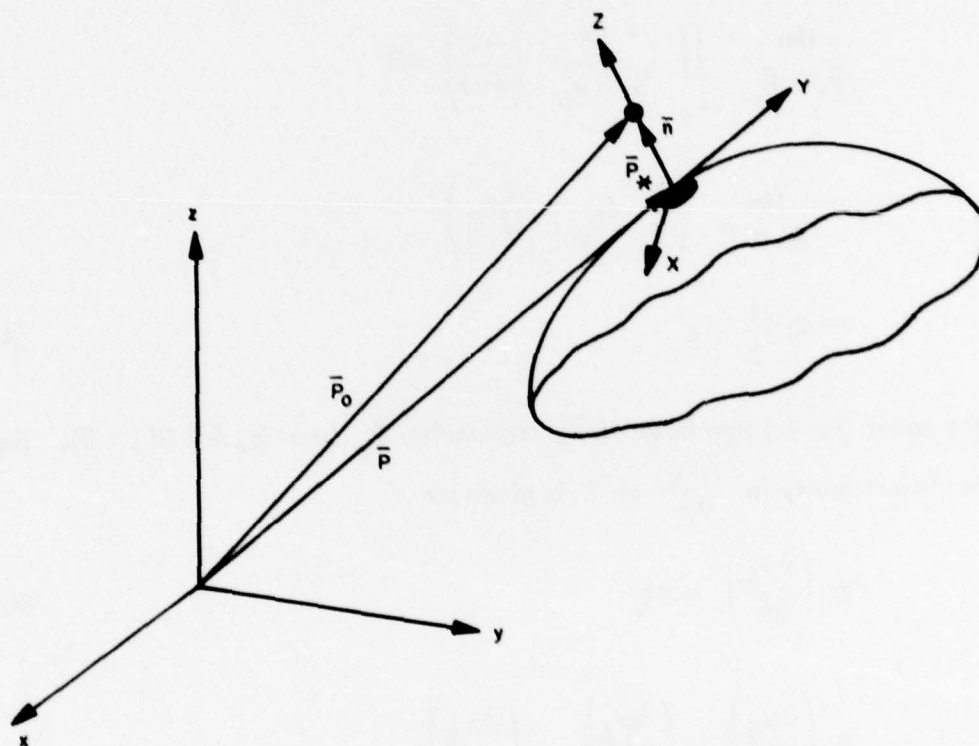
Figure A-1. Geometry for Layers of Sources,
Doublets and Vortices.

where (see Figure A-2)

$$R = \sqrt{X^2 + Y^2}$$

$$\theta = \tan^{-1} (Y/X) \tag{A-6}$$

and I_{S_o} is the value of I_S at $\bar{P}_o$.

Note that

$$\lim_{\bar{P}_* \to \bar{P}_o} \iint_{\Sigma_\epsilon} I_S \frac{\partial}{\partial n_o} \left(\frac{-1}{4\pi r} \right) d\Sigma$$

$$= \lim_{Z_* \to 0} \left(\frac{1}{2} I_{S_o} \frac{Z_*}{|Z_*|} \right)$$

$$= \pm \frac{1}{2} I_{S_o} \tag{A-7}$$

where the upper (lower) sign holds if $\bar{P}_*$ approaches $\bar{P}_o$ from $Z_* > 0$ ($Z_* < 0$). There-fore, the discontinuity in $\frac{\partial \varphi_S}{\partial n}$ on Σ is given by

$$\Delta \left(\frac{\partial \varphi_S}{\partial n} \right) = I_{S_o} \tag{A-8}$$

with

$$\Delta \left(\frac{\partial \varphi_S}{\partial n} \right) = \left(\frac{\partial \varphi_S}{\partial n} \right)_1 - \left(\frac{\partial \varphi_S}{\partial n} \right)_2 \tag{A-9}$$

where 1 indicates the side for positive Z, i.e., the side toward which $\bar{n}$ is pointing, and 2 indicates the opposite side. For a horizontal surface $\Delta \left(\frac{\partial \varphi_S}{\partial n} \right) = \left(\frac{\partial \varphi_S}{\partial n} \right)_u - \left(\frac{\partial \varphi_S}{\partial n} \right)_\ell$ if $\bar{n}$ is the upper normal, where u and ℓ indicate upper surface and lower surface, respectively.

The above result could be anticipated by thinking of a uniform source distri-bution on any infinite plane. The flux per unit area emanating from the layer is I_S.

102
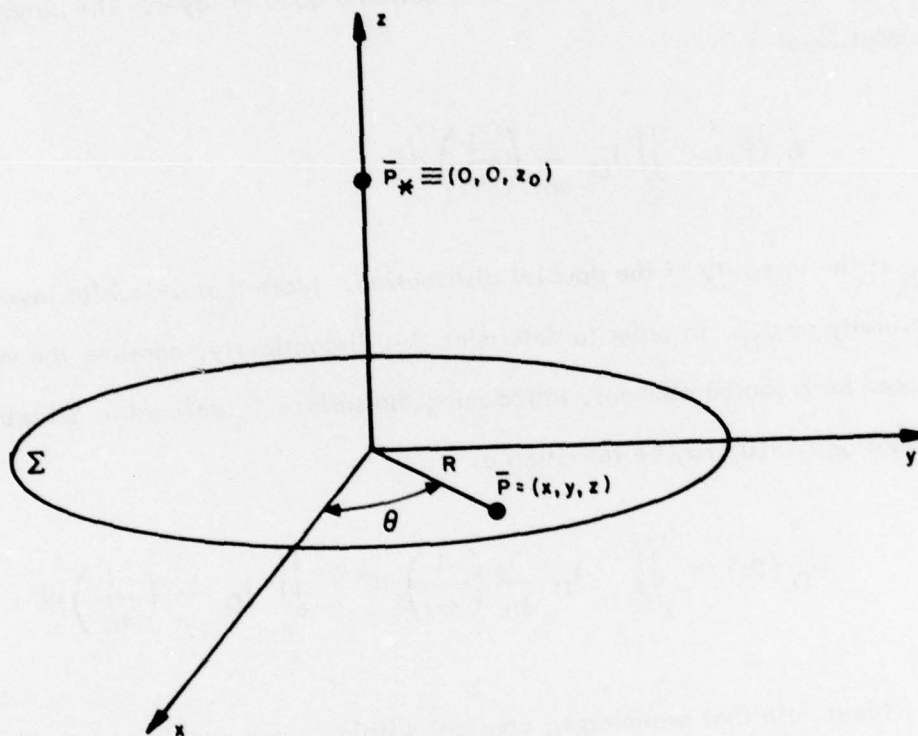
Figure A-2. Detailed Geometry for Σ_ϵ.

The flux (per unit area) on each side of the surface is $I_S/2$; therefore, the flow field is a uniform velocity of absolute value $I_S/2$ away from the layer. The value of $\partial\varphi/\partial n$ is $I_S/2$ on the side of $\bar{n}$ and $-I_S/2$ on the other side. Therefore, the discontinuity is equal to I_S (if evaluated in the direction of $\bar{n}$).

A.2   DOUBLET LAYERS

A surface distribution of doublets, $\dfrac{\partial}{\partial n}\left(\dfrac{-1}{4\pi r}\right)$, where $\bar{n}$ is the normal to the surface Σ (pointing from side 1 to side 2) is called a doublet layer. The potential due to a doublet layer is

$$\varphi_D(\bar{P}_*) = \iint_\Sigma I_D \frac{\partial}{\partial n}\left(\frac{-1}{4\pi r}\right) d\Sigma \qquad (A-10)$$

where I_D is the intensity of the doublet distribution. Note that a doublet layer yields a discontinuity on φ_D. In order to determine this discontinuity, consider the same process used for a source element. Introducing the surface Σ_ϵ defined in Subsection A.1, Equation (A-10) may be rewritten as

$$\varphi_D(\bar{P}_*) = \iint_{\Sigma-\Sigma_\epsilon} I_D \frac{\partial}{\partial n}\left(\frac{-1}{4\pi r}\right) d\Sigma + \iint_{\Sigma_\epsilon} I_D \frac{\partial}{\partial n}\left(\frac{-1}{4\pi r}\right) d\Sigma \qquad (A-11)$$

Next note that assuming I_D constant within Σ_ϵ and equal to I_{D_o}, one obtains (see Equation (A-5))

$$\iint_{\Sigma_\epsilon} I_D \frac{\partial}{\partial n}\left(\frac{-1}{4\pi r}\right) d\Sigma = I_{D_o} \iint_{\Sigma_\epsilon} \bar{n}\cdot\bar{\nabla}\left(\frac{-1}{4\pi r}\right) dX\,dY$$

$$= I_{D_o} \; 2\pi \int_0^\epsilon \bar{n}\cdot\frac{\bar{P}-\bar{P}_*}{4\pi r^3} R\,dR$$

104

$$= -I_{D_o} \frac{1}{2} \int_0^\epsilon \frac{Z_*}{(R^2 + Z_*^2)^{3/2}} R\,dR$$

$$= I_{D_o} \frac{1}{2} \left[\frac{Z_*}{\sqrt{\epsilon^2 + Z_*^2}} - \frac{Z_*}{|Z_*|} \right] \tag{A-12}$$

Therefore, the discontinuity is

$$\Delta \varphi_D = -I_{D_o} \tag{A-13}$$

A.3 SOLID ANGLES

It will be useful later to interpret doublet distributions in terms of solid angles. Note that (see Figure A-3)

$$\iint I_D \frac{\partial}{\partial n} \left(\frac{-1}{4\pi r} \right) d\Sigma = \iint I_D \, \bar{n} \cdot \frac{\bar{P} - \bar{P}_*}{4\pi r^3} \, d\Sigma$$

$$= \frac{1}{4\pi} \iint I_D \, \bar{n} \cdot \frac{\bar{r}}{r} \, \frac{d\Sigma}{r^2}$$

$$= \frac{1}{4\pi} \iint I_D \, \bar{n} \cdot \bar{e}_r \, \frac{d\Sigma}{r^2}$$

$$= \frac{1}{4\pi} \iint I_D \, \cos \chi \, \frac{d\Sigma}{r^2}$$

$$= \frac{1}{4\pi} \iint I_D \, \frac{d\Sigma n}{r^2}$$

$$= \frac{1}{4\pi} \iint I_D \, d\Omega \tag{A-14}$$

In particular, for a closed surface and I_D = constant, Equation (A-14) becomes

105
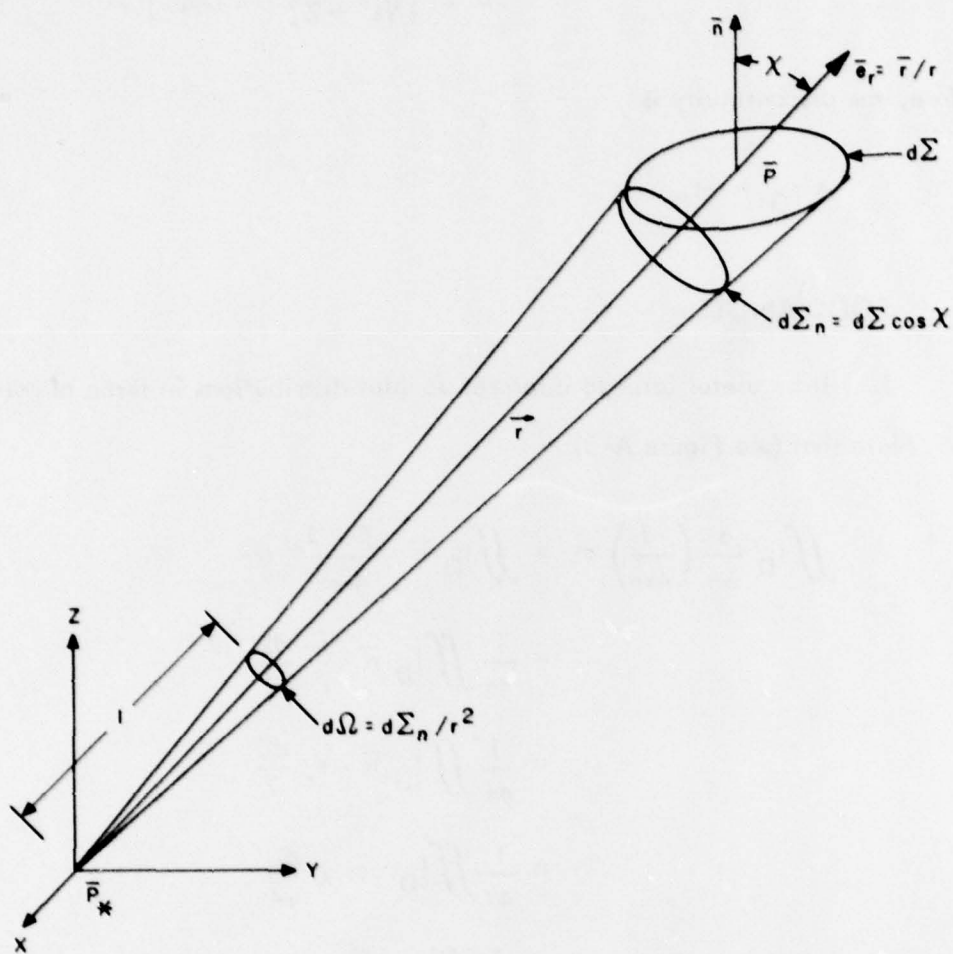
Figure A-3. Geometry for Definition of Solid Angles.

$$\oiint {}^{I}_{D} \frac{\partial}{\partial n}\left(\frac{-1}{4\pi r}\right) d\Sigma = \frac{{}^{I}_{D}}{4\pi} \oiint_{\Sigma} d\Omega = \frac{{}^{I}_{D}}{4\pi} \Omega \qquad (A-15)$$

Note that, as is well known

$$\Omega = 1 \qquad \text{for } \overline{P}_{\star} \text{ inside } \Sigma$$
$$= 1/2 \quad \text{for } \overline{P}_{\star} \text{ on } \Sigma \text{ (on regular point}^{\dagger})$$
$$= 0 \qquad \text{for } \overline{P}_{\star} \text{ outside } \Sigma \qquad (A-16)$$

A.4   VORTEX LAYERS

A surface distribution of vortices is called a vortex layer. The velocity created by a vortex layer is given by

$$\overline{v} = -\iint \overline{\gamma} \times \overline{\nabla}\left(\frac{-1}{4\pi r}\right) d\Sigma \qquad (A-17)$$

Note that the vorticity is represented by a solenoidal field. Therefore,

$$\gamma^{\alpha}/\alpha = 0 \qquad (A-18)$$

where the slash denotes covariant differentiation.

Introducing a curvilinear surface coordinate system ξ^{1}, ξ^{2}, such that the ξ^{1} is parallel to $\overline{\gamma}$, then

$$\overline{\gamma} = \gamma^{\alpha} \overline{a}_{\alpha} \equiv \gamma^{1} \overline{a}_{1} \qquad (A-19)$$

where $\overline{a}_{\alpha}$ are the base vectors

$$\overline{a}_{\alpha} = \frac{\partial \overline{P}}{\partial \xi^{\alpha}} \qquad (A-20)$$

---

† A regular point is defined here as a point where Σ has a tangent plane.

Thus, Equation (A-18) becomes

$$\frac{\partial}{\partial \xi^1} \left(\sqrt{a} \quad \gamma^1 \right) = 0 \tag{A-21}$$

A.5 EQUIVALENCE OF A SINGLE VORTEX TO A DOUBLET LAYER OF CONSTANT INTENSITY

In Subsection 3.6 the isolated vortex was represented as an isolated vortex branch wake, i.e., a doublet distribution with constant intensity. Here it is shown that a single closed vortex is equivalent to a doublet layer with constant intensity. The proof is based upon the identity

$$\oint_C \bar{f} \times d\bar{\ell} = - \iint_\Sigma (\bar{n} \times \bar{\nabla}) \times \bar{q} \, d\Sigma$$

$$= \iint_\Sigma [(\bar{\nabla} \cdot \bar{f}) \bar{n} - \bar{\nabla}(\bar{f} \cdot \bar{n})] \, d\Sigma \tag{A-22}$$

which may be obtained from the generalized Stokes' theorem (Reference 41, page 49, Equation 3). Consider the velocity induced by an isolated vortex on a point $\bar{P}*$. According to the well-known Biot and Savart law (Reference 41, page 521)

$$\bar{v}_\Gamma = - \frac{\Gamma}{4\pi} \oint_C \bar{\nabla} \left(\frac{-1}{r} \right) \times d\bar{\ell} \tag{A-23}$$

where Γ is the circulation

$$\Gamma = \oint \bar{v} \cdot d\bar{\ell} \tag{A-24}$$

108

According to Equation (A-22), Equation (A-23) may be rewritten as

$$\bar{v}_\Gamma = \frac{-\Gamma}{4\pi} \iint_\Sigma \left\{ \left[\bar{\nabla} \cdot \bar{\nabla} \left(\frac{1}{r} \right) \right] \bar{n} - \bar{\nabla} \left[\bar{\nabla} \left(\frac{1}{r} \right) \cdot \bar{n} \right] \right\} d\Sigma \qquad (A-25)$$

where Σ is any arbitrary surface bounded by the vortex line C. Noting that $\nabla^2 \left(\frac{1}{r} \right) = 0$, Equation (A-25) may be rewritten as

$$\bar{v}_\Gamma = \frac{\Gamma}{4\pi} \iint_\Sigma \bar{\nabla} \frac{\partial}{\partial n} \left(\frac{1}{r} \right) d\Sigma$$

$$= \bar{\nabla}_* \iint_\Sigma \Gamma \frac{\partial}{\partial n} \left(\frac{-1}{4\pi r} \right) d\Sigma = \bar{\nabla}_* \varphi_\Gamma \qquad (A-26)$$

when

$$\varphi_\Gamma = \iint_\Sigma \Gamma \frac{\partial}{\partial n} \left(\frac{-1}{4\pi r} \right) d\Sigma \qquad (A-27)$$

Equation (A-26) indicates that the velocity $\bar{v}_\Gamma$ due to a single closed vortex may be expressed in terms of the potential, φ_Γ, due to a doublet distribution of constant intensity equal to the vortex intensity Γ, over a surface Σ bounded by the vortex line C but otherwise arbitrary.

A.6   EQUIVALENCE OF DOUBLET AND VORTEX LAYERS

The above analysis may be extended to a vortex layer, since a vortex layer may be thought of as a superposition of single, closed vortices. The extension of the

analysis is briefly presented in the following. Note that (see Figure A-4) using Equation (A-22), the velocity $\bar{v}_\gamma$ due to a vortex layer may be written as

$$\bar{v}_\gamma = \frac{-1}{4\pi} \iint \bar{\gamma} \times \bar{\nabla} \left(\frac{1}{r}\right) d\Sigma$$

$$= \frac{-1}{4\pi} \int_0^{\Xi^2} \oint \gamma^1 \bar{a}_1 \times \bar{\nabla} \left(\frac{1}{r}\right) \sqrt{a} d\xi^1 d\xi^2 \qquad (A-28)$$

now if

$$d\bar{\ell} = d\xi^1 \bar{a}_1 \qquad (A-29)$$

then Equation (A-28) becomes

$$\bar{v}_\gamma = \frac{-1}{4\pi} \int_0^{\Xi^2} \sqrt{a} \; \gamma^1 d\xi^2 \oint \bar{\nabla} \left(\frac{1}{r}\right) \times d\bar{\ell}$$

$$= \frac{1}{4\pi} \int_0^{\Xi^2} \sqrt{a} \; \gamma_1 d\xi^2 \oint \int_0^{\xi^2} \left\{ \bar{\nabla} \cdot \bar{\nabla} \left(\frac{1}{r}\right) \bar{n} - \bar{\nabla} \left[\bar{\nabla} \left(\frac{1}{r}\right) \cdot \bar{n} \right] \right\} d\Sigma$$

$$= \frac{1}{4\pi} \bar{\nabla}_0 \int_0^{\Xi^2} \sqrt{a} \; \gamma_1 d\xi^2 \int_0^{\xi^2} \oint \frac{\partial}{\partial n} \left(\frac{1}{r}\right) \sqrt{a} \; d\xi^1 d\xi^2 \qquad (A-30)$$

Introducing

$$f(\xi^2) = \frac{-1}{4\pi} \oint \frac{\partial}{\partial n} \left(\frac{1}{r}\right) \sqrt{a} \; d\xi^1 \qquad (A-31)$$

and

$$D(\xi^2) = \int_{\Xi^2}^{\xi^2} \sqrt{a} \; \gamma^1 d\xi^2 \qquad (A-32)$$

110
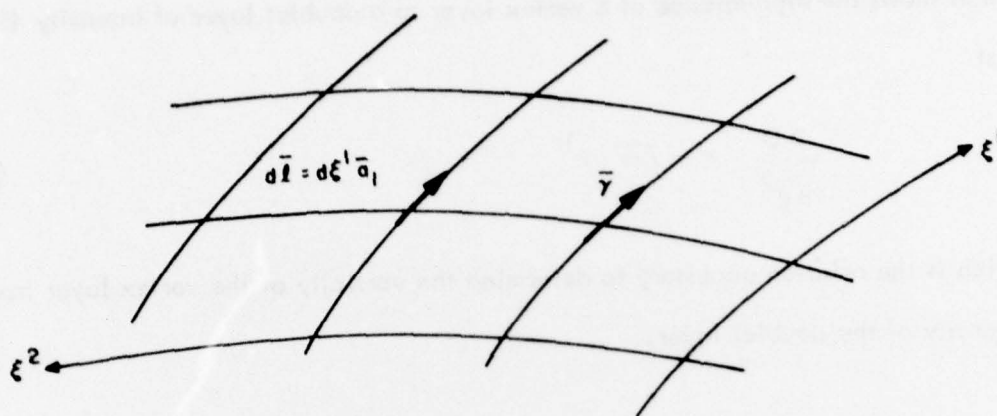
Figure A-4. Vortex Layers and Doublet Layers.

yields

$$\overline{I}_v = -\overline{v}_0 \int_0^{\Xi^2} \frac{\partial D}{\partial \xi^2} \left[\int_0^{\xi^2} f \, d\varsigma^2 \right] d\xi^2$$

$$= -\overline{v}_0 \left[D \int_0^{\xi^2} f \, d\varsigma^2 \right]_0^{\Xi^2} + \overline{v}_0 \int_0^{\Xi^2} D f \, d\xi^2$$

$$= \frac{-1}{4\pi} \overline{v}_0 \int_0^{\Xi^2} \oint D \frac{\partial}{\partial n} \left(\frac{1}{r} \right) \sqrt{a} \; d\xi^1 \, d\xi^2$$

$$= \overline{v}_0 \iint_\sigma D \frac{\partial}{\partial n} \left(\frac{-1}{4r} \right) d\sigma \qquad (A-33)$$

111

which shows the equivalence of a vortex layer to a doublet layer of intensity D. Note that

$$\frac{\partial D}{\partial \xi^2} = \sqrt{a} \; \gamma^1 \qquad\qquad (A-34)$$

which is the relation necessary to determine the vorticity of the vortex layer from the intensity of the doublet layer.

LIST OF SYMBOLS

$\bar{a}, \bar{b}$ arbitrary vectors

$\bar{a}_1, \bar{a}_2$ base vectors (see Equation (121))

$\bar{a}_\alpha$ base vectors; $\alpha = 1, 3$

$a_{\alpha\beta}$ $= \bar{a}_\alpha \cdot \bar{a}_\beta$; covariant component of the metric tensor

$\bar{a}^\alpha$ adjoint base vectors; $\alpha = 1, 3$

$a^{\beta\gamma}$ contravariant component of the metric tensor where $a_{\alpha\beta}\, a^{\beta\gamma} = \delta_\alpha^\gamma$

A, B arbitrary constants

B_{hn} source coefficient

B_n source integral (see Equation (107))

c blade chord

C, D arbitrary constants

C_D drag coefficient

C_{hn} doublet coefficient

C_L lift coefficient

C_n doublet integral (see Equation (107))

C_p pressure coefficient

C_{ph} pressure coefficient at centroid of hth element

C_T thrust coefficient (see Equation (8))

E_* domain function (see Equation (55))

f, g arbitrary functions

LIST OF SYMBOLS (Continued)

F_{hm}	$= F_m(P_h, t)$; wake coefficient
F_m	wake integral (see Equation (107))
$\bar{g}_\alpha$	adjoint base vectors; $\alpha = 1, 3$
$\bar{g}_\beta$	adjoint base vectors; $\beta = 1, 3$
$g_{\beta\gamma}$	$= \bar{g}_\beta \cdot \bar{g}_\gamma$; covariant component of the metric tensor
$g^{\alpha\beta}$	contravariant component of the metric tensor where $g^{\alpha\beta} g_{\beta\gamma} = \delta^\alpha_\gamma$
i	rotor incidence angle with respect to freestream velocity
$\bar{i}, \bar{j}, \bar{k}$	unit vectors in x, y, z directions, respectively
$\bar{\ell}$	length of isolated vortex element
ℓ	(subscript) denotes lower surface
L_M	vortex line
M	number of elements on the wake
n	direction normal to the surface of the body
$\bar{n}$	normal to surface of the body at point P
N	number of elements on the surface of fuselage and rotor
N_e	number of elements along the circumferential direction of one wake spiral
N_s	number of wake spirals
p	pressure
P_∞	freestream pressure
$\bar{P}_{pp}, \bar{P}_{pm}, \bar{P}_{mp},$ $\bar{P}_{mm}$	location of the corner points of the hyperboloidal element

LIST OF SYMBOLS (Continued)

$\bar{P}_0, \bar{P}_1, \bar{P}_2, \bar{P}_3$ parameters describing the geometry of hyperboloidal elements (see Equation (119))

P point on surface of body

$\bar{P}(t)$ dummy point on surface Σ

P_h centroid of hth elements on surface of fuselage and rotor

$\bar{P}_h(t)$ centroid of element $\Sigma_h(t)$

P'_m centroid of mth elements on the wake

P_m^{TE} corner points along the trailing edge of mth wake element

P_w point on the wake

P_* control point in the flow field

Q_s location of separation line

Q_v location of isolated vortex line that is used to represent the presence of vorticity in the separated wake

r radial distance (see Equation (43))

$\bar{r}$ vector denoting the distance between control point and dummy point

R rotor radius

R_{Σ_2} radius of Σ_2 (see Figure 5)

S_{mn} function that relates the value of φ at the trailing edge with the values of φ at the centroid of the element (see Equation (112))

t time

t_o time when point on the wake is at $\bar{x}_M$

LIST OF SYMBOLS (Continued)

T	thrust
u	(subscript) denotes upper surface
U_W	induce rotor velocity (associated with the convection of the rotor wake)
U_∞	freestream velocity
v	velocity induced by the rotor (see Equation (5))
$\bar{v}$	perturbation velocity
v_x, v_y, v_z	perturbation velocity in x, y, z direction, respectively
v_α	covariant components of vector $\bar{v}$
$\bar{v}_\Gamma$	velocity induced by isolated vortex
V	flight velocity
$\bar{V}$	velocity vector
V'	volume surrounding the surface of the body and wake (see Figure 5)
$\bar{V}'$	resultant flow velocity in the far wake
$\bar{V}_A$	average value of velocity
$\bar{V}_B$	velocity of body
V_x, V_y, V_z	components of velocity in x, y, z directions, respectively
x, y, z	Cartesian coordinates
$\bar{x}_M$	location of a point on the wake
$\bar{X}$	vector describing the vortex lines
y	spanwise coordinate measured from midspan of an elliptical monoplane wing
Y_{co}	blade root cut-out

LIST OF SYMBOLS (Continued)

Γ vortex intensity

Γ_o midspan value of elliptical circulation distribution of a monoplane wing

δ_α^γ Kronecker delta $= \begin{cases} 1 & \alpha = \gamma \\ 0 & \alpha \neq \gamma \end{cases}$

ε radius of surface Σ_1 (see Figure 5)

$\bar{\zeta}$ $= \bar{\nabla} \times \bar{v}$ (see Equation (75))

ζ^α contravarient components of vector $\bar{\zeta}$; $\alpha = 1, 3$

θ rotor angular position

η parameter describing vortex lines

Σ surface which surrounds the volume V'

Σ_B surface of the body

Σ_B' branch surface of isolated vortex line (see Figure 8)

Σ_F surface of the fuselage

Σ_F' surface of the fuselage wake

Σ_h h^{th} element on the surface of the body

Σ_i i^{th} elements on the surface of the fuselage, rotor, and wake

Σ_m' m^{th} elements on the wake

Σ_n n^{th} elements on surface of fuselage and rotor

Σ_R surface of the rotor

Σ_R' surface of the rotor wake

Σ_w surface of the wake

117

LIST OF SYMBOLS (Continued)

Σ'_w — surface surrounding each wake

Σ_0 — surface surrounding the body and wakes (see Figure 5)

Σ_1 — spherical surface of radius ϵ and center P_* (see Figure 5)

Σ_2 — spherical surface of radius R_{Σ_2} and center P_* (see Figure 5)

τ_m — time necessary for material point of wake to move from P_m^{TE} to $\bar{P}'_m$ with velocity $\bar{V}_A$

φ — perturbation potential (see Equation (127))

$\check{\varphi}$ — velocity potential in absence of the isolated vortex (see Equation 62)

φ_h — value of potential at centroid of hth element on the surface of fuselage and rotor

φ_m — value of potential at centroid of mth element on the wake

φ_m^{TE} — value of φ at P_m^{TE}

φ_n — value of potential at centroid of nth elements

$\varphi_{pp}, \varphi_{pm}, \varphi_{mp}, \varphi_{mm}$ — value of the potential at nodal points of the element

$\varphi_0, \varphi_1, \varphi_2, \varphi_3$ — parameter that yields a continuous potential distribution on the element

Φ — velocity potential (see Equation (17))

λ — inflow ratio (see Equation (7))

μ — advance ratio (see Equation (6))

ξ, η — surface coordinate associated with the hyperboloidal element (see Figure 10)

ξ^α — generalized curvilinear coordinates; $\alpha = 1, 2, 3$

118

LIST OF SYMBOLS (Concluded)

ρ   air density

χ   wake deflection angle of the rotor wake geometry with respect to the freestream (see Figure 3)

Ψ   downwash $= \dfrac{\partial \varphi}{\partial n}$

Ψ_n normal wash at centroids of elements Σ_n

Ω   angular velocity of rotor

∇^2 Laplacian operator

$\bar{\nabla}$ gradient operator $= \bar{i}\,\dfrac{\partial}{\partial x} + \bar{j}\,\dfrac{\partial}{\partial y} + \bar{k}\,\dfrac{\partial}{\partial z}$